Chromospheric activity
First results of the observations
with the
Hamburg Robotic Telescope

Dissertation
zur Erlangung des Doktorgrades
des Departments Physik
der Universität Hamburg

vorgelegt von
Marco Mittag

aus Potsdam

Hamburg
2009

Abstract

In this PhD thesis, the fully automatic data reduction pipeline of the Hamburg Robotic Telescope (HRT), first observations and the first analyses of stellar activity are presented. The first part of this thesis deals with the data reduction pipeline. It is based on the IDL reduction package REDUCE, written by Piskunov and Valenti (2002). I adapted REDUCE to take into account the properties of the HRT spectrograph. The data reduction pipeline was designed to automatically perform all standard reduction steps for Échelle spectra including an automatic wavelength calibration. During the observations form Oct. 2008 until Aug. 2009, the pipeline was shown to be working fully automatically and stably. All spectra which are used in this work are extracted with this pipeline. Furthermore, I could show that the wavelength solution depends on air pressure, air temperature and humidity. A correction equation was created to account for these dependencies.

In the second part of this thesis, the results of the first HRT observations are presented. They show the potential and the current state of the telescope. Another important result is the creation of a new photospheric correction. These results were obtained as follows: First, a transformation equation was derived for the HRT S-intex to be the Mount Wilson S-index so that it is possible to compare the activity levels of stars observed at different observatories. Thereafter, new photospheric flux corrections which depend on the colour index $B - V$ for Ca H+K lines were created for main sequence stars, subgiants and giant stars. These flux corrections were obtained using model spectra produced with the multi-purpose stellar atmosphere code PHOENIX. Furthermore, I investigated the relationship between the excess flux in the Ca II H+K lines and the rotation period of the star and created relations to estimate the rotation period of a star. These relations are only valid for main sequence stars. Another method to determine the excess flux in the Ca II H+K lines is to use a template spectrum for comparison. These objects have to show as little activity as possible. I present the first six template candidates and show the spectra of the Ca II H+K lines. These observations are performed to check whether a double peak structure is detected in the line cores. I found two good candidates without a double peak feature. Finally, I present the first five time series of the S-index and two series of radial velocity shifts. The time series of the S-index were investigated in order to check whether it is possible to detect the rotation period of the star. In all time series of the S-index, the significance of the peaks in the periodogram is too small for a clear detection with the highest peak in the periodogram for HD120136 being located at the frequency of the known rotation period. The results of the radial velocity investigations are consistent with the values from literature. However, the significance of the peak in the periodogram for HD120136 is also too small for a detection.

Zusammenfassung

In dieser Arbeit wird die vollautomatische Spektren-Reduktionsprozedur des Hamburger Robotischen Teleskops (HRT), die ersten Beobachtungen und die ersten Ergebnisse von stellaren Aktivitätsuntersuchungen präsentiert.

Der erste Teil der Arbeit beschäftigt sich mit der Spektren- Reduktionsprozedur. Diese basiert auf dem IDL Reduktionspaket REDUCE, geschrieben von Piskunov und Valenti (2002). Dazu wurde REDUCE an die Eigenschaften des HRT Spektrographen angepasst. Die Datenreduktionsprozedur ist so konzipiert, dass alle Standartreduktionsschritte für ein Echelle Spektrum durchgeführt werden können, einschliesslich einer automatischen Wellenlängen kalibration. Während der Beobachtungen von Okt. 2008 bis Aug. 2009 wurde die Datenreduktionsprozedur getestet und es zeigte sich, dass sie vollautomatisch und stabil arbeitet. Alle Spektren, die in dieser Arbeit verwendet werden, wurden mit dieser Prozedur reduziert. Ausserdem konnte ich zeigen, dass die Wellenlängen lösung von Luftdruck, Lufttemperatur und Luftfeuchtigkeit abhänging ist. Um diese Abhängigkeiten zu korrigieren, wurde eine Korrekturgleichung erstellt.

Im zweiten Teil dieser Arbeit werden die Ergebnisse der ersten HRT Beobachtungen vorgestellt. Diese zeigen das Potential und den aktuellen Zustand des Teleskops. Ein weiteres wichtiges Ergebnis ist eine neue Photosphärenkorrektur. Im Folgenden werden diese Ergebnisse aufgeführt:

Als erstes wurde eine Transformationsgleichung bestimmt, um den S-Index vom HRT in den Mount Wilson S-Index umzurechen. Dies ist notwendig um die beobachteten Aktivitätslevel von Sternen mit den Beobachtungen von anderen Observatorien zu vergleichen. Danach wurde eine neue Photosphärenkorrektur der Ca II H+K Linien abhängig vom Farbindex $B - V$ für Hauptreihensterne, Unterriesen und Riesen erstellt. Diese Flusskorrekturen wurden mit Hilfe des vielseitig anwendbaren stellaren Atmosphärencode PHOENIX erstellt. Ausserdem habe ich die Beziehung zwischen dem Flussexcess in den Ca II H+K Linien und der Rotationsperiode des Sterns untersucht und habe eine Gleichung erstellt um die Rotationsperiode zu berechnen. Diese Gleichung ist nur für Hauptreihensterne gültig. Eine weitere Methode um den Flussexcess in den Ca II H+K zu bestimmen besteht darin, einen inaktiven Stern (Template) als Referenz zu benutzen.

Hier stelle ich die Ca II H+K Linien der ersten sechs Template Kandidaten vor, die ich auf die charakteristischen Linienstrukturen eines aktiven Sterns (eine Doppelspitze) untersuche. Zwei dieser Sterne zeigten nicht diese Linienstruktur. Zum Schluss presäntiere ich die ersten fünf Zeitreihen von S-Indizes und zwei Zeitreihen mit Radialgeschwindigkeitsverschiebungen. Die Zeitreihen der S-Indizes untersuchte ich, um die Rotationsperiode des jeweiligen Sterns zu bestimmen. Die Peaks in den Periodogrammen der Zeitreihen sind nicht stark genug für einen eindeutigen Nachweis. Nur für HD120136 ist die Frequenz des stärksten Peaks mit dem bekannten Literaturwert vergleichbar. Auch die Ergebnisse der Radialgeschwindigkeitsuntersuchung sind konsistent mit den Literaturwerten. Für HD120136 ist der Peak im Periodogramm wieder zu klein für einen eindeutigen Nachweis.

Contents

Chapter 1

Introduction and motivation

The systematic search for magnetic activity cycles of stars was started in 1966 with the Mount Wilson project by O. C. Wilson. The results of this project have shown that a lot of stars had periodic activity cycles like the Sun. Furthermore, short time variations in active stars were observed. Those variations are caused by the rotation of the star, hence, its rotational period can be measured directly: active regions migrate apparently across the surface of the star and this causes a variation in the flux intensity. The active regions, however, move very slowly compared to the rotation velocity of the star. Therefore, the variation in the flux intensity is caused by the rotation of the star. If the rotational period of the star is measured in consecutive years, one is able to determine whether this period is changing. One explanation for this change is the differential rotation and spot migration as observed for the Sun in form of the butterfly diagrams. In order to measure a rotation period or an activity cycle, it is necessary to monitor a star about a long time. The Hamburg Robotic Telescope (HRT) was designed for this kind of observations. The observations will be performed automatically. This is economic and the observations can be performed optimally, e. g., in the object selection, exposure time. The HRT is a spectroscopic telescope with an Échelle spectrograph.

My motivation was to provide some basics like a data reduction pipeline, a transformation equation from the S-index of the HRT to the Mount Wilson S-index, redetermination of the so-called Ca II H+K excess flux and to conduct test observations.

In Oct. 2008, the scientific observations were started with the blue spectral channel of the spectrograph. The creation of a standard data reduction pipeline for the HRT was an important part of this work. It is working fully automatically and starts after the observation night. Thus, the astronomer has available the fully reduced spectra few hours later.

Another important part of this work were the observations with the HRT. Here is shown the potential and performance of the HRT. First, the observed objects were used to create a transformation equation from the S-index of the HRT to the Mount Wilson S-index. This transformation is necessary to compare the results for the measurements of the activity levels of stars with results of other observatories and projects.

Furthermore, several stars were observed to check whether they are usable as template stars. These stars can be use to determine the excess flux in the Ca II H+K lines, which is a result of activity. Another applied method to determine an excess flux in the Ca II H+K lines, is to use of a photosphere correction. In order to create a photosphere correction for main sequence, subgiant and giant stars in dependence on the colour index $B - V$, the

multi-purpose stellar atmosphere code PHOENIX was used.

Finally, the results of the first object monitoring are presented. Here, the focus lies on the variations in the S-index and in the radial velocities. The measurement of the S-index is one of the primary tasks of the HRT because one can measure the activity level of a star with the S-index. With the variations in the S-index, it is possible to measure the rotation period. The radial velocity shift measurements are used, e. g., to find planets. In order to achieve this, the wavelength calibration has to be very precise.

Chapter 2

Activity

In this chapter, I want to give a short historical overview over the discovery of activity signs on the Sun. Then, I show images with the different signs of the magnetic activity in the photosphere, chromosphere and in the corona of the Sun. After this, I will give a short overview over the activity tracers on stars. Finally, I describe briefly the $\alpha\Omega$ dynamo theory. This theory describes how the magnetic field is created in solar like stars. At first, I give a definition what is meant with the term activity.

2.1 A definition of the term activity

The term activity is not clearly defined. A definition for the term activity or nonradiative activity provided by Linsky (1985) is the following: "phenomena and physical properties that occur when the energy balance in a stellar atmosphere departs greatly from pure radiative equilibrium". In this definition, the phenomena and physical properties are included, which are caused by the magnetic field of the star, thus it is often denoted as magnetic activity.

2.2 A historical overview

The historical facts and the individual personal data were taken from the "Encyclopedia of ASTRONOMY and ASTROPHYSICS" (Murdin 2001) and "The Sun from Space" (Lang 2008). This historical overview presents only an overview over some important events in activity research.
In 1611 J. Fabricuis[1], C. Scheiner[2], G. Galilei[3] and J. Kepler[4] rediscovered independently the sunspots and in this year, the modern history about the activity investigation began. Galilei interpreted the motion of the sunspots over the solar disk as evidence of the Sun's rotation. From his observations, he derived a period of about 27 days. Thereafter, the records of the sunspots were started. In Fig. 2.1, the yearly averaged relative sunspot number R vs. time is shown since 1610. The relative sunspots number R is defined as:

$$R \quad = \quad K(10g + f), \tag{2.1}$$

---

[1] Johannes Fabricuis, German Lutheran pastor and astronomer 1587-1616
[2] Christoph Scheiner, German Jesuit and astronomer 1575-1650
[3] Galileo Galilei, Italian astronomer and physicist 1564-1642
[4] Johannes Kepler, German astronomer 1571-1630
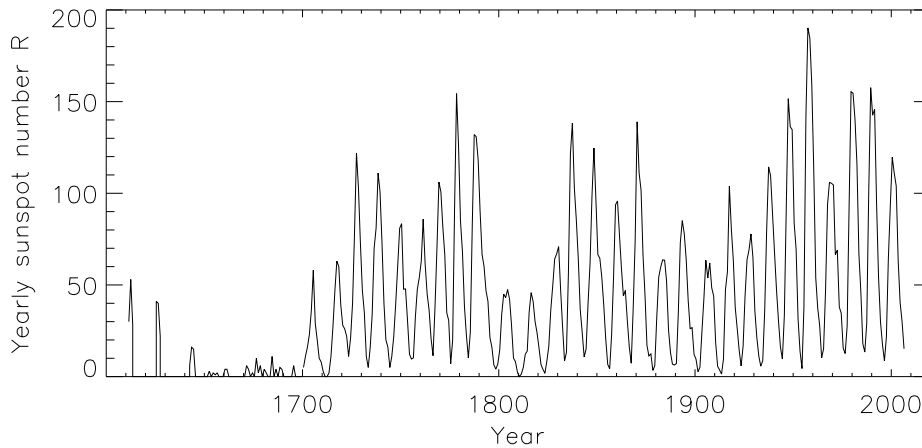
Figure 2.1: The yearly averaged relative sunspots number R since 1610, 1610-1700 (http://www.ngdc.noaa.gov/stp/SOLAR/ftpsunspotnumber.html#ancient) and 1700- (http://sidc.oma.be/sunspot-data/)

where g is the number of spot groups, f the total number of individual spots and K a scaling factor dependent on the instrument and observation conditions (Zirin 1988). The relative sunspot number R was introduced by J. R. Wolf[5] in 1848. In the time between 1645 and 1715, the number of sunspots was very low. This period of very low activity is called Maunder[6] Minimum. The term Maunder minimum was introduced by Eddy (1976). In 1802 W. H. Wollaston[7] discovered dark lines (absorption lines) in the solar spectrum. Frauenhofer[8] found and catalogued 1814 574 lines in the solar spectrum. The strongest lines in the solar spectrum were labelled with the letters A to Z from the red part of the spectrum to the blue part. These lines are called Frauenhofer lines. In 1843 S. H. Schwabe[9] announced after an observation range of 17 years that the sunspots have a period of about 11 years. This result was confirmed by R. C. Carrington[10]. He also noted that the first sunspots turn up at the latitudes around $\pm 30°$ and with the time, the latitudes where the sunspots turn up migrated in the direction of the Sun's equator. Before the spots contacted the equator the sunspot minimum approached. The new sunspot cycle starts when the new spots turn up in higher latitudes. Carrington found that the rotation velocity of the Sun is not uniform. The velocity of the spots was larger near the equator. With the discovery of the absorption lines in the solar spectrum and the recognition by G. Kirchhoff[11] that these absorption lines show the composition of the solar atmosphere, the spectroscopic investigation of the Sun started. The investigation of the corona began

---

[5]Johann Rudolf Wolf, Swiss astronomer 1816-1893

[6]E. W. Maunder, English solar astronomer 1851-1928

[7]William H. Wollaston, Chemist and physicist 1766-1828

[8]Joseph von Frauenhofer, German instrument-maker 1787-1826

[9]Samuel Heinrich Schwabe, German astronomer 1789-1875

[10]Richard Carrington, English amateur astronomer 1826-1875

[11]Gustav Robert Kirchhoff German physicist 1824-1887

with a photographic observation during the eclipses in 1860 by A. Secchi[12] and W. de la Rue[13]. The spectroscopic observations of the corona started with the eclipses in 1868. G. E. Hale[14] developed the spectroheliograph and found the chromospheric network (Sect. 2.3.2) in 1892. With this instrument, it is possible to take images of the Sun in single spectral lines. In 1901 J. Evershed[15] published a spectrum of the solar chromosphere and compared this with a spectrum of the solar photosphere. He found that the strongest lines in the chromosphere are the Frauenhofer lines. Hale measured in 1908 the magnetic field in sunspots in doing so he used the Zeeman effect, the splitting of a spectral line in a magnetic field.

In 1930 B. F. Lyot[16] invented the coronagraph. This instrument is a telescope where a disk is mounted in front. The disk covers the solar disk so that one can see the coronal light. The invention of the coronagraph allowed to investigate the corona without an eclipse. With the end of the second world war and the invention of the rocket, the investigation of the Sun extended to wavelengths which are not observable from the ground, e. g., in X-rays and UV (ultraviolet). The first extreme-ultraviolet (EUV) spectrum of the Sun was taken in 1946. The first soft X-rays of the Sun were detected in 1948. These observations were performed by V-2 rocket experiments. In the today's time, it is possible to observe the Sun continuously with satellites, e. g. Soho satellite. The Sun is monitored since then with imaging telescopes and spectrometers in different wavelength ranges.

Observations of the Sun are very important because one can observe directly the structure of the surface. Such observations are not possible for other stars. Therefore, the Sun is important for activity research. However, one can observe periodic variations in the spectral line of other stars e. g., in the emission cores of the Ca II H+K and H α lines which are caused by activity.

2.3 Signs of activity on the Sun

The activity of the Sun is observed continuously in different wavelength ranges so that one can observe the different atmospheric layers. In this section, I show images of the Sun in an inactive and active phase. Therefore, I use images for the photosphere, chromosphere and corona. In Fig. 2.2-2.7, the images in the different layers of the Sun and activity phases are seen. The images for the active and inactive phase were taken on Oct. 29 2003 and Sep. 20 2009, respectively. On these days, the relative sunspot number was $R = 167$ and $R = 0$, respectively (http://sidc.oma.be/sunspot-data/dailyssn.php). In the following, the activity phenomena in the different layers are described briefly.

2.3.1 Photosphere

The photoshere is the atmospheric layer of the Sun which is visible with the eye. The surface of the Sun is defined at the optical depth of $\tau = 1$. The photosphere is located above the convective zone of the Sun and shows a web-like pattern. This pattern is called the photospheric network. The network shows cellular features which are called Granules

---

[12]Angelo Secchi, Italian Jesuit and astronomer 1818-1878
[13]Warren de la Rue, English astronomer 1815-1889
[14]George Ellery Hale, American astrophysicist 1868-1938
[15]John Evershed, English astronomer 1864-1956
[16]Bernard Ferdinand Lyot, French astronomer 1897-1952
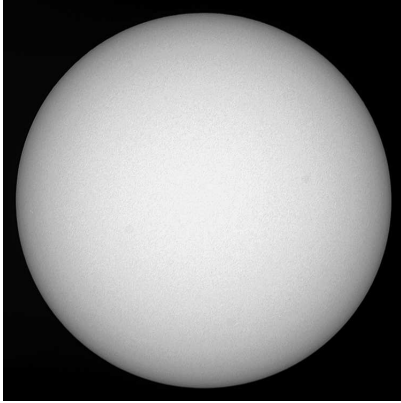
Figure 2.2: Photosphere in the inactive phase
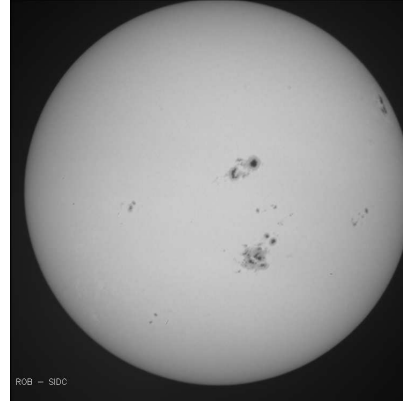
Figure 2.3: Photosphere in the active phase
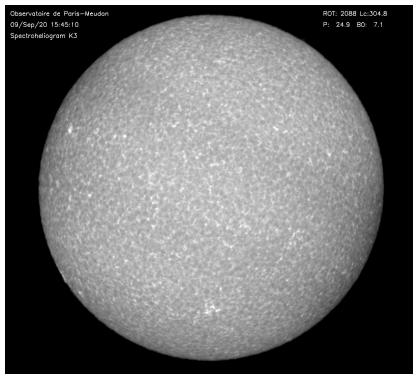
Figure 2.4: Chromosphere in the inactive phase
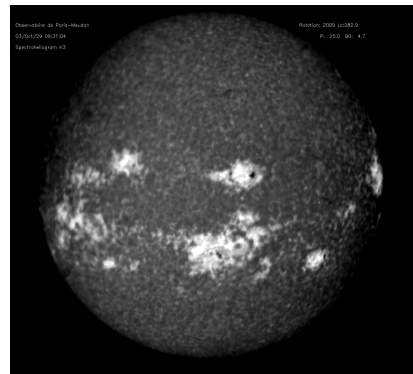
Figure 2.5: Chromosphere in the active phase
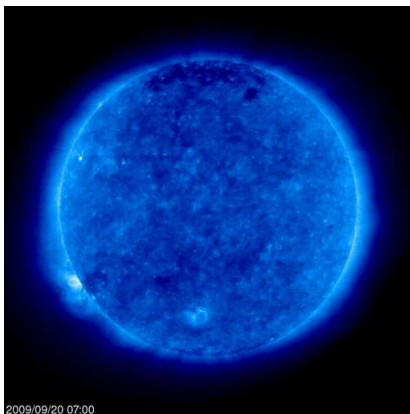
Figure 2.6: Corona in the inactive phase
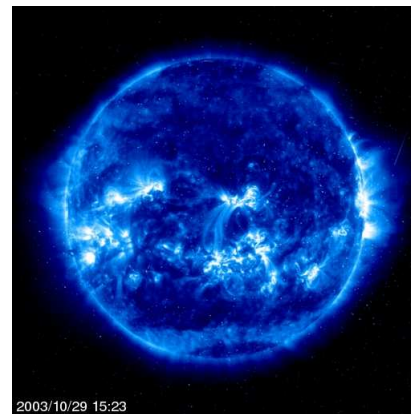
Figure 2.7: Corona in the active phase
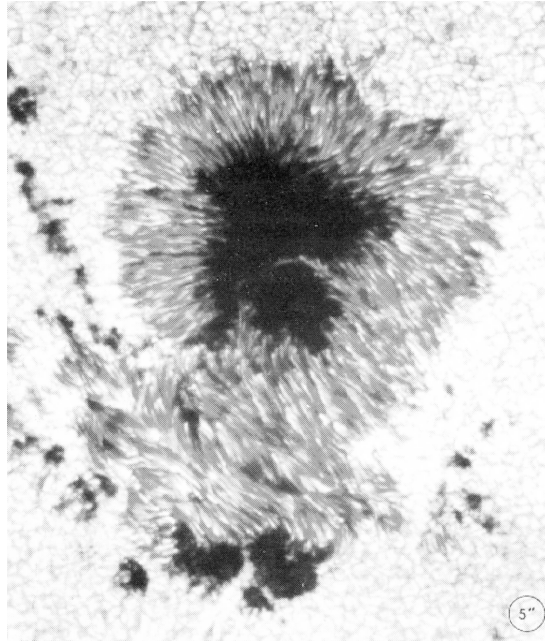
Figure 2.8: Example for a sunspot (Schrijver and Zwaan 2000)

and are the tops of convection cells. The bright areas in the Granules are produced by uprising hot plasma. This plasma cools down and sinks into the areas which are seen as dark edges (Stix 2004). The Granules have a size of 600-1300 km (Schrijver and Zwaan 2000).

The temperature in the photosphere of the Sun decreases outwards from roughly 6500 K to roughly 4000 K, see Fig. 6.4. Nevertheless, one can define a temperature of the photosphere because the photosphere is in radiation equilibrium. This temperature is called effective temperature. The effective temperature of the Sun is $T_{eff} = 5777$ K (Cox 2000). The photosphere of the Sun is about 500 km thick (Strassmeier 1997) .

In Fig. 2.2 and 2.3 (http://sidc.oma.be/uset/searchuset.php), the photosphere is shown in the inactive and active state. The sign of activity of the photosphere are the sunspots. The number of sunspots is a tracer of the activity level of the Sun. In the inactive phase, see Fig. 2.2, no sunspots are seen. On the other hand in the active phase, sunspots are seen in northern or southern hemisphere or in both hemispheres like this example. The sunspot numbers for the northern and southern hemisphere for the Oct. 29 2003 were $R = 66$ and $R = 101$ (http://sidc.oma.be/sunspot-data/dailyssn.php), respectively. In the following, I will give some observable characteristics about sunspots.

Sunspots

In Fig. 2.8, an example of a sunspot is shown. The sunspot consists of two areas. The dark centre is called umbra and the bright belt at the umbra is called penumbra. The reason for the darkness of the umbra and penumbra is the temperature difference between the region of the sunspot and the rest of the surface. The temperature of the umbra and penumbra are 1000 to 1900 K and 250 to 400 K (Thomas and Weiss 2008), respectively, cooler than the effective temperature of the quiet Sun. The magnetic field strength of the

umbra varies from (2400 ± 200) G for small sunspots to (2900 ± 400) G for large sunspots. The integrated radiation in the umbra and penumbra is only 20 to 30% and 75 to 85%, respectively, of the flux of the quiet Sun (Thomas and Weiss 2008).

2.3.2   Chromosphere

The chromosphere is the atmospheric layer which is located above the photosphere. This atmospheric layer is about 2000 km thick. The temperature of the chromosphere increases from the minimum of the atmospheric temperature of roughly 4000 K to circa 25000 K. At above 2000 km height of the atmosphere, the temperature of the chromosphere increases within 100 km from 7000 K to circa 25000 K (Stix 2004).

The spectrum of the chromosphere comprises emission lines with very little continuum (Strassmeier 1997). With the spectroheliograph, it is possible to observe the emission of individual spectral lines, e. g. , Ca II K, H α, and one can resolve the active chromospheric regions of the Sun. The excess flux of these lines is a good tracer of the activity state because the intensity of the emission in these lines is dependent on the activity level.

The chromosphere of the Sun in the inactive and active state is shown in Fig. 2.4 and Fig. 2.5 (http://bass2000.obspm.fr/home.php). To compare the chromosphere of the inactive and active phase of the Sun, images of the Sun are used which were taken in a Ca II wavelength filter at 3933.66 Å. In the active phase, the Sun shows bright emission areas (plage) in contrast to the Sun in the inactive phase. In the inactive phase, only the chromospheric emission network is seen. The chromospheric network shows the edges of the Supergranules where a emission flux, e. g. Ca II K, is produced. The Supergranules are a combination of individual Granules (Sect. 2.3.1) with a size of 15000-30000 km (Strassmeier 1997; Schrijver and Zwaan 2000).

If one compares the chromosphere and photosphere, Fig. 2.5 and Fig. 2.3, the chromosphere shows more and larger active regions at the Sun as in the photosphere.

2.3.3   Corona

The last atmospheric layer is the corona. Below the corona, the transition region is located. This layer is very thin and is located between the chromosphere and corona. In the transition region, the temperature increases from roughly 25000 K to the temperature of the corona of circa 10^6 K (Stix 2004). The corona is observed in X-rays and in EUV (Extreme ultraviolet wavelength). This monitoring is performed currently with, e. g., the SOHO satellite. This satellite observes the Sun in different wavelength bands.

In Fig. 2.6 and 2.7 (http://sohodata.nascom.nasa.gov/cgi-bin/data_query), the corona of Sun in the inactive and active state are shown. The images were taken with the wavelength filter 171 Å (Fe IX). The emission level of this line is a tracer of the activity state. In the image which was taken in the inactive state (Fig. 2.6), no active regions are seen. In Fig. 2.7, the Sun is seen in an active state. One can see the bright activity areas. The location of these areas are often the same as the active areas in the chromosphere, see Fig. 2.5. Furthermore, one can see in Fig. 2.7 the coronal loops. A good visible example of a loop in Fig. 2.7 is the loop, which connects an active region in the northern hemisphere with an active region in the southern hemisphere. These regions are located at the positions of the great sunspots in the northern and southern hemisphere, see Fig. 2.3. Finally, the corona in Soft X-rays is shown in Fig. 2.9. This image was taken with the Soft X-Ray Telescope
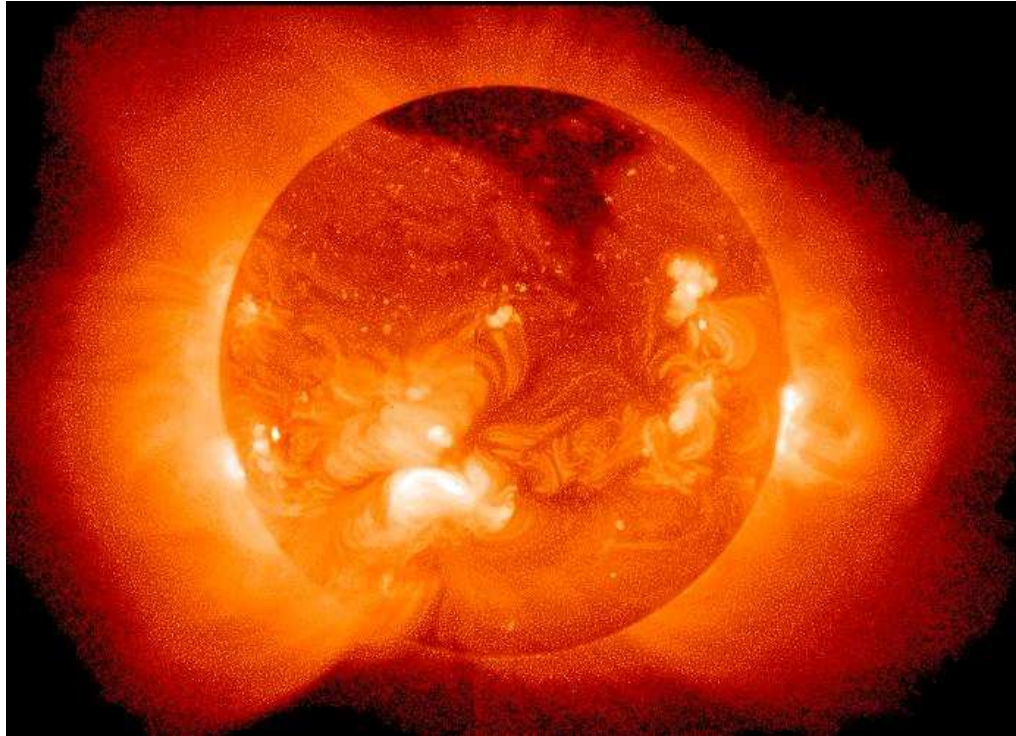
Figure 2.9: Sun in X-rays observed with the Soft X-Ray Telescope onboard of Yohkoh satellite (http://rsd.gsfc.nasa.gov/rsd/images/yohkoh_l.jpg)

onboard of the Yohkoh satellite. The date of this image is unknown to me. Nevertheless, the Sun was in an active phase because one can seen coronal loops in the image.

2.4 Activity in stars

The activity of a star can only be observed with photometric or spectroscopic methods in different wavelength ranges. In the optical, the Ca II H+K lines are very important for stars of the spectral types F, G and K. The H α line is used as activity tracer for late K and M stars where the Ca II H+K region in the spectrum is hard to observed and also for T-Tauri stars. In this thesis, Ca II H+K lines are used as activity tracer. Therefore, I will give a short overview about activity research with the Ca II H+K lines from the discovery until the current research.

The Ca II H+K lines are Frauenhofer lines and the most prominent lines in the blue wavelength range. In 1901 J. Evershed took solar spectra of the photosphere and chromosphere. The Ca II H+K lines were also very prominent in the spectrum of the chromosphere. The variability of the Ca II H+K lines was discovered by G. Eberhard[17] and K. Schwarzschild[18] (1913) in the spectra of Arcturus, Aldebaran and σ Geminorum. In 1957 O. C. Wilson[19]

---

[17]Gustav Eberhard, German astronomer 1867-1940 (http://kuffner-sternwarte.at/sternwarte/vks_ksw_astronomen.html)

[18]Karl Schwarzschild, German mathematical physicist 1873-1916

[19]Olin Chaddock Wilson, American astronomer 1909-1994

and M. K. Vainu Bappu[20] found a dependence of the width of the Ca II H+K lines and the absolute magnitude (Wilson and Vainu Bappu 1957). This is called the Wilson-Bappu effect.

In 1966 O.C. Wilson started a systematic long-term monitoring of solar-like stars. To measure the variability, the Ca II H+K lines were used. This project is known as Mount Wilson Project and was performed for about 30 years. The Mount Wilson Project was the most important project because of the long runtime. Therefore, the Ca II H+K lines had developed to the most important spectral lines of the activity research in the optical for later F to K stars. With the Mount Wilson project, the systematic search of activity cycles of other stars was started. Based on the measurements of the Mount Wilson project, short- and long-term variations were found in the Ca II H+K lines of other stars. Here are noted some important papers with the results of this project, e. g., Wilson (1978), Vaughan et al. (1981), Noyes et al. (1984) and Baliunas et al. (1995). It was found that other spectral lines also show variability. This variability is correlated with the variation in the Ca II H+K lines. Here, as example the H α and Mg II H+K spectral lines are noted. The Mg II H+K lines are observed with the IUE satellite (International Ultraviolet Explorer). This satellite was operated from 1978 until 1996. The search of short- and long-term variations of stars are performed up to date. The successor of the Mount Wilson project is the long-term monitoring program at the Lowell Observatory, which was started in 1994. With the use of satellites, a correlation between the variations in the Ca II H+K flux and the X-ray radiations of the stars (observed with the Einstein satellite) was found at the beginning of the 80th of the 20th century (Mewe and Zwaan 1980; Mewe et al. 1981). With the modern X-ray satellites (XMM-Newton and Chandra), active stars are observed and high resolution grating X-ray spectra are taken. With these observations, the coronal structures are investigated, e. g., the abundances, temperature and L_X/L_{bol} (Güdel and Nazé 2009).

2.5 $\alpha\Omega$ Dynamo

The phenomena of activity are created by the magnetic field of the star. With the observation of the Sun, it is possible to observe these phenomena in detail. The question is, how the magnetic field of the Sun is created.

The natural lifetime of the magnetic field in the convective zone is much shorter than the lifetime of solar-like stars (Wolter 2004). Hence, a mechanism is necessary to regenerate the magnetic field of these stars. This mechanism is called dynamo. The dynamo theory is a part of the magnetohydrodynamics (MHD). The MHD is concerned with the magnetic field in a plasma and one assumes the plasma as a continuous fluid in motion (Murdin 2001; Foukal 2004).

A dynamo theory that describes the magnetic field generation of the Sun is delivered by the $\alpha\Omega$ Dynamo theory described by Parker (1955). The $\alpha\Omega$ dynamo is composed of two effects, the α effect and the Ω effect. In the following, I briefly describe the α and Ω effect.

---

[20]Manali Kallat Vainu Bappu, India astronomer 1927-1982
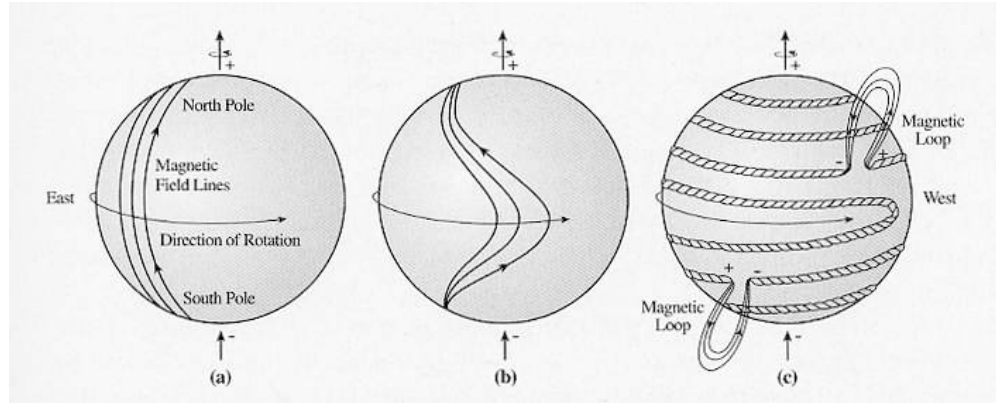
Figure 2.10: The omega effect (Lang 2008)

2.5.1 Ω Effect

The formation of the Ω effect is illustrated in Fig. 2.10. This is based on the model by Babcock (1961). One assumes that the inital magnetic field of the star is a dipolar field (also called poloidal field) like that of a bar magnet (Fig. 2.10a). The magnetic field lines run also inside the star. If the star rotates, the rotation velocity at the equator is larger than at the polar region (differential rotation). Through the differential rotation, the internal magnetic field lines becomes stretched out and wrapped. Furthermore, the magnetic field lines are coalescent to magnetic flux tubes, which are located in the overshoot region (region at the base of the convective zone) (Fig. 2.10b and 2.10c) (Babcock 1961; Lang 2008). Through the formation of the magnetic flux tubes, the poloidal magnetic field is changed into a toroidal magnetic field.
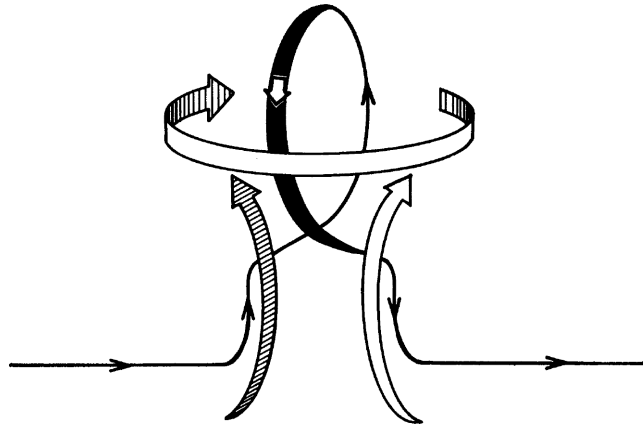
Figure 2.11: The alpha effect the solid line ilustrad the magnetic flux tube and the arrows the plasma motion (Parker 1970)

2.5.2 α Effect

In the convective zone, blobs of plasma can rise and through the Coriolis force, these blobs rotate (northern hemisphere of the Sun clockwise, southern hemisphere of the Sun counterclockwise). If magnetic flux tubes are enclosed into these rising blobs of plasma, the magnetic flux tubes rise also with upward and eventually penetrate the photosphere, see Fig. 2.10c and creates a bipolar region. The points where the magnetic flux tube penetrates the photosphere are visible as dark spots, the so called sunspots. The rising magnetic flux tubes are twisted by the Coriolis force, see Fig. 2.11, and the toroidal magnetic field is changed into a poloidal magnetic field, and vice versa (Schrijver and Zwaan 2000; Thomas and Weiss 2008).

Chapter 3

Hamburg Robotic Telescope

With the Hamburg Robotic Telescope (HRT), long-term monitoring of active stars will be performed. Therefore, the HRT is designed for fully automatically observations. This is the optimal solution to perform a long-term monitoring, because the observation time is used efficiently. Furthermore, the automatically observation is more economic as the manual observation. The final location of the HRT will be Guanajuato in Mexico. In Fig. (3.1), the diagram of the HRT software system is shown. In this chapter, the HRT system is described briefly and for more details see González-Pérez et al. (2008).

3.1   Central Control System

The Central Control System (CCS) is the core of the HRT software system. It controls the whole system and checks its status during the observations. The CCS has two modes of operation. In the interactive mode, the astronomer has full control of the system and can accomplish each of the observation steps by hand. In the robotic mode, the CCS decides which steps of the observation will be performed next. Furthermore in the robotic mode, the CCS reacts to each possible error during the observations by performing the necessary actions to handle this error. In the following, the robotic course of the observation night is described briefly.

The first steps of an observation i. e., the initialisation of the subsystems, opening the roof, the start of night calibration (e.g. focusing) and start time of the observation, are dependent on the elevation of the Sun. Furthermore, the end of the observations depends also on the elevation of the Sun. First, the CCS initialises the individual subsystem (Sect. 3.2). Then, the calibration images, bias, dark and flat field are taken. Next, the weather conditions are checked, if the weather conditions allow the observation, then the roof is opened and the telescope is initialised. Thereafter, some calibrations are performed: First, the telescope is focused by searching the minimal FWHM of the disc of a star on the guiding camera. Then, it is searched the fibre entrance position as viewed from the guiding camera and finally, the focus is determined for the optimal spectrograph output. Thereafter, the scientific observation is started. In the morning, the observation is stopped and the telescope and the roof are closed. Following, the calibration images, bias, dark and flat field are taken. Finally, the system is shutdown and thereafter, the scientific spectra are reduced with the HEROS data reduction pipeline (Ch. 4). The results are saved in the HRT archive.
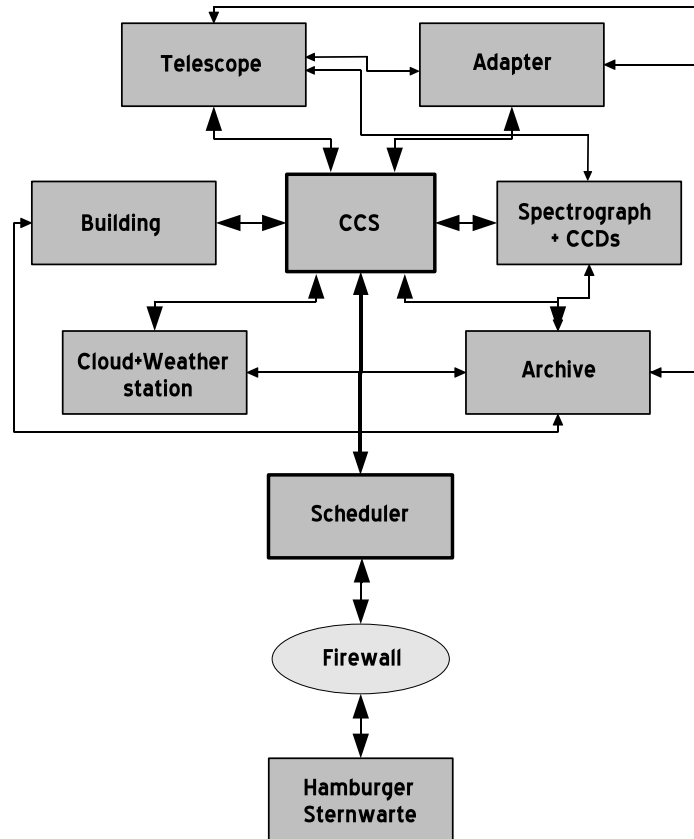
Figure 3.1: Diagram of the HRT software system, by J.N. González-Pérez

3.2   Subsystems

3.2.1   Telescope

The telescope Fig. 3.2 is controlled by the control software PILAR, developed by 4PI Systeme GmbH.

It was built by Halfmann Teleskoptechnik GmbH and installed at Hamburg Observatory in 2005. This Cassegrain-Nasmyth F/8 type telescope has a 1.2 m aperture, an ALT/Az mounting and final direct drives with high-precision absolute encoders. The telescope has two different types of bearing. The azimuth bearing is hydraulic and the elevation bearing is a precision diagonal roller.

The optics of the telescope was built by Carl Zeiss Jena GmbH and consists of two parabolice mirrors, the primary M1 and the secondary M2, and a tilted flat mirror M3.

An instument platform is located at the Nasmyth focus and it is attached an adapter (Sect. 3.2.2).

The telescope has a very good technical performance. The average tracking lost rate is 0.033 and 0.040 [arcsec/min] in the elevation and azimuth, respectively (Mittag 2006). For

Figure 3.2: The Hamburg Robotic Telescope

the pointing, the HRT uses a temperature dependent pointing model, this increases the pointing and tracking accuracy.

3.2.2 Adapter

This unit and its control software are responsible for the acquisition of the object. Also this subsystem controlls the focussing and guiding. The adapter contains the flat field and the ThAr lamp for the calibration images. A fibre holder and two SBIG ST7 CCD cameras are attached on the adapter.
The CCD 1 looks on the fibre entrance and with the CCD 2, the acquisition of the objects, the focussing and guiding are performed. The fibre holder holds the fibre entrance on the adapter and in the telescop beam. This fibre is a polymicro FVP $50/70\mu$ fused silica fibre and is the connection between the telescope and spectrograph.

3.2.3 Spectrograph

The spectrograph of the HRT is the Heidelberg Extended Range Optical Spectrograph (HEROS). The HEROS is a permanent loan from the Landessternwarte Heidelberg on the Hamburg Observatory. The Fig. 3.3 shows the scheme of this spectrograph.
The HEROS spectrograph is a fibre fed Échelle spectrograph. It has a blue and red spectral channel. The wavelength range is 380 to 570 nm and the spectral resolution is R≈20.000 for the blue channel. The CCD camera has a E2V 2Kx2K chip and was built by OES GmbH. At present, the red channel is not in operation. In summer 2009, two new CCD cameras are delivered for the red and blue channels and the spectrograph will be upgraded. These CCD cameras are built by Andor and have also E2V 2Kx2K chips.

3.2.4 Archive

In the archive, the scientific images and the extracted spectra are stored. Also, log files about system status of the subsystems during the observation are saved. At present, this

FLASH components ——
FLASH housing - - - -
HEROS components - - - -
HEROS housing - - - -
common light path - - - -
blue channel light path - - - -
red channel light path - - - -

Blue CCD   Shutter   UV Camera   Blue Crossdisperser

Red Crossdisperser

Collimator   Dichroic Filter   Echelle

Red Camera

Fiber

Shutter

Red CCD
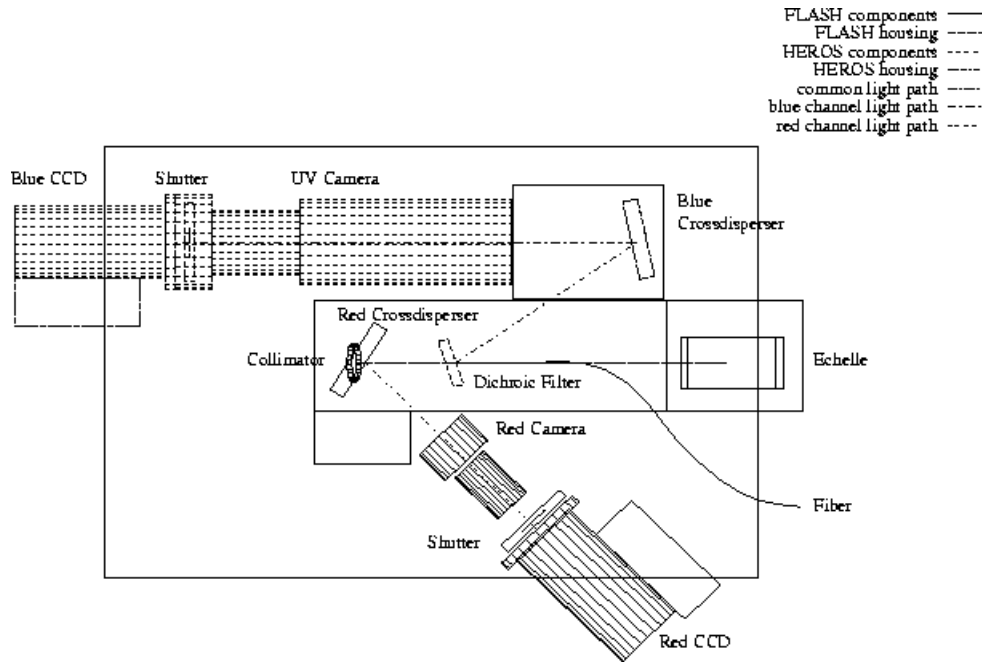
Figure 3.3: The scheme of the HEROS spectrograph (http://www.hs.uni-hamburg.de/DE/Ins/Per/Hempelmann/HRT/index.html)

subsystem is in a preliminary status.

3.2.5 Scheduler

The scheduler has the function to decide which star will be observed next. It requests all relevant information for the observation, the object coordinate, the scientific priority and the exposure time to optimize the available observation time. The scheduler contains also a simpler scheduler, the engineering scheduler, which is used for engineering measurements and targets of opportunities.

3.2.6 Building

This subsystem control the open and close process of the telescope building. At present, the building is located at the Hamburg observatory and has a simple motor-drive-roll-off roof.

3.2.7 Weather station and cloud monitor

The weather station monitor the current weather conditions, temperature, air perssure, humidity, wind and the precipitation. Furthermore, a cloud monitor is available to observe the cloud coverage in the night. The cloud monitor checks the sky cover, if the sun below 12°. The cloud coverage is estimated by taking image of the night sky and counting the number of visible stars.

Chapter 4

Data reduction pipeline

In this chapter, I present the fully automatic data reduction pipeline of the HRT for the blue spectral channel of the HEROS spectrograph.

The spectra, which were taken with the CCD camera of spectrograph, are two-dimensional. These two-dimensional spectra are reduced to one-dimensional spectra. This reduction is performed with a data reduction pipeline. It is possible to automatise the data reduction process so that the astronomer can concentrate on the analysis of the scientific data instead of the data extraction. Therefore, the HRT/HEROS reduction pipeline is provided as fully automatic reduction pipeline including an automated wavelength calibration. It is started by the CCS (Sect. 3.1) of the HRT system after observations and calibrations. The reduced data are stored in an archive.

This pipeline is implemented in IDL (Interactive Data Language) and uses the reduction package REDUCE, by Piskunov and Valenti (2002). REDUCE is a powerful package providing the required functionality for the HEROS pipeline. In Fig. 4.1, an example of the spectrum extracted with the HRT/HEROS reduction pipeline is shown.
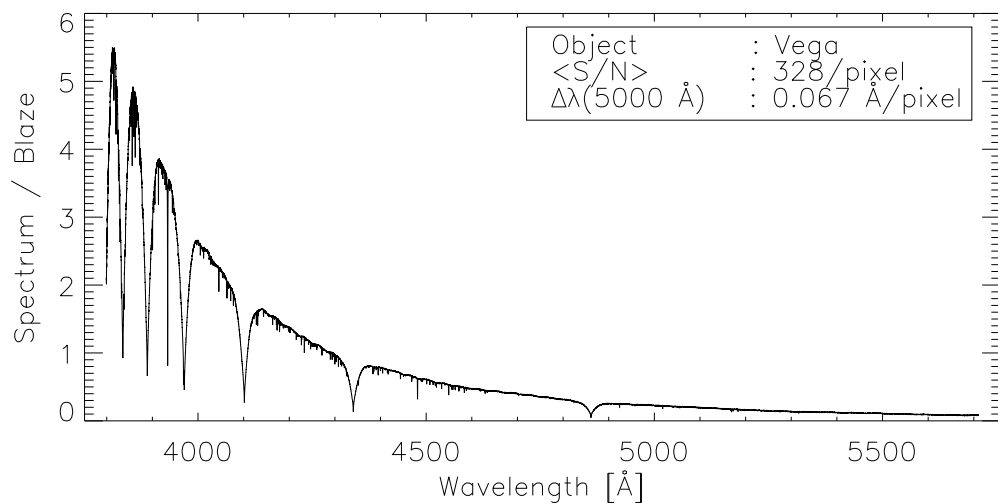
Figure 4.1: An example result: Vega spectrum relative to the flat field spectrum
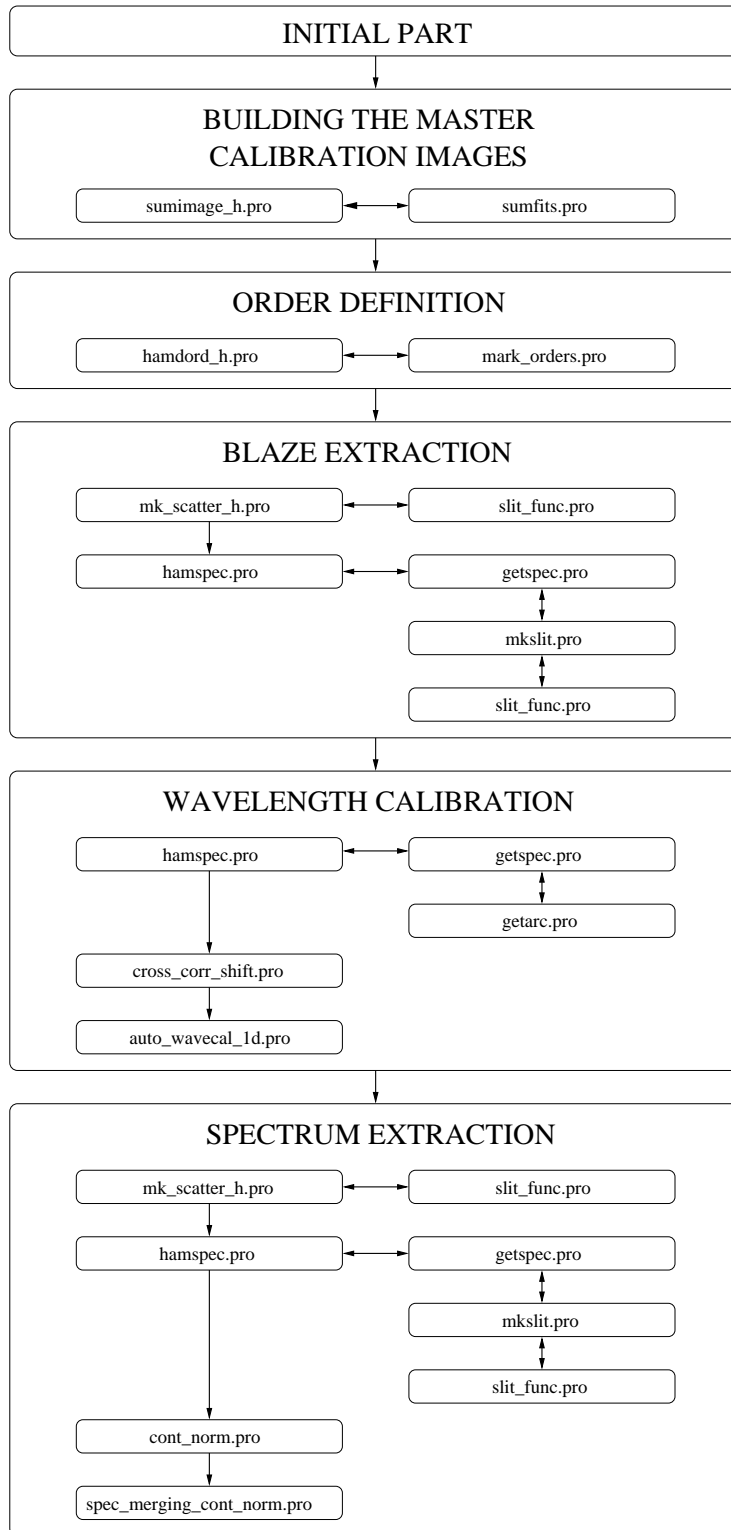
Figure 4.2: Flow chart of the reduction pipeline with the important procedure

This chapter provides a general description of the HEROS pipeline and introduces briefly the important procedures and functions. In Fig. 4.2, a flow chart of the data reduction pipeline of the HEROS with the important procedures is shown. Furthermore, a manual wavelength calibration with the REDUCE procedure *wavecal.pro* is described.

4.1 First steps to use the REDUCE package

In order to use the REDUCE package, one has to modify the function *modeinfo.pro* (Sect. 4.4.3). This modification is necessary because the function modeinfo.pro checks whether the spectrograph mode is valid.

The REDUCE package uses a mask file to identify bad CCD pixels. The mask file is an image with pixel values 0 or 1. To build the mask file, the image is checked for defects; good pixels are assigned the value 1 while damaged ones are set to 0.

4.2 Reduction pipeline

The syntax for a call of the pipeline in IDL is:

```
heros_pipeline_v1, date [, DAY=day, [NONAUTOCAL=nonautocal, PLOT=iplot,
                   MANUAL=manual, NO_CORR_IM=no_corr_im,
                   NO_USE_SKY_IMAGE=no_use_sky_image,
                   NO_ADD_SCI_IMAGE=no_add_sci_image]]
```

The *v1* indicates the version of the pipeline. The parameter ''DATE'' is the starting date of the observation night and the syntax is 'yyyy_mm_dd' e. g. '2007_12_15'; this parameter is required. It defines the sub-directory for raw data and the sub-directory where the results are saved. The keyword ''DAY'' is used for the reduction of solar spectra taken during day-time. The corresponding images are saved in another sub-directory. This keyword is non-optional for the reduction of the solar spectra. The options in the second brackets are optional.

They allow a flexible use of the pipeline. The keyword ''NONAUTOCAL'' is set to switch off the automatic wavelength calibration. With the keyword ''PLOT'', one receives informational plots. If the keyword ''MANUAL'' is set, then the pipeline stops after each reduction part e.g. after building and saving the master bias. The keyword ''NO_CORR_IM'' switches off the cutoff of the last row and saves it in a temporary directory (Sect. 4.2.1), because the modified images are already stored in the temporary directory. If it is not necessary to use the sky images, then one sets the keyword ''NO_USE_SKY_IMAGE''. The keyword ''NO_ADD_SCI_IMAGE'' is used if one does not require a spectrum from the summed object images.

4.2.1 Preparation of the reduction

Before the main reduction starts, it is necessary to prepare this reduction. The flow chart Fig. 4.3 shows the main steps of this part.

The first step of the preparation is the definition of the directory holding the raw data.
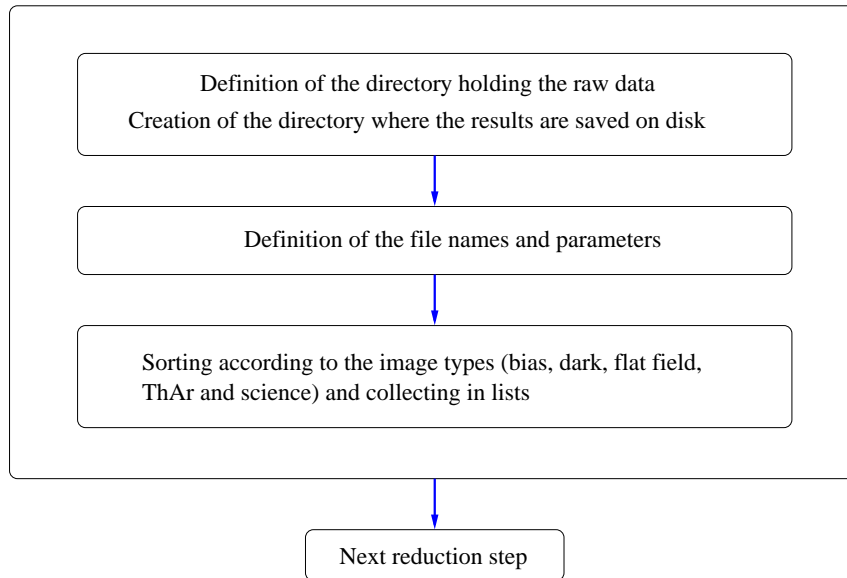
Figure 4.3: Flow chart with the main steps of the preparation of the reduction

Furthermore, a temporary directory and the directory, where results are saved on disk are created.

The next step of the preparation is to cut off the last row in each raw image. The modified images are saved in a temporary directory. This step is necessary because the last row of the CCD in the blue channel is 0 or 32768. This defect has the effect that one obtains too large number of outliers when building the master bias, dark and flat field. The temporary directory with the modified images is deleted after the reduction procedure. This step can be left out, when a new camera without this defect is available.

Thereafter, the parameters and file names for reduction procedure are defined (Sect. 4.3). All reduction parameters are supplied with the same values to all routines called by the pipeline at the different steps of the reduction. This is made for consistency in the reduction. The parameter values are read out from the parameter file for the blue channel. The name of the file is parameter_blue.dat. The corresponding values of this parameters are given in Sect. 4.3.

The names of the master calibration images, the save files for the order definition and the offset for the ThAr spectra in comparison with a master ThAr spectra are defined. The name of the master calibration images and save files is composed of the inst_mode and type, for the master calibration images e.g. heros_blue.bias.fits and for the save files of the order definition e.g. heros_blue.ord.sav and for the result of the wavelength calibration e.g. heros_blue.wave.sav.

Furthermore, the file names for log and error file to control the reduction are defined. The names are composed of the inst_mode and the type of the message.

Additionally, during the procedure the file name for error files are defined. All possible file names and a small description for the blue channel follow:

heros_blue.*_change.ps: a plot of the relative variation in the bias, dark and flat field see (4.2.2)

heros_blue.mean_*.dat: the arithmetic mean and standard deviation of the single bias,
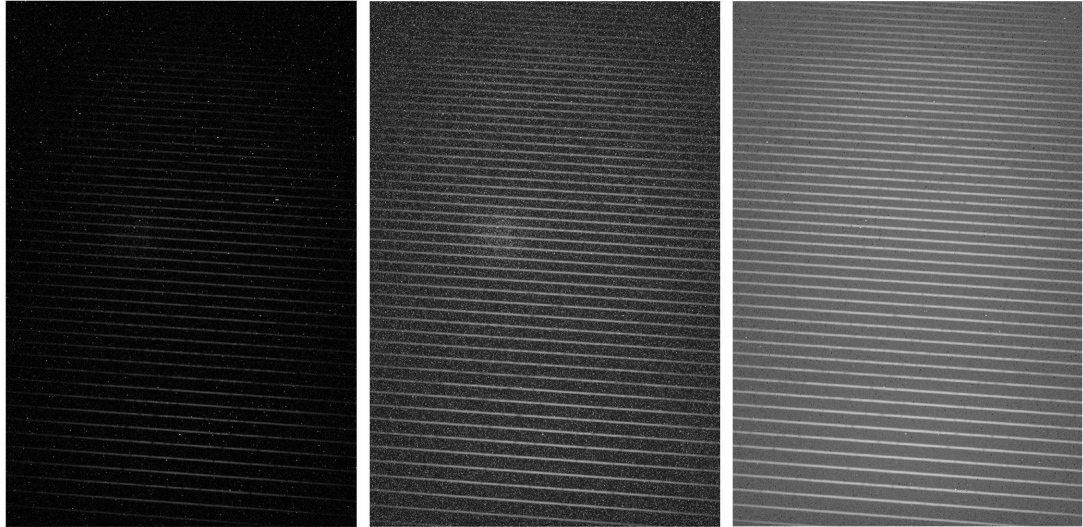
Figure 4.4: An example of the influence of the bias and dark correction whereas the dark background is caused by the high background counts, from left to right, the raw image, after the bias correction, after the bias and dark correction

dark and flat field

heros_blue.wave_log.dat: the arithmetic mean and the standard deviation of the ThAr spectrum shift and the arithmetic mean of the standard deviation and the standard deviation of the residuals of the wavelength calibration

heros_blue.*_error_message.txt: the reason why the program stops or the messages about a problem when building the master bias, dark and flat field

heros_blue.*_combine_error_message.txt: an error during the combination of bias, dark and flat field

heros_blue.order_error.txt if not a single order was found in the master flat field

heros_blue.thar_error_message.txt: message about the reason why the program stops at the extraction of the ThAr spectrum

heros_blue.wavecal_error_message.txt: the program cannot make the wavelength calibration automatically

heros_blue.sci_error_message.txt: science images not found

image name+.sci_error_message.txt: the reason why the spectrum is not extracted

image name+.sci_error_cosmic_info_message.txt: if the signal in the image is to faint

The images are sorted by type (bias, dark, flat field, ThAr and science) and collected in lists. Also it is determined, which make file will be used.

4.2.2 Building the master calibration images

The HRT system takes several calibration images: Bias, dark and flat fields, before and after the observations.

Bias: Image with closed shutter and exposure time zero.

Dark: Image with closed shutter and exposure time not equal to zero. This image is used
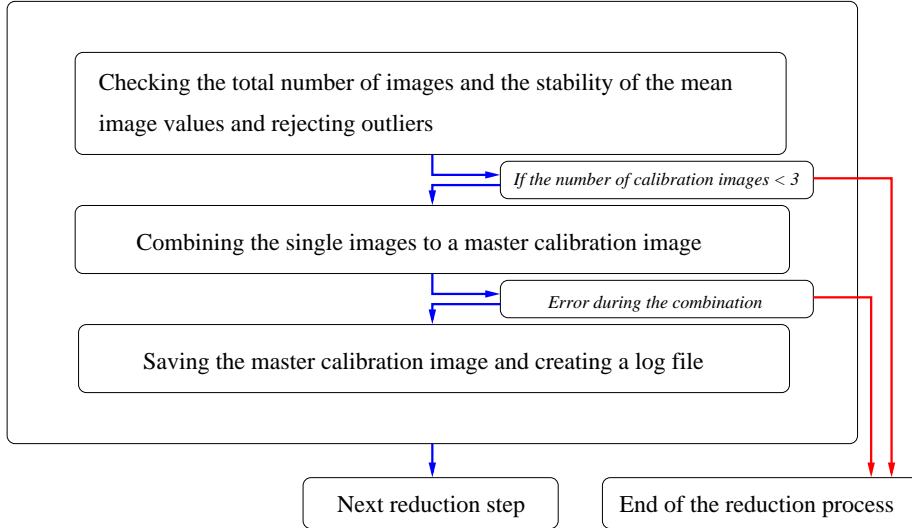
Figure 4.5: Flow chart with the main steps for building the master calibration images

to eliminate the dark current of the CCD camera.

Flat field: Spectrum of a continuum lamp. The flat field is used to define the order positions and the quantum efficiency correction.

The respective images are averaged and then used as master calibration images. The scientific images have to be corrected by bias and dark. All pixels in the image have a bias value which has to be corrected. In Fig. 4.4 (left image), one sees how the corrections influence the scientific images. In the left image, the raw image is shown. The spectral orders are only slightly visible. This is a contrast effect because the difference between the pixel values is not very high. After the bias correction, Fig. 4.4 (middle image), the orders are clearly visible. However, the image shows individual white pixel so that the image looks like grainy. This is caused by the dark noise. After the dark correction (Fig. 4.4 (right image)), the spectral orders are clearly visible and the dark noise is mainly eliminated. The average dark noise in the images is 20.01 ± 0.10 elec/600 sec. This high dark noise is caused by the fact that the CCD camera is only cooling to -25 C°.

The main steps to build the master image are similar for bias, dark and flat field. The flow chart in Fig. 4.5 shows the main steps of this part. The first step is to check the variation in the calibration images. The percentage of relative variation rv_i between the arithmetic mean of the single images $\langle im_i \rangle$ and the median of this values is calculated. The equation is:

$$rv_i = \left(\frac{\langle im_i \rangle - median(\langle im_1 \rangle ... \langle im_n \rangle)}{median(\langle im_1 \rangle ... \langle im_n \rangle)} \right) \cdot 100. \tag{4.1}$$

For the calculation of rv_i for the darks, the single images are corrected by bias and for the rv_i for the flats by bias and dark. The rv_i is plotted in a log file.

The calibration images are split in two lists. If the same number of images was taken before and after the observation, the images taken at the start of the observation are collected in the first list and those taken after the observation in the second list. Then, the percentage of relative variations of the images are checked for both lists. Normally,

the total number of images in both lists is greater or equal to 3. The standard deviations of the percentage of the relative variation of images (Eq. 4.1) is calculated for both lists and used as thresholds to build the master calibration image (Sect. 4.4.1). If the standard deviation is less than 3.5, then it is reset to the minimal threshold of combination 3.5.

If rv_i is greater than a threshold (Sect. 4.3), the corresponding image is not used for building the master calibration image. If the total number of images in one list is less than 3, an error message is obtained and the images are collected in a new list. The content of this new list is checked. Now there are 3 possibilities:

1. The total number of images is < 3: The reduction ends, because one needs at least 3 calibration images to build a master calibration image.

2. The total number of images < 6: The new list is not split in two lists and the REDUCE procedure *sumfits.pro* (Sect. 4.4.2), is used to build the master calibration image. The standard deviation of the percentage of relative variation is calculated for the list and used as threshold for the procedure *sumfits.pro*. If the standard deviation is less than 3.5, then the value is reset to the minimal threshold of combination 3.5. The procedure *sumfits.pro* (Sect. 4.4.2) adds the images directly. Thereafter, the summed image has to be normalised by the number of images. This image is trimmed and rotated with the REDUCE function *clipnflip.pro* (Sect. 4.4.4). It is used as master calibration image.

3. The total number of images ≥ 6: The new list is split in two lists and the procedure *sumimage_h.pro* (Sect. 4.4.1), is used to build the master calibration image. This possibility is similar the normal case, the only difference being is that the calibration images are not split in calibration images before and after the observations.

The single calibration images are averaged with the procedure sumimage_h.pro (Sect. 4.4.1).

As next step, it is checked if an error arose during the combination of the images and the keyword ''ERR'' (Sect. 4.4.1 and 4.4.2) was set. If the keyword set, then the pipeline stops and an error message is written to a file.

When building the master dark and flat field the image dimensions of average dark and flat field are compared with the image dimensions of the master bias. If the sizes are not equal, then the pipeline stops and an error message is written to a file.

The master bias is subtracted from the average dark and flat field and additionally, the flat field is corrected from the dark contribution. The dark correction is not performed if the arithmetic mean of dark is less than the threshold because in this case a dark contribution is negligible. After the subtraction of the master bias, the dark is time normalised.

The results are saved as master calibration images (hereafter, bias, dark and flat field). To monitor long-term changes the arithmetic mean of the single images and the corresponding standard deviation are saved in a log file. Furthermore, the standard deviation of the both lists and the arithmetic mean, the median and the standard deviation of the master calibration image are saved.
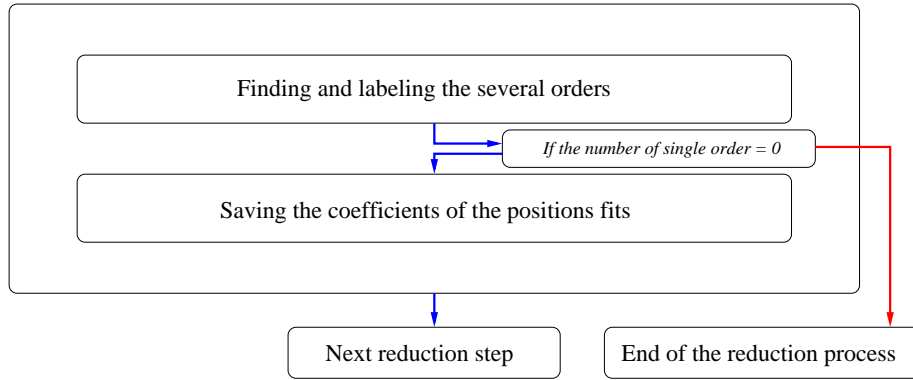
Figure 4.6: Flow chart with the main steps of the order definition

4.2.3   Order definition

The flat field is used for the order definition. The central positions of the individual spectral orders are located and defined. The flow chart Fig. 4.6 shows the main steps in this reduction part.

First the flat field and the mask image are loaded. The header of the mask image is modified with the function *modeinfo.pro* (Sect. 4.4.3). Then the mask image is trimmed and rotated with the function *clipnflip.pro* (Sect. 4.4.4). These steps are repeated for all images. For bias, dark and flat field these steps are already performed during their respective construction.

After the modification of the mask image, the order definition is done with the procedure *hamdord_h.pro* (Sect. 4.4.5). If the keyword ''ERR'' (Sect. 4.4.5) is set, then the pipeline
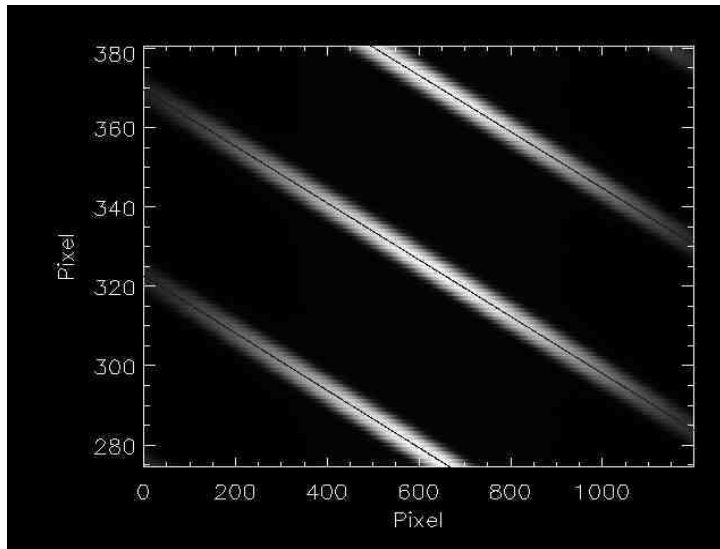
Figure 4.7: An example of the order definition where the white bands are the spectral orders 5,6,7 and the order positions are represented as solid line
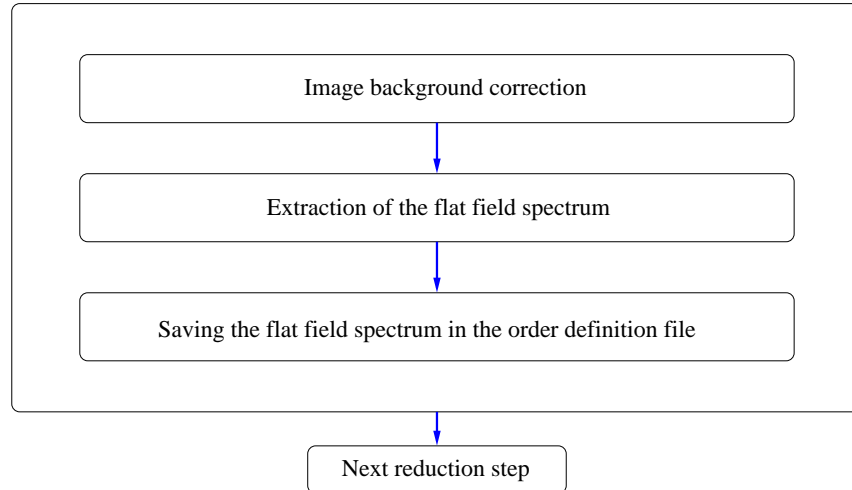
Figure 4.8: Flow chart with the main steps of the blaze extraction
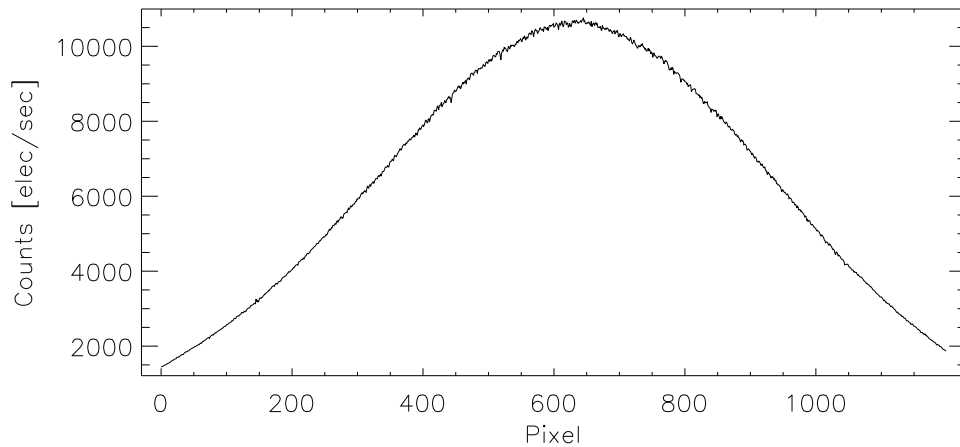
Figure 4.9: Extracted blaze from a flat field

stops and an error message is written to a file. In Fig. 4.7, an example of an order definition is shown. The white bands are a spectral order and the solid line represents the order centre. The results of the order definition are saved in the order definition file. Furthermore, the extraction width for each order is saved as array in the same file.

4.2.4 Blaze extraction

During the next step in the reduction pipeline the spectrum of the flat field lamp is extracted. The flow chart Fig. 4.8 shows the main steps in this part of the pipeline. This spectrum (hereafter, blaze) can be used as blaze function. The blaze function is the intensity distribution of the photons caused by the Échelle grating. The blaze is used to eliminate the blaze function in the science spectrum and to correct for the difference in
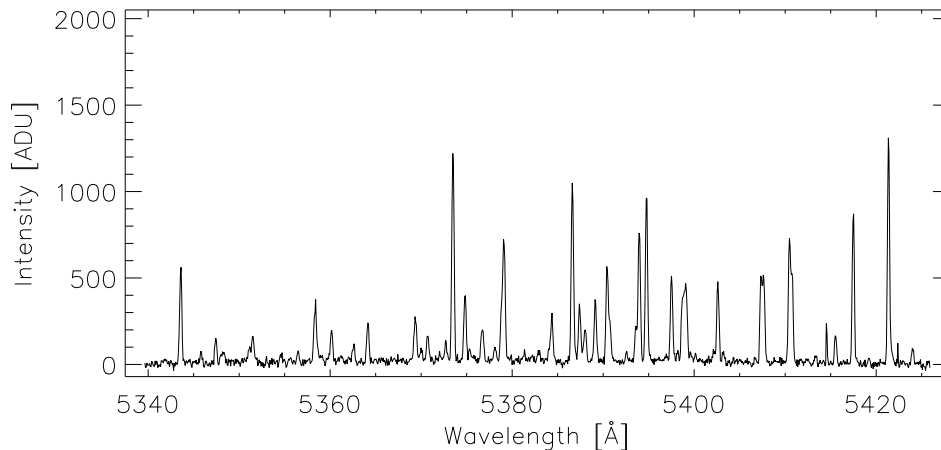
Figure 4.10: An example of a extracted ThAr spectrum

the quantum efficiency (Sect. 4.2.6.1) of the pixels.

For the extraction of the blaze, the order definition, the flat field and mask image are loaded. The mask header and image is modified with the functions *modeinfo.pro* (Sect. 4.4.3) and *clipnflip.pro* (Sect. 4.4.4). Thereafter the background in the image is corrected with the procedure *mk_scatter_h.pro* (Sect. 4.4.6). After background elimination, the blaze is extracted with the procedure *hamspec.pro* (Sect. 4.4.10). The extraction is performed using the method of the optimal extraction (Sect. 4.4.10.1). The counts in the blaze are converted from unit ADU (Analog Digital Unit) to electrons and the blaze is normalised by the exposure time. In Fig. 4.9, an example for the blaze is shown. The noise in the blaze is caused by the varying quantum efficiency of the pixels. At last, the blaze is saved in the order definition file.

4.2.5   Wavelength calibration

The spectrum of the Thorium-Argon (ThAr) lamp is used for the wavelength calibration. One ThAr image will be taken before and one after the observations. The flow chart Fig. 4.11 shows the main steps in this part. An example of an extracted ThAr spectrum is shown in Fig. 4.10. This spectrum is shown with the corresponding wavelength. The process of the wavelength calibration can be split in two parts: the spectrum extraction and the new wavelength solution.

4.2.5.1   ThAr spectrum extraction

The two ThAr spectra are reduced consecutively. The order definition, ThAr, bias, and dark images are loaded for the extraction. The headers of the ThAr image and the ThAr image itself are modified with *modeinfo.pro* (Sect. 4.4.3) and *chlinflip.pro* (Sect. 4.4.4). The bias is subtracted from the ThAr image. If the arithmetic mean of dark is above the threshold for dark subtraction, then the dark is also subtracted from the ThAr image. After that, the ThAr spectrum is extracted with the REDUCE procedure *hamspec.pro*
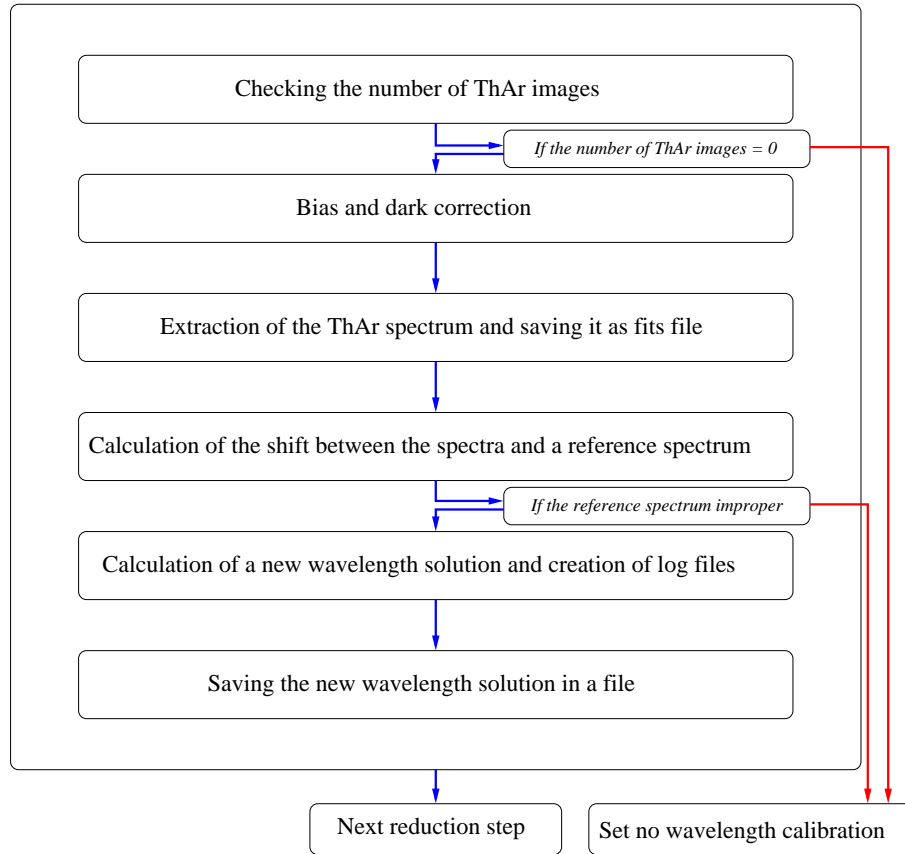
Figure 4.11: Flow chart with the main steps of the wavelength calibration

(Sect. 4.4.10). It uses the non-optimal extraction method (Sect. 4.4.10.2). Finally, the ThAr spectrum is saved.

4.2.5.2 Wavelength solution

For the automatic wavelength calibration, a reference ThAr spectrum with 1-D wavelength solutions for the several orders is used. The extracted spectra are compared with the reference spectrum. The shifts are calculated for each order via a cross correlation. The cross correlation is performed by the procedure *cross_corr_shift.pro* (Sect. 4.4.9). After that, the order shifts of the individual ThAr spectra are averaged for each order.

The new 1-D wavelength solutions of several orders are determined from the shifts and the 1-D wavelength solution of the reference spectrum. The procedure *auto_wavecal_1d.pro* (Sect. 4.4.13), is used to calculate the wavelength corresponding to each pixel. The results, the shifts and the spectral resolution of the reference ThAr spectrum are saved in a wavelength file.

To check the results, the procedure *auto_wavecal_1d.pro* creates plots with the residuals of the 1-D wavelength solution fits and a file containing the arithmetic mean and standard deviation of the shifts and the residuals of the 1-D wavelength solution.
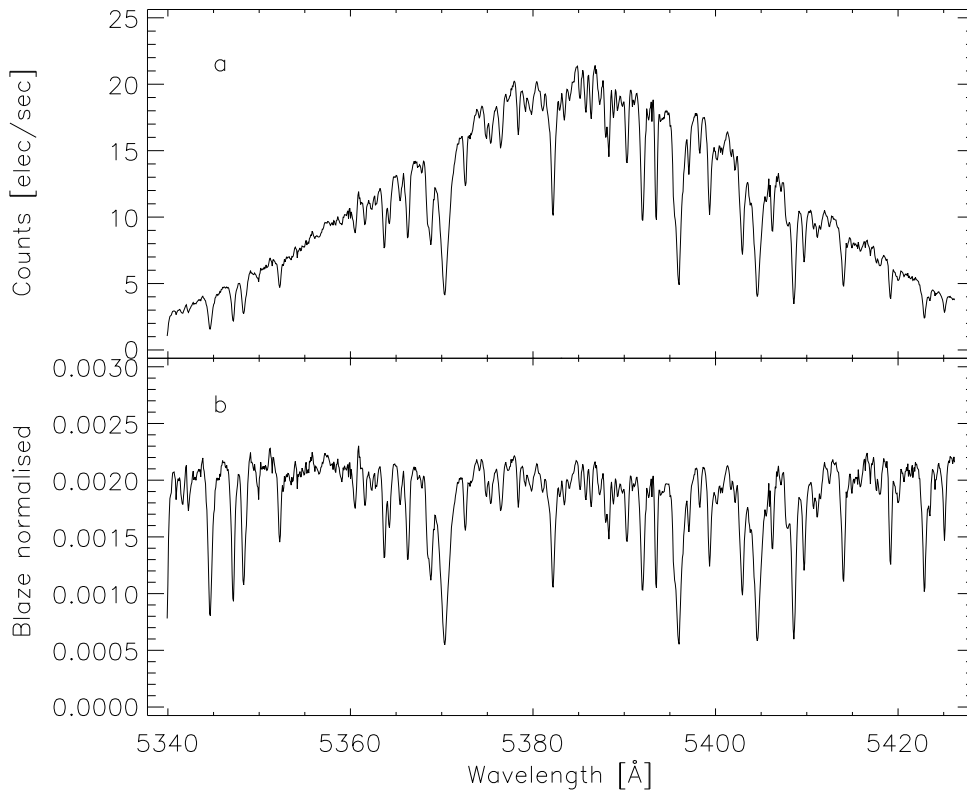
Figure 4.12: An example of an extracted star spectrum; a: without blaze normalisation; b: with blaze normalisation

4.2.6 Spectrum extraction

The final part of the pipeline is the spectra extraction. First, the spectra of all images are extracted. Thereafter, the images of the same object are co-added and a summed spectrum is created. In Fig. 4.12, an example of an extracted spectrum without and with a blaze normalisation are shown.

4.2.6.1 Spectrum from the single science image

The flow chart Fig. 4.16 shows the main steps in this part of the pipeline. The science images were collected in a list. The order definition, bias, dark, mask file and science image is loaded. If the keyword ''NOAUTOCAL'' was not set, then the wavelength file is loaded. The headers of the science and mask image are modified with the procedure _modeinfo.pro_ (Sect. 4.4.3) and _chlinflip.pro_ (Sect. 4.4.4). The bias is subtracted from the science image and if the arithmetic mean of dark is greater than the threshold for dark subtraction, then the dark is also subtracted from the science image. If sky images from this image (object) exist, then the average of two sky images is created and subtracted from the science image. Next, a background correction is performed with the procedure _mk_scatter_h.pro_ (Sect. 4.4.6). After the background correction, the procedure _cosmic_corr.pro_ (Sect. 4.4.7)
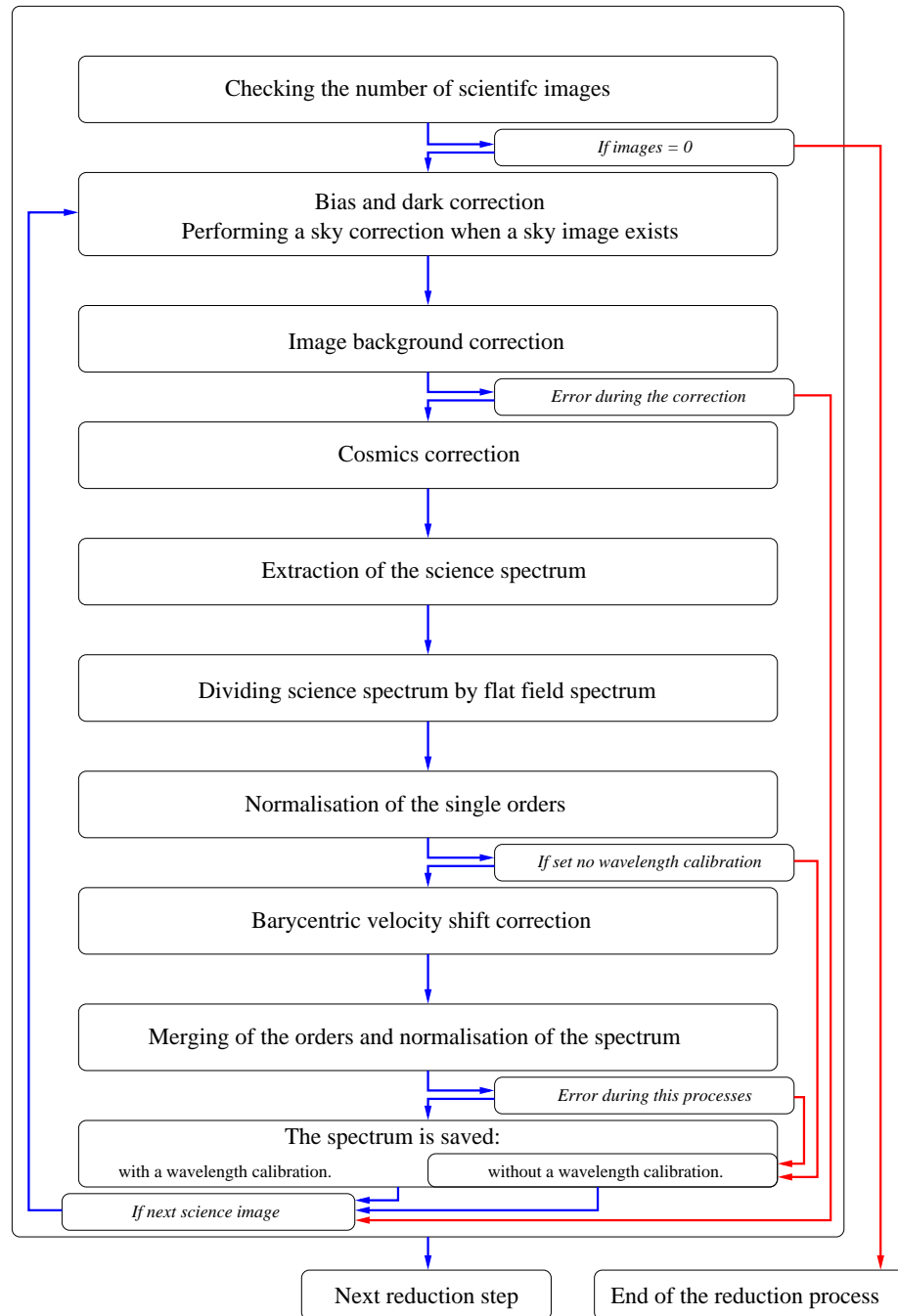
Figure 4.13: Flow chart with the main steps of the spectrum extraction from a single science image

identifies outliers in the science image and these are flagged in the mask file. Thereafter, the spectrum is extracted with the REDUCE procedure *hamspec.pro* (Sect. 4.4.10). The extraction is performed using the optimal extraction (Sect. 4.4.10.1). The counts in the spectrum are converted from the unit of ADU (Analog Digital Unit) to electrons and the
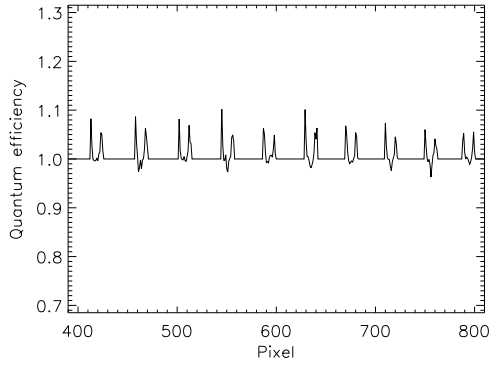
Figure 4.14: The values in the normalised flat field for column 600 in cross dispersion direction
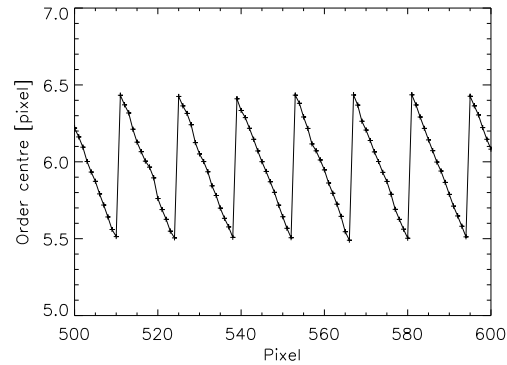
Figure 4.15: The variation of the order centre in the extracted relative order 6

spectrum is time normalised. Thereafter, the spectrum is divided by the blaze. This step eliminates the blaze function. Simultaneously, the correction for the quantum efficiency is achieved (Skoda and Slechta 2002).

Normally, this correction is done using a normalised flat field, but not in this pipeline. The reason is:

If one uses the REDUCE procedure for the normalisation, one obtains spikes in the order wings of the normalised flat field (Fig. 4.14). A reason for these spikes is that a small variance between data and order profile in the order wings has a larger relative effect than in the order centre. Furthermore, the centre of the average order profile is slightly shifted compared to the centre of the order because the position of the order centre is not fixed. The centre varies periodically around a mean centre (Fig. 4.15) because of the finite pixel size.

The simpler alternative method to make the correction for the quantum efficiency is to extract a spectrum from the flat field with the same method as the science spectrum and to divide the science spectrum by this spectrum.

Thereafter, the mean signal-to-noise is calculated and written to the header. In the next step, the separate orders of the spectrum are normalised with the procedure *cont_norm.pro* (Sect. 4.4.8). If the keyword ''NOAUTOCAL'' is not set, then the wavelengths for the individual object are corrected by the corresponding barycentric velocity shifts (bary_corr), with the equation from REDUCE procedure rdech.pro:

$$ wavelength \quad = \quad wavelength_{observed} \ \left(1 + \frac{bary\_corr}{c} \right) \tag{4.2} $$

The separate orders of the spectrum are merged to a total spectrum with the procedure *spec_merging_cont_norm.pro* (Sect. 4.4.11). After the extraction of the spectrum from the single science images, the spectrum from the co-added science images is extracted.
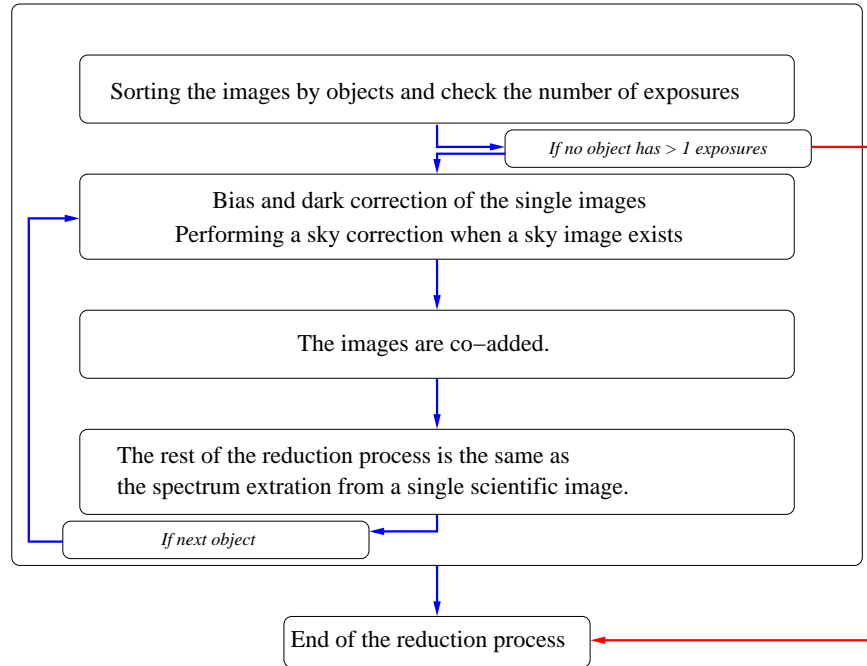
Figure 4.16: Flow chart of the first steps of the spectrum extraction of the co-added science images

4.2.6.2 Spectrum from the co-added science images

This is the last part of the reduction pipeline. The spectra from the summed science images of the same object are extracted. This reduction procedure is similar to the procedure to extract the spectrum from the single science image, but additionally, the images are co-added at first. The flow chart Fig. 4.16 shows the first steps in this reduction part. The rest is similar to the spectrum extraction of the single science images.

The first difference between both reduction steps is a check which objects have more than one exposure. These objects are collected in a list.

Another difference is the co-addition of the single images for the same object, after the bias and, if necessary, a dark and sky correction. The mean Julian date for the summed image and the barycentre velocity shift is computed. The velocity shift is calculated with the REDUCE procedure *helcorr.pro* (Sect. 4.4.12).

4.2.6.3 Storing the results

Finally, the extracted data are stored in the HRT archive in a fits format. The data is stored in the first extension and the structure is given in Table 4.1. The column noautocal in the Table 4.1 shows the data which is saved if the keyword noautocal was set. In the zeroth extension of the fits file, the image header is saved.

Structure name	data description	noautocal
wave	the wavelength array[data,order]	x
spec_blz	the blaze normalised spectrum array[data,order]	x
blaze	the blaze array[data,order]	x
sig	the signal to noise array[data,order]	x
spec_norm	the of one normalised spectrum array[data,order]	x
wave_merg	the merged wavelength array[data]	
spec_merg	the merged blaze normalised spectrum array[data]	
spec_merg_norm	the of one normalised merged spectrum array[data]	

Table 4.1: The data structure in first extension of the fits file

4.3   Parameters of the reduction pipeline

For the reduction, some parameters are necessary. These parameters are stored in two files. The single parameters and the corresponding values can be seen in Table A.1.

The first file is the REDUCE function *modeinfo.pro* (Sect. 4.4.3). Here, the following parameters are stored:

xr and yr: the trim ranges of the image in x-direction and y-direction

These define the area of the image which is used for the extraction and so the total wavelength range of the spectrum. At present, the wavelength range of the spectrum in the blue channel is 380 to 570 nm.

orient: the orientation of the image defines the rotation of the image (Sect. 4.4.4) which is necessary if the orders are horizontal to the x-axis

backn: a fixed background in the image, it is always set to 0

The second file is the parameter file parameter_blue.dat. In this file, the following parameters are defined:

xwd1: the number of pixels below the order centre

xwd2: the number of pixels above the order centre

The total extraction width is xwd1+xwd2+1. The one is for the order centre.

osample: the step size of the slit function when reconstructing a sub- pixel grid (Sect. 4.4.10.4)

sf_smooth: slit function smoothing parameter in cross dispersion direction (Sect. 4.4.10.4)

sp_smooth: spectrum smoothing parameter in dispersion direction (Sect. 4.4.10.4)

power: the order of the polynomial fit (Sect. 4.4.5)

swath_width: the number of columns where a constant PSF is assumed (Sect. 4.4.10.3)

The pipeline uses a relatively small swath width, because the spectrum jumps if the pipeline uses a large swath width. These jumps are very small in the current setup. One can see this, if the blaze extracted with the optimal extraction is divided by analysis the blaze extracted with non-optimal extraction. The Fig. 4.17 and Fig. 4.18 show the blaze fraction, where the swath width was 300 and 25 respectively. The swath width of 300 is used because one can see the jumps and also the pixel position of the jumps. The position of the jumps are a factor of the swath width. On the other hand, the swath width of 25 is the values which is used for the extraction. The jumps in Fig. 4.17 very small, but this effect is an error of the reduction. The reason for these jumps is unknown. With a small swath, these jumps are eliminated, see Fig. 4.18.
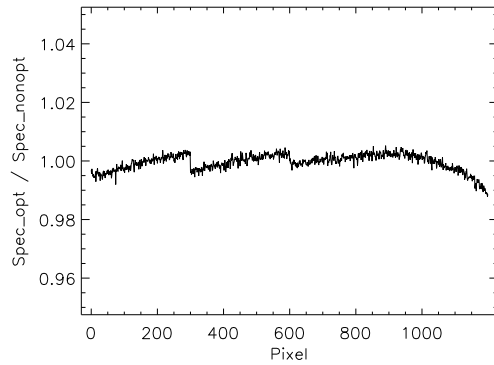
Figure 4.17: Blaze divided by blaze extract with the non-optimal extraction method and a swath width 300
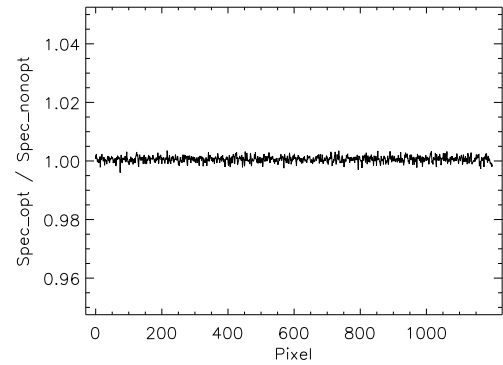
Figure 4.18: Blaze divided by blaze extract with the non-optimal extraction method and a swath width 25

thresflat, *dark, *bias: the maximum of the relative variations between the arithmetic mean of the single images and the median of these values (Sect. 4.4.1)

use_dark_thres: the value of the mean master dark, when the dark correction is performed

threscosmic: the threshold for the search for comics and outliers (Sect. 4.4.7)

filter: the sensitivity of order detection

min_order_size: the minimal order size in percent

order_width: order height used for the background determination

obase: the first absolute order

inst_mode: the spectrograph mode

master_thar: the full file name of the master ThAr spectrum

path_master_1d_solution: the directory of the sav files for the master wavelength solution

4.4 Important procedures and functions of the pipeline

This section includes a short description of the important individual procedures. Not all are REDUCE procedures and some REDUCE procedures are modified. The modified procedures are labelled with *_h*. The information about the REDUCE procedures are taken from the comments, an analysis of the source codes and Piskunov and Valenti (2002).

4.4.1 Procedure sumimage_h.pro

The procedure *sumimage_h.pro* combines individual bias, dark and flat field images to an average image and also identifies and replaces outliers. The syntax with all parameters and their description can be seen in Table 4.2.

The procedure *sumimage_h.pro* is based on the REDUCE procedure sumbias.pro. The

sumimage_h	, list1, list2, inst_mode, image, head, DEBUG=debug		
	, XR=xr, YR=yr, ERR=err, EXTEN=exten		
	, THRESH1=thresh1, THRESH2=thresh2,		
Parameter	Description	Optional	Default
list1	list of images taken before the observation		
list2	list of images taken after the observation		
inst_mode	the spectrograph mode		
image	the average image		
head	new header	yes	
DEBUG	keyword for information plots	yes	
XR	the values of the trim range [x_min:x_max]	yes	all
YR	the values of the trim range [y_min:y_max]	yes	all
ERR	output of a error message	yes	
EXTEN	fits extension	yes	0
THRESH1	threshold of combination	yes	3.5
THRESH2	threshold of combination	yes	3.5

Table 4.2: The input and output parameters of sumimage_h.pro

procedure sumbias.pro was modified and in the next paragraph there is a description of this procedure. Thereafter, the modifications are described.

4.4.1.1   REDUCE procedure sumbias.pro

The procedure *sumbias.pro* combines single bias images and identifies and replaces outliers. The images are collected in two lists. It is considered that the individual bias images are taken before and after the night time observation. In the list1, the images taken before the observation are collected and the images after the observation in list2. The images in both groups are added with the procedure *sumfits.pro* (Sect. 4.4.2). Then, the co-add images are rotated with the function *clipnflip.pro* (Sect. 4.4.4) and they are added. Next, an average image is built. Furthermore, it is searched for bad pixels and the noise in the combined image is calculated.
As first step, the results of both parts are normalised with the total number of the images in each part. Then, a difference image and a difference distribution is calculated. This distribution is a Gaussian and the standard deviation of the Gaussian the noise. Finally, the limiting values are determined, where the wings of the difference distribution become non-Gaussian. The pixels in the difference image with a value outside of the limiting values are defined as outliers. In the average image, the pixel values of this outliers are replaced with the lower values of a normalised image of the individual parts. The result of the process is now the average image.

4.4.1.2   Differences to sumbias.pro

The keywords ''THRESH1'', ''THRESH2'', ''WDEFAULT'' and ''NO_GAUSS_CORR'' were added. The new name sumimage shows that this procedure is used to combine the bias, dark and flat field images and not only the bias images.

sumfits	, list, inst_mode, sumimage, head, DEBUG=debug		
	, THRES=thres, WIN=hwin , MASK=mask		
	, XR=xr, YR=yr, ERR=err , EXTEN=exten		
Parameter	Description	Optional	Default
list	list of images to add		
inst_mode	the spectrograph mode		
image	the summed image		
head	new header	yes	
DEBUG	keyword for informational plots	yes	
THRES	threshold for bad pixels	yes	3.5
WIN	number of columns used to construct	yes	50.
	a probability function		
MASK	the mask file to use	yes	
XR	trim range [x_min:x_max]	yes	all
YR	trim range [y_min:y_max]	yes	all
ERR	output of error message	yes	
EXTEN	fits extension	yes	0

Table 4.3: The input and output parameters of the procedure sumfits.pro

The keyword ''`THRESH1`'' and ''`THRESH2`'' are thresholds for both calls of the sub-procedure *sumfits.pro* (Sect. 4.4.2). The procedure *sumbias.pro* does not set a threshold for the image combination with the procedure *sumfits.pro* and the default value of 3.5 is used.

If the keyword ''`WDEFAULT`'' is set, then the original calculation of the lower and upper limits used. This limit is the threshold, determining what pixels are used for the noise determination. This threshold is calculated:

$$\pm limit \;\; = \;\; \pm \; 5.0 \; \cdot \; median(|diff|) \tag{4.3}$$

Diff is the difference image of the co-added normalised images. If the keyword ''`WDEFAULT`'' is not set, then the following equation is employed:

$$\pm limit \;\; = \;\; \pm \; \sqrt{stddev(diff)^2 \; + \; thres1^2 \; + \; thres2^2} \; \cdot \; median(|diff|) \tag{4.4}$$

In this equation, the standard deviations of diff and the thresholds of the both image lists are considered. The keyword ''`NO_GAUSS_CORR`'' is used to switch off the correction where the wings of the difference distribution become non-Gaussian.

4.4.2 REDUCE procedure sumfits.pro

This procedure adds individual images and it also identifies and replaces outliers. The syntax and a description of the parameters are shown in Table 4.3. Before the outliers in the single images are identified and the images are co-added, the function *modeinfo.pro* is opened to modify each fits header.

Then, a median fit dependent on the pixel values is performed and a noise model is constructed. After this, the median is subtracted from the data and the result is compared to the threshold, given by the noise model multiplied by the input threshold (thres). If the data value is greater than this threshold, then it is replaced by the median.

newheader = modeinfo(header, inst_mode, XR=xr, YR=yr, ORIENT=orient , GAIN=gain, READN=readn, BACKG=backg, , TIME=time, RA2000=ra2000, DE2000=de2000 , JD=jd, OBSLON=obslon, OBSLAT=obslat , OBSALT=obsalt, HELCORR=helcorr)			
Parameter	Description	Optional	Default
header	input image header		
inst_mode	the spectrograph mode	yes	
xr	trim range [x_min:x_max]	yes	
yr	trim range [y_min:y_max]	yes	
orient	the orientation of the image for a rotation	yes	
gain	CCD readout gain	yes	
readn	readout noise	yes	
backn	background consisting of dark and sky	yes	
time	exposure time in sec	yes	
ra2000	right ascension in hrs	yes	
dec2000	declination in deg	yes	
jd	Julian date - 2400000	yes	
obslon	observatory longitude in deg	yes	
obslat	observatory latitude in deg	yes	
obsalt	observatory altitude in m	yes	
helcorr	barycentric correction in km/sec	yes	

Table 4.4: The input and output parameters of the function modeinfo.pro

4.4.3   REDUCE function modeinfo.pro

The function *modeinfo.pro* checks whether the spectrograph mode is valid or not. If the mode is valid, then it writes information required for the extraction E_* into the fits header. These information are collected in the corresponding spectrograph mode. The syntax and a description of the parameter are given in Table 4.4. The function *modeinfo.pro* was extended for both spectrograph modes for the HEROS spectrograph. The modes are called heros_blue and heros_red for the blue and red channel respectively. The spectrograph modes were included in the array valid_modes. Furthermore, some parameter were predefined under the spectrograph modes. These parameters and the corresponding values are see in Sect. 4.3. Under the spectrograph mode, the readout noise and gain are read out from the image header. Furthermore, the telescope coordinates and the altitude of the telescope are set. For each science image, the Julian date, object coordinate of the equinox 2000 and the proper motion are read out from the header.

With the object coordinate of the equinox 2000 and the proper motion the object coordinate at the epoch of the observation is calculated.

If the parameter obslon is not zero, then the function opens the procedure *helcorr.pro* (Sect. 4.4.12) to calculate the barycentric correction and the heliocentric Julian date.

newimage = clipnflip(image, header, XR=xr, YR=yr, ORIENT=orient)			
Parameter	Description	Optional	Default
newimage	image is rotated		
image	the image input		
header	image header	yes	
XR	the values of the trim range [x_min:x_max]	yes	
YR	the values of the trim range [y_min:y_max]	yes	
ORIENT	the orientation of the image for a rotation	yes	

Table 4.5: The input and output parameters of the function clipnflip.pro

Direction	Transpose	Rotation Counterclockwise	X1	Y1
0	No	None	X_0	Y_0
1	No	90°	$-Y_0$	X_0
2	No	180°	$-X_0$	$-Y_0$
3	No	270°	Y_0	$-X_0$
4	Yes	None	Y_0	X_0
5	Yes	90°	$-X_0$	Y_0
6	Yes	180°	$-Y_0$	$-X_0$
7	Yes	270°	X_0	$-Y_0$

Table 4.6: Rotation directions [IDL Help]

4.4.4 REDUCE function clipnflip.pro

The function *clipnflip.pro* rotates and trims the image. The syntax and a description of the parameter are given in Table 4.5.

The rotation orientation depends on the order trends in the image and the wavelength direction. The order trends have to be horizontal to the x-axis. If the keywords ''XR'', ''YR'' and ''ORIENT'' are not set, then the trim ranges and rotation direction are read from the image header (Sect. 4.4.3). The function uses the IDL function *rotate.pro* for the image rotation. The possible rotation directions are shown in Table 4.6.

4.4.5 Procedure hamdord_h.pro

The procedure *hamdord_h.pro* searches for the individual orders and gets the position of individual orders as the coefficients of a polynomial fit. The syntax and a description of its parameters are given in Table 4.7.

4.4.5.1 REDUCE procedure hamdord.pro

The procedure hamdord opens the REDUCE procedure *mark_orders.pro* to locate and to mark clusters. These clusters are the individual orders. After locating the orders, the procedure hamdord.pro determines the first and last absolute order of the cross-disperser. The procedure hamdord.pro checks the number of columns in the individual orders. If the total number of columns in the order is under 20% of the total number of image columns, then this order is rejected. The order is also rejected, when the middle part is outside the

hamdord_h	, im, orc, or_err=ome, or_range=orr, or_column=or_column		
	, cross_disperser=cross, power=opower, filter=filter		
	, PLOT=iplot, POLARIM=polarim, MASK=mask		
	, MANUAL=manual, NOISE=noise		
	, MIN_ORDER_SIZE=min_order_size, ERR=err		
Parameter	Description	Optional	Default
im	the image input		
orc	the location of the order output as		
	coefficients of a polynomial fit		
or_err	the rms for the individual order	yes	
or_range	the first and last order	yes	
	number assuming the specific		
	type of cross-disperser		
or_column	the first and last column for each order	yes	
cross_disperser	the type of cross-disperser	yes	grating
	grating or prism		
power	the power of the polynomial for	yes	2.0
	order fitting		
filter	the filter width for the detection	yes	20.0
	of orders		
PLOT	keyword for informational plot	yes	
	of the process		
POLARIM	polarimetric mode	yes	
MASK	the mask file use	yes	
MANUAL	merge all clusters in	yes	
	an interactive mode		
NOISE	the readout noise of the CCD	yes	
MIN_ORDER_SIZE	minimum number of columns in percent	yes	20.
ERR	get an error message	yes	

Table 4.7: The input and output parameters of the procedure hamdord_h.pro

range.

The values of the calculated first and last absolute order cannot be used because their values are too small in the HEROS spectra.

4.4.5.2   Differences to hamdord.pro

In the procedure *hamdord_h.pro*, the minimum number of columns in percent is not fixed (20%). The keyword ''MIN_ORDER_SIZE'' was added to set the minimum number of columns in percent. Furthermore, the keyword ''ERR'' was added to get an error message, if the procedure cannot find a single order in the flat field.

4.4.6   Procedure mkscatter_h.pro

The procedure *mkscatter_h.pro* determines the background in the image which is created by the scattered light in the spectrograph. The syntax of *mkscatter_h.pro* and a short

mkscatter_h	, im, orders, back, yback, colrange=colrange		
	, LAMBDA_SF=lam_sf, LAMBDA_SP=lam_sp		
	, SWATH_WIDTH=swath_width, OSAMPLE=osample		
	, MASK=mask, GAIN=gain, READN=rdnoise		
	, SUBTRACT=subtract, POLY=pol, DATA=back_data		
	, ORDER_WIDTH=order_width, DEBUG=debug		
	, ORDER_EXTRA_WIDTH=order_extra_width		
	, IMBACK=imback, ERR=err		
Parameter	Description	Optional	Default
im	the image input and the output		
orders	the location of the order as		
	coefficients of a polynomial fit		
back	fitted scattered light model	yes	
yback	the coordinates of the scattered light	yes	
colrange	the first and last column for each order	yes	
LAMBDA_SF	smoothing across dispersion	yes	1.
LAMBDA_SP	smoothing in dispersion direction	yes	
SWATH_WIDTH	the number of columns where	yes	400.
	a constant PSF is assumed		
OSAMPLE	the step size with in the slit function	yes	10
	to reconstruct a sub-pixel grid		
MASK	the mask file to use	yes	
GAIN	factor ADU to electrons	yes	1.
READN	Read out noise	yes	0.
SUBTRACT	keyword to subtract the background	yes	
POLY	keyword to use polynomial fit	yes	
	to determine the background		
	with the procedure mkscatterh.pro		
DATA	the non smooth scattered light data	yes	
ORDER_WIDTH	this parameter is a offset	yes	
	to determine the order height		
DEBUG	Keyword to plot	yes	
ORDER_EXTRA	to use the option	yes	1.
_WIDTH	ORDER_WIDTH		
IMBACK	the background image	yes	
ERR	output of an error message	yes	

Table 4.8: The syntax, the input and output parameters of the procedure mkscatter_h.pro

description are given in Table 4.8.

4.4.6.1   REDUCE procedure mkscatter.pro

To determine the background, the middle between the adjacent orders and the corresponding regions between both orders is determined. The region between the orders is
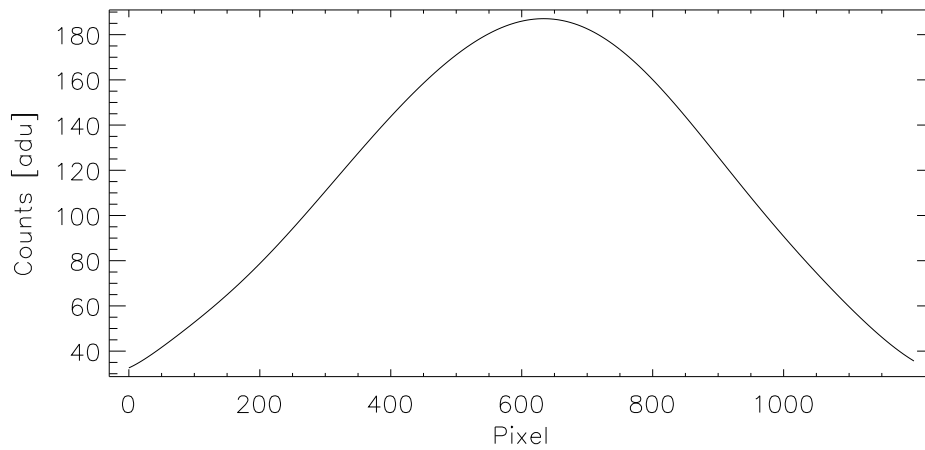
Figure 4.19: The background counts measured parallel to the relative order 6 and 7

Figure 4.20: The background image of a flat field image

determined with the procedure *slit_func.pro* (Sect. 4.4.10.4). The pixel values in the region between the orders are assumed to be the scattered light in the spectrograph. The average scattered light is calculated as the median of each column in this region and the median is smoothed. The Fig. 4.19 shows the background between the relative orders 6 and 7.

If the procedure cannot determine the region between the two orders, then it uses 5 pixels around the central line.

If the keyword ''SUBTRACT'' is set, then the background is determined for each pixel. The background for each pixel is calculated with a linear interpolation of the scattered light according to the column position. Afterwards, the background is subtracted from the input image. One point is very important. The background correction does not work if the swath width is smaller than the total number of pixels of the lowest order.

4.4.6.2 Differences to mkscatter.pro

The REDUCE procedure *mkscatter.pro* was modified to use primarily the keyword ''POL''. The keyword ''DOUBLE'' was rejected in the call to the REDUCE function *middle.pro* and *bottom.pro*. This keyword is not allowed in these functions.

If the keyword ''POL'' is set, then the REDUCE functions *middle.pro* and *bottom.pro* smooth the background data by a polynomial fit, before finally, the background is smoothed with a median fit. It is possible that the background value smoothed by a polynomial fit is below zero. These unphysical values are reset to zero.

If the keyword ''POL'' is not set, then the smoothing REDUCE functions *middle.pro* and *bottom.pro* use only a median fit to smooth the background data.

Furthermore, the keyword ''ORDER EXTRA WIDTH'' was added to use the parameter ''ORDER WIDTH''. The parameter ''ORDER WIDTH'' is an offset for the calculation of the order height. This has to be between 0<offset<2.0. If one does not set the keyword ''ORDER EXTRA WIDTH'', then the offset is 1 and the calculation is performed using the half order height.

Additionally, the keyword ''IMBACK'' and the creation of the background image were added, so that the background image is returned. The Fig. 4.20 shows the background image of a flat field image. In this example, the background is $\sim 11\%$ of the total number of counts [ADU].

Finally, the keyword ''ERR'' was added, so that one gets an error message.

4.4.7 Procedure cosmic_corr.pro

This procedure is used to identify outliers in the scientific image. The outliers are labelled, by setting the corresponding pixel in the mask file to zero. The syntax and a short keyword description are given in Table 4.9.

The first step is to check for negative pixel values in the science image. If the value is less than a threshold, then the pixel is labelled in the mask file. The threshold is calculated from the negative readout noise multiplied with the cosmic threshold thres (Table 4.9 ''THRES''). The outlier search is limited to the orders. To find outliers, three different methods are used.

In the first method, the arithmetic mean (m1) and standard deviation (stddev) are computed for all values in the image larger than a boundary value. This value is the readout

cosmic_corr	, image, mask, orders, xwd, col_range, READN=readn , GAIN=gain,THRES=thres, ERR=err		
Parameter	Description	Optional	Default
image	scientific image		
mask	mask file		
orders	location of the orders as coefficients of a polynomial fit		
xwd	the extraction width		
col_range	the range of the orders		
READN	the readout noise		
GAIN	CCD readout gain		
THRES	the threshold to find comics		4.5
ERR	output an informational message	yes	

Table 4.9: The syntax, the input and output parameters of the procedure cosmic_corr.pro

noise multiplied with the cosmic threshold. If the total number of useable pixels is larger than 5% of the total number of image pixels, then the new arithmetic mean (m2) is calculated with the values larger then the first arithmetic mean (m1). To identify outliers, a threshold value (tv) is calculated with the equation:

$$tv = m2 + (stddev \cdot thres) \tag{4.5}$$

All values in the images above the threshold value (tv) are labelled in the mask file as damaged.

If the total number of useable pixels is below 5% of the total number of image pixels, then an warning message is created and also this method is not used for the outlier search.

In the next method, the image is multiplied by the modified mask file. The single order and the corresponding part of the mask file are extracted. The median and the standard deviation of the columns in the single order are calculated. The pixel values in the column are compared with a threshold. The threshold is calculated from standard deviation multiplied with the cosmic threshold thres. If a pixel value is greater than this threshold, then the corresponding pixel in the mask file is set to zero.

The last method uses the initial part of the spectrum extraction (Sect. 4.4.10.4 for more information) and the modified mask file. The single order and the corresponding part of the mask file are extracted from the image. The slit function is formed and the spectrum is extracted for the order. To find outliers, a deviation (dev) is calculated with the Eq. 4.6. With the slit function and the spectrum, the pixel values are recalculated and they are compared with the original values. All values above dev multiplied with the cosmic threshold are labelled as damaged in the mask file.

Finally, the mask file is returned to the main procedure and used for the spectrum extraction.

4.4.8 Procedure cont_norm.pro

With this procedure, the single orders are normalised. The syntax and a short description are shown in Table 4.10. This process consists of two parts. In the first part, the trend in

cont_norm	, sp, sig, normspec, obase=obase, PLOT=iplot		
Parameter	Description	Optional	Default
sp	the blaze normalised spectrum		
sig	noise		
normspec	the normalised spectrum		
obase	order base		
PLOT	to get informational plot	yes	

Table 4.10: The syntax, the input and output parameters of the procedure cont_norm.pro

the spectrum is eliminated. The median of the spectrum values is calculated. The values above 90 % of the median are used for a linear fit. With the fit, the trend in the spectrum is eliminated.

After this, a second fit to eliminate a remaining trend is performed. For the fit, only the data points above 0.95 are used. Afterwards, it is checked checked how exact the spectrum is continuum normalised. The median is calculated for the data points above 0.95. If the median is less than 1.005, then the normalisation starts at the next order. If the median is greater than this boundary, then an iteration process starts until this boundary is reached or the iteration is greater than 8. In this iteration process, the median is calculated for the data points above 0.98 and the spectrum is divided by this median.

4.4.9 Procedure cross_corr_shift.pro

This procedure is a composition of two IDL standard functions to calculate the shift between two ThAr spectra. These are the IDL function *c_correlate.pro* and the IDL function *gaussfit.pro*. The syntax of *cross_corr_shift.pro* and the parameter description are given in Table 4.11.

The IDL function *c_correlate.pro* computes the cross correlation between both spectra. The correlation values at a given vector of shifts are returned. In our case, one can assume that the shift between both spectra is small. The values of the given shifts range from -10 to 10 pixel. The distribution of the correlation values is a Gauss distribution

cross_corr_shift	, s1, s2, shift, WIDTH=steps, PLOT=iplot, NTERMS=interms , SIG_SHIFT=sig_sh		
Parameter	Description	Optional	Default
s1	first spectrum		
s2	second spectrum		
shift	the signal between the both spectra		
WIDTH	maximum of pixel in the positive direction	yes	10.
PLOT	to get a informational plot	yes	
NTERMS	Gauss parameter 3-6	yes	6
SIG_SHIFT	Error of the shift	yes	

Table 4.11: The syntax, the input and output parameters of the cross_corr_shift.pro

around 0. The position of the distribution maximum is the shift between both spectra. To compute the distribution maximum, the IDL function *gaussfit.pro* is used. The sign of the shift shows in which direction the second spectrum is shifted. If the sign is negative, then the spectrum is blue shifted and if the sign is positive, then the spectrum is red shifted.

4.4.10   REDUCE procedure hamspec.pro

The procedure *hamspec.pro* is used for the extraction of the spectrum. In Fig. 4.9, the extracted spectrum of the relative order 6 out the flat field (blaze) is shows. The syntax and a description of its parameters are given in Table 4.12. For the spectrum extraction, the procedure *hamspec.pro* opens the procedure *getspec.pro* (Sect. 4.4.10.1). To extract a spectrum, the extraction methods non-optimal and optimal extraction are available.

The non-optimal extraction is used if the keyword ''THAR'' is set at the procedure *hamspec.pro*. The procedure *getspec.pro* opens the procedure *getarc.pro*, (Sect. 4.4.10.2) for the non-optimal extraction method.

The optimal extraction is the more accurate method to extract the spectrum in comparison to the non-optimal extraction. The concept of the optimal extraction was introduced by Horne (1986). At the optimal extraction, the spatial profile of the order is used to find outliers in the spectrum. The REDUCE package uses a form of optimal extraction which was developed by Piskunov (Piskunov and Valenti 2002). The difference between the methods of Horne and Piskunov is the way to determine the spatial profile. Horne uses a polynomial fit to determine the spatial profile for each wavelength (Horne 1986). The method by Piskunov uses the spatial profile for each wavelength, which is determined with an empirical mean spatial profile, see Sect. 4.4.10.4. In the optimal extraction, the procedure *getspec.pro* opens the procedure *mkslitf.pro* (Sect. 4.4.10.3). This procedure opens the procedure *slit_func.pro* (Sect. 4.4.10.4).

In the following sections, descriptions of these procedures are given.

4.4.10.1   REDUCE procedure getspec.pro

With this procedure, the method of extraction is selected and the corresponding procedure is opened. The procedure extracts the single order from the image and passes it to the sub-procedure.

The spectra of the single order is returned to the procedure *hamspec.pro*.

4.4.10.2   REDUCE procedure getarc.pro

The procedure *getarc.pro* adds the pixel values inside the extraction width for each column and the result is the spectrum. This method is not so accurate because one obtains outliers in the spectrum.

4.4.10.3   REDUCE procedure mkslit.pro

The order is split into several parts. These parts are called swath width. The number of columns is given in the parameter ''SWATH WIDTH''. In the swath width, the PSF is assumed to be constant. The single parts are passed to the sub-procedure *slit_func.pro* (Sect. 4.4.10.4) and here, the extraction is performed. After the extraction, the separate

hamspec	, im, head, orc, dxwd, dsxwd, obase, spec		
	, ThAr=thar, LONG=long, SIG=sunc, COLRANGE=colrange		
	, SF_SMOOTH=sf_smooth, SP_SMOOTH=sp_smooth		
	, OSAMPLE=osample, SWATH_WIDTH=swath_width		
	, PLOT=iplot, MASK=mask, ORDER_RANGE=order_range		
	, TELLURIC=telluric, FILENAME=filename		
	, BLAZE_CONT=blaze_cont, SLIT_TILT_FILE=slit_tilt_file		
Parameter	Description	Optional	Default
im	the image		
head	the header of the image		
orc	the location of the order as		
	coefficients of a polynomial fit		
dxwd	the extraction width		
dsxwd	error of dxwd, but it is unused		
obase	order base, it is unused		
spec	the output spectra		
ThAr	keyword for the ThAr spectra	yes	optimal
	no optimal extraction		extraction
LONG	keyword for long slit spectra	yes	
SIG	noise of the spectra	yes	
COLRANGE	the first and last column for each order	yes	
SF_SMOOTH	smoothing across dispersion	yes	1.
SP_SMOOTH	smoothing in dispersion direction	yes	0.
OSAMPLE	the step size of the slit function	yes	14.
	to reconstruct a sub-pixel grid		
SWATH_WIDTH	the number of columns where	yes	
	a constant PSF is assumed		
PLOT	keyword to plot	yes	
MASK	to use the mask file	yes	
ORDER_RANGE	the range of orders	yes	all
	to extract		
TELLURIC	offset to order centre	yes	
FILENAME	print, the name in the plot	yes	
BLAZE_CONT	keyword to fix the blaze if	yes	
	discontinuities appear for		
	high-curvature orders.		
SLIT_TILT_FILE	keyword to use a 2D	yes	
	slit function		

Table 4.12: The syntax, the input and output parameters of the hamspec.pro

parts of the order are merged to a total spectrum of the order and returned to the *get-spec.pro*.

The Fig. 4.21 shows a control plot of the spectrum extraction, which is produced, if the keyword ''PLOT'' is set in the procedure *hamspec.pro*. The upper plots in Fig. 4.21 represent the slit function (dotted line, in the original plot solid line) and the data points
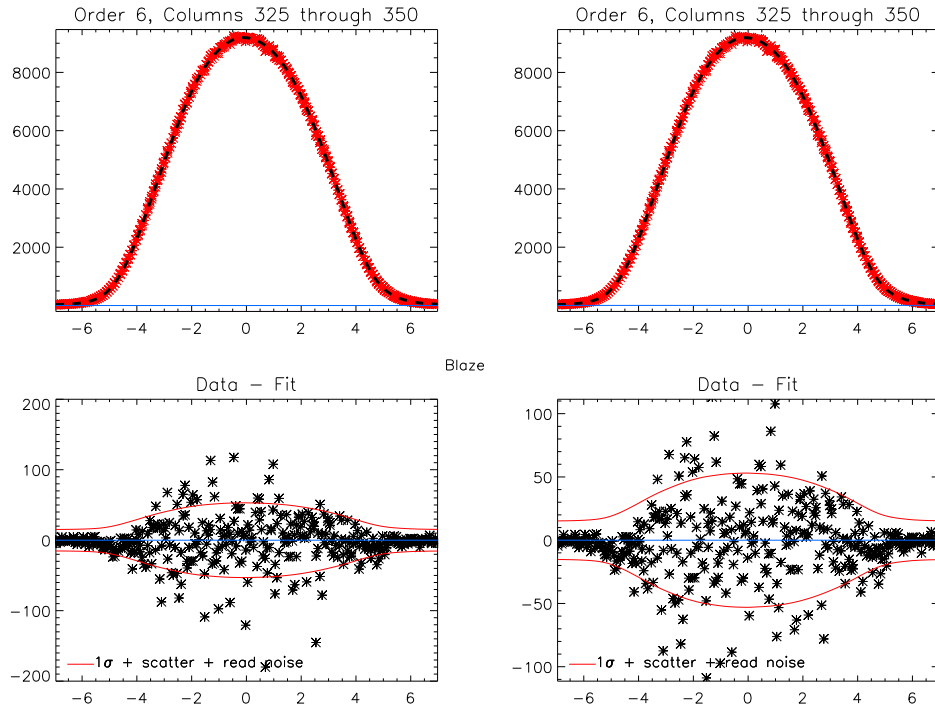
Figure 4.21: Control plot of the extraction produced by the procedure mkslit.pro, in the upper plots the slit function and in the lower plots the residuals between the data and the spectrum multiplied with the slit function

(asterisk, in the original plot dots), which were used for creating the slit function. The title shows the order and the column of the extraction. The lower plots show the residuals between the data and the spectrum multiplied with the slit function. The line represents the 1σ error plus the noise and the scatter. The x-axes in the plots are the extraction width. In the middle between the upper and lower plot is the file name of the corresponding image.

4.4.10.4   REDUCE procedure slit_func.pro

This procedure performs the extraction and also labels bad pixels. The extraction is conducted in two steps.

In the first step, the total sum of each row in an order is determined and these values are smoothed with a median fit. Afterwards, this array is divided by the sum of all pixel values. This is called spatial profile or slit function, the profile across the order. The pixel values are weighted with the slit function and these values are added for each column. Then, this spectrum is smoothed. Now outliers are found and defined. A deviation (dev) are determine with the equation:

$$dev \quad = \quad \sqrt{\frac{\sum \left(mask \; (imm - imm_{reconstruct})^2\right)}{\sum mask}} \tag{4.6}$$

The imm is the original image part and imm$_{\text{reconstruct}}$ is the corresponding reconstructed part. The reconstruction is performed with the spectrum multiplied by the slit function. The mask is corresponding part of mask file. The deviation is multiplied by three and compared with the difference between the pixel value and the spectrum values multiplied with the slit function. If the difference is greater than this threshold, then the corresponding pixels are marked.

In the second step, the slit function is re-determined. The supporting points of the slit function are oversampled so that one gets a new smoothed slit function with more supporting points. For this, the Tikhonov[1] regularisation is used.

The Tikhonov regularisation is a linear regularisation method which measures the difference between the adjacent pixels (Press et al. 1992; Wolter 2004). The vector notation is (Press et al. 1992):

$$(A^T A + \lambda H)\vec{u} = A^T \vec{b} \tag{4.7}$$

where A represents a $n \times m$ data matrix, $\vec{u}$ a set of parameters and $\vec{b}$ is a vector of observational data. These are the same elements used for the minimisation with the least square method. The matrix H (4.8) is a $m \times m$ matrix and it is the first order of the Tikhonov regularisation function (Press et al. 1992; Wolter 2004).

$$H = \begin{pmatrix}
1 & -1 & 0 & 0 & 0 & 0 & \cdots & 0 \\
-1 & 2 & -1 & 0 & 0 & 0 & \cdots & 0 \\
0 & -1 & 2 & -1 & 0 & 0 & \cdots & 0 \\
\vdots & & & & \ddots & & & \vdots \\
0 & \cdots & 0 & 0 & -1 & 2 & -1 & 0 \\
0 & \cdots & 0 & 0 & 0 & -1 & 2 & -1 \\
0 & \cdots & 0 & 0 & 0 & 0 & -1 & 1
\end{pmatrix} \tag{4.8}$$

The parameter λ is a regularisation parameter. The Eq. (4.7) can be solved (Press et al. 1992):

$$\vec{u} = \left(\frac{1}{A^T A + \lambda H} A^T A \right) A^{-1} \vec{b} \tag{4.9}$$

The oversampling factor for the slit function is defined by the parameter ''OSAMPLE''. The parameters ''SF_SMOOTH'' and ''SP_SMOOTH'' define the smoothing in cross dispersion direction and in dispersion direction respectively.

This process stops at one of the following points: at the maximal number of iterations or a cutoff value. The maximum number of iteration is 8 and the cutoff value is $1.0 \cdot 10^{-5}$. This value is calculated:

$$\frac{\max | spectrum_i - spectrum_{i-1} |}{\max \; spectrum_i} \tag{4.10}$$

The index i is the number of the iteration. With the second iteration, outliers are located and the positions of the outliers are fixed in the mask array. This new mask array is used in the next iteration for the identification of bad pixels.

The result is returned to the REDUCE procedure *mkslitf.pro.*

---

[1] A.N.Tikhonov, Russian mathematician 1906-1993

spec_merging_cont_norm	, wave, spec, blaze, head, wavem, specm		
	, specm_norm, PLOT=iplot, DEBUG=debug, ERR=err		
Parameter	Description	Optional	Default
wave	the wavelength		
spec	the blaze normalised spectrum		
blaze	the blaze array		
head	the image header		
wavem	the merged wavelength array		
specm	the merged blaze normalised spectrum		
specm_norm	the normalised merged spectrum		
PLOT	to get a informational plots	yes	
DEBUG	print information to debug	yes	
ERR	output of a error message	yes	

Table 4.13: The syntax, the input and output parameters of the procedure spec_merging_cont_norm.pro

4.4.11 Procedure spec_merging_cont_norm.pro

This procedure includes two functions. The first function merges the single orders to a total spectrum. The second function performs a continuum normalisation of the total spectrum. The syntax and a description of its parameters are given in Table 4.13.

4.4.11.1 Merging the single orders

The overlap in the neighbouring orders, (order n and n-1) is estimated. Then, the data of the order n-1 is adapted on the wavelength grid of order n. In the order n are more wavelength points because the dispersion is smaller. Next, it is checked, where the count number in the overlap is smaller than the readout noise. This data point is set to 0. In both overlaps, the weights of the wavelength points are calculated for the spectrum and the blaze. The weight is calculated as follows:

$$weight1_i = \frac{overlap1_i}{(overlap1_i + overlap2_i)} \, 100 \tag{4.11}$$

$$weight2_i = \frac{overlap2_i}{(overlap1_i + overlap2_i)} \, 100 \tag{4.12}$$

The singular weight of the blaze counts is compared with the counts in the spectra to find outliers. If an outlier is detected, then the corresponding weight is set to 0 and the weight for this wavelength point in the other order is set to 100. Furthermore, if weight1 < 10, then weight1 is set to 0 and weight2 to 100 and the other way around. Next, the values of the blaze normalised spectra are weighted and a mean value is calculated for the corresponding wavelength points. This mean value replaces the values in the order n and the end of the overlap region is put in an array. The single orders are sorted, so that the wavelengths increase with rising relative order and also the corresponding ends of the overlap regions are sorted. Then, only the data with a longer wavelength than the end

helcorr	, obs_long,obs_lat,obs_alt,ra2000,dec2000,jd, corr,hjd,DEBUG=debug		
Parameter	Description	Optional	Default
obs_long	Longitude of the observatory in [°] (East is negative)		
obs_lat	Latitude of the observatory in [°]		
obs_alt	Altitude of the observatory in [m]		
ra2000	Right ascension of the object in [h]		
dec2000	Declination of the object [°]		
jd	Average Julian date of the exposure		
corr	Barycentric velocity		
hjd	Average heliocentric Julian date of the exposure		
DEBUG	keyword to print the results	yes	

Table 4.14: The syntax, the input and output parameters of the procedure helcorr.pro

of the overlap region are put in a new array. After the merging of the single orders, the spectrum is continuum normalised.

4.4.11.2 Continuum normalisation of the total spectrum

This procedure tries to find a quasi-continuum in the spectrum. This continuum area is used to estimate sampling points for the normalisation.

First, it searches for strong outliers employing a median fit. Second, the difference between spectrum and median fit is calculated. After this, the standard deviation of these residuals is calculated. Finally, the procedure checks whether residuals are greater than the standard deviation multiplied by the factor 10. This factor 10 is selected to secure that here only very strong outliers are detected and not variations caused by the median fit. If an outlier is detected, the values in the spectrum and the wavelength grid are set to 0. The spectrum is split in parts and in each part the maximum in the spectrum is searched for. If the maximum is in the first or last part of the spectrum, then a polynomial of the order 2 is fitted to the logarithm of the maximal values. Then, the spectrum is divided by this fit. If the maximum is not in the first or last step then it is checked if the difference between two maxima is greater than 10 Å. If the difference is less than 10 Å, then the smaller wavelength point is rejected as sampling point. After this selection, the median is computed in the range of ± 50 pixels around the sampling point. Then, an interpolation between these points is made and the spectrum is divided by this result.

In the last step of the normalisation, the regions are defined, which are used as quasi continua. The quasi continuum is cut into parts, where the median of the data and the corresponding wavelengths are estimated. This number depends on the length of the continuum. With the median and the corresponding wavelength points, the date points from the original wavelength grid are interpolated. This is performed with a quadratic interpolation. Finally, the blaze normalised spectrum is divided by these data. The results are returned as normalised spectrum.

auto_wave_cal_1d	, data, path_master_1d_solution, npix, nord, wave , stdevreswave, LOG=ilog , NAMETXT=nametxt, NAMEPLOT = nameplot		
Parameter	Description	Optional	Default
data	Order shifts		
path_master_1d_solution	Path of the sav files of		
	the master wavelength solution		
npix	Number of Pixels		
nord	Number of Orders		
wave	Wavelength solution		
stdevreswave	Standard deviation		
	of the fit residuals		
LOG	Keyword to create log files		
NAMETXT	Name of the text log files		
NAMEPLOT	Name of the plot log file		

Table 4.15: The syntax, the input and output parameters of the procedure auto_wavecal_1d.pro

4.4.12   REDUCE procedure helcorr.pro

This procedure calculates the barycentric correction and the heliocentric Julian date. The syntax and a description of its parameters are given in Table 4.14. The barycentric correction is a correction for the rotation of the Earth, the rotation of the Earth's centre about the Earth-Moon barycentre and the rotation of the Earth-Moon barycentre about the solar centre.
The procedure considers the precession correction of the coordinates of the epoch 2000 to the epoch of the observation. The projection of the rotational, barycentric velocity along the line of sight is calculated. The barycentric correction is the sum of the projection of the rotational and barycentric velocities along the line of sight.

4.4.13   Procedure auto_wavecal_1d.pro

The procedure *auto_wavecal_1d.pro* calculates the wavelength points of the corresponding pixels in each order. The syntax and a description of its parameters is given in Table 4.15. To calculate the new wavelengths, the 1D wavelength solution of the master ThAr spectrum is used. The sav files of the 1D wavelength solutions include the pixel position of the line centre and the corresponding laboratory wavelength for each order. Furthermore, the coefficients of the polynomial fit are included and the order of the fit.
To obtain the new line centres in the single orders, the shift of this order is added to the corresponding pixel position of the line centres from the master ThAr spectrum. Thereafter, the laboratory wavelength and corresponding new line centre are fitted with the same order as in the 1D wavelength solution.
If the keyword ''LOG'' and the keywords ''NAMETXT'' and ''NAMEPLOT'' are set, then the residuals of the fit are plotted and the arithmetic mean of the shift and residuals of the fit and the corresponding standard deviation are written in a file.

wavecal	, file, save=savefile		
Parameter	Description	Optional	Default
file	the ThAr spectra with the file suffix ech		
save	the savefile of the possible 2D wavelength solution	yes	

Table 4.16: The syntax, the input and output parameters of the wavecal.pro

4.5 Manual wavelength calibration with the REDUCE procedure wavecal.pro

With the procedure *wavcal.pro*, one can perform a manual wavelength calibration. This procedure is not a component of the reduction pipeline, but with this procedure one produces reference 1D wavelength solutions. These solutions for single orders are stored in a sav file and the automatic wavelength calibration uses these sav files to create a new wavelength solution. The manual wavelength calibration is performed as follows:

4.5.1 1D wavelength solution

The ThAr spectrum is extracted with the HEROS pipeline without the automatic wavelength calibration and the suffix .ech is added to the fits files. This ending is specific to REDUCE and necessary to use *wavecal.pro*. The syntax and the parameters are given in Table 4.16.

At first, one quotes the absolute number of the base order in the field "Base order number" and the increment of orders in the field "Order increment". One selects an order and pushes the button "1D solution". A pop-up window appears and here one gives the wavelength range of the reference ThAr spectra and the absolute order. Thereafter, one can see the calibration ThAr spectra in the window. With button "Show ThAr", the reference ThAr spectra in the bottom of the window opens or closes and so it is possible to compare both spectra and identify several lines. At the top right side of the GUI are two controllers to zoom the spectra in or out. If one selects a line, it is opened a pop-up window with a line fit and a wavelength list. From this list, one can select the wavelength. Following a successful 1D wavelength solution, one can push the button "Compute" and in a pop-up window, one can check the accuracy of the solution. One can set the order of the fit with the option "Polynom power". One performs this process for each order and the resulting 1D wavelength solution is saved in a savefile.

After the second 1D wavelength solution, the procedure *wavecal.pro* builds a 2D wavelength solution, see Sect. 4.5.2 and estimates the remaining 1D solutions. If one has a 2D solution, one can see the residuals of this solution in a pop-up window. In this window, one can reject data points to improve the 2D solution and one has a wavelength solution for each order. This solution is saved as a sav file with informations about the wavelength points.

If a science spectrum was saved with the REDUCE saving procedure wdech.pro, it is possible to use the 2D wavelength solution to calibrate this science spectrum. For this purpose, one presses the button "Add 2D to ECH" and select this spectrum.

4.5.2   2D wavelength solution

The 2D wavelength solution is a fit dependent on the line centre, laboratory wavelength and order. The fit method is the Marquardt method, also called Levenberg-Marquardt method, and is a nonlinear least-squares fit. Before the Marquardt method is described, I want to give the necessary equations for the Marquardt method:
The χ^2 is (Press et al. 1992):

$$\chi^2(a) \;=\; \sum_{i=1}^{N} \left[\frac{y_i - y(x_i; a)}{\sigma_i} \right]^2 \tag{4.13}$$

The $y(x_i; a)$ is the model with the sampling points x_i and the parameter a, which describes the measured data y_i. The gradient of χ^2 is defined (Press et al. 1992):

$$\beta_k \equiv -\frac{1}{2} \frac{\partial \chi^2}{\partial a_k} \tag{4.14}$$

The Hessian matrix of χ^2 is defined (Press et al. 1992):

$$\alpha_{kl} \equiv \frac{1}{2} \frac{\partial^2 \chi^2}{\partial a_k \partial a_l} \tag{4.15}$$

One can combine the gradient and Hessian matrix to a set of linear equations (Press et al. 1992)

$$\beta_k \;=\; \sum_{l=1}^{M} \alpha_{kl} \delta a_l \tag{4.16}$$

$$\delta a_l \;=\; \text{constant} \times \beta_l. \tag{4.17}$$

For the Marquardt method δa_l is defined as (Press et al. 1992):

$$\delta a_l \equiv \frac{1}{\lambda \alpha_{ll}} \beta_l \Rightarrow \lambda \alpha_{ll} \delta a_l = \beta_l \tag{4.18}$$

with the fudge factor λ. Also one defines a new matrix α' Press et al. (1992):

$$\begin{aligned} \alpha'_{jj} &\equiv \alpha_{jj}(1+\lambda) \\ \alpha'_{jk} &\equiv \alpha_{jk} \qquad (j \neq k) \end{aligned} \tag{4.19}$$

The matrix α_{kl} (4.15) in equation (4.16) is replaced with the new matrix α' (4.19) so that β_k is Press et al. (1992):

$$\beta_k \;=\; \sum_{l=1}^{M} \alpha'_{kl} \delta a_l \tag{4.20}$$

The Marquardt method is an iterative method Press et al. (1992):

1. In the first step the $\chi^2(a)$ with an initial set of parameters a is calculated.

2. In the second step one selects a value for the fudge factor λ, e.g., $\lambda = 0.001$.

3. In the third step one solves the equation (4.20) for δa and then estimates the $\chi^2(a + \delta a)$.

4. In the last step one evaluates the $\chi^2(a + \delta a)$.

   (a) Is the $\chi^2(a + \delta a) \geq \chi^2(a)$ then the factor λ is increased by a reasonable factor of e.g., 10 and then the procedure goes back to the third step.

   (b) Is the $\chi^2(a + \delta a) < \chi^2(a)$ then the factor λ is reduced by a reasonable factor of e.g., 10 and the trial solution $a \leftarrow a + \delta a$ updates. After this one goes back to the third step.

It is necessary to define a boundary condition to stop the iteration process. The boundary condition for the 2D wavelength solution is a fractional change of the $\chi^2(a)$ of 0.001 or less.

4.6 Summary

The data reduction pipeline for the blue channel works fully automatically and stably. To control the reduction flow, log files are created during the reduction. In case of an error in some positions in the reduction flow, a message is written to a file. Using the error and log files the astronomer can check the reduction flow.
It is also possible that the astronomer uses this pipeline manual and checks the results after the individual reduction steps.
The pipeline is implemented in IDL and therefore the astronomer can modify the pipeline and the sub-procedures very simply and quickly. Furthermore, the HEROS pipeline is very flexible and so it can be easily supported.
Although, the pipeline works automatically and is stable there are two main problems in the data reduction: One problem in the reduction pipeline is the identification of faint outliers in the science image. An outlier correction is implemented in the procedure *slit_func.pro* (Sect. 4.4.10.4). The accuracy of this correction depends on the size of the swath width. With the small swath width, which is used for the pipeline, the accuracy of the outlier correction is not very high. Furthermore, the continuum normalisation process of late type stars may have problems in finding the quasi-continuum segments of the spectrum.
A future task will be the development of a data reduction pipeline for the red channel. In general, this pipeline will have the same structure as the pipeline for the blue channel.
Finally, the optimisation and regular support of the both pipelines is important to obtain the best possible outputs.

Chapter 5

Air pressure, temperature and humidity dependence of the wavelength solution

Dependences of the wavelength solution on air pressure and air temperature were observed for the UVES (UV-Visual Echelle Spectrograph) (Dekker et al. 2000) and HARPS (High-Accuracy Radial velocity Planetary Searcher) (Mayor et al. 2003) spectrograph. The UVES spectrograph is not pressurised or temperature-stabilised and Dekker found a line shift of 84 m/sec/hPa and -219 m/sec/K (Dekker et al. 2000). They conclude, that the variations in the line position are caused by variations of the refractive index of air inside the instrument. Mayor observed a line shift of 100 m/s per mbar for HARPS, if HARPS does not operate in vacuum (Mayor et al. 2003). A dependence between the wavelength solution dependent on the air pressure was also found for the STELLA I spectrograph (private communication Granzer).

To check the air pressure and air temperature stability of the wavelength solution at the HEROS spectrograph, I used 121 ThAr spectra.

5.1 Results

I estimated the pixel shift between the spectra of each order with a reference ThAr spectrum using a cross correlation. The reference ThAr spectrum is used for the automatic wavelength calibration.

I found, that the pixel shift is correlated with the air pressure, the air temperature and also the humidity. The average multiple linear correlation coefficient is 0.7987 ± 0.0004. In the following, the individual correlations of the air pressure, the air temperature and humidity are investigated.

In Fig. 5.1-5.3, the pixel shift of the relative order 6 vs. air pressure, air temperature and humidity is shown for example. The solid line in the Fig. 5.1-5.3 is a linear fit to estimate the slope. One sees in all three plots a correlation between the shift and air pressure, air temperature and humidity. To check the significance of these correlations, the t-Student test is used. With this test, the independence between two samples is tested. From the correlation coefficient r and the number of degrees of freedom, equal to n-2, where is n the
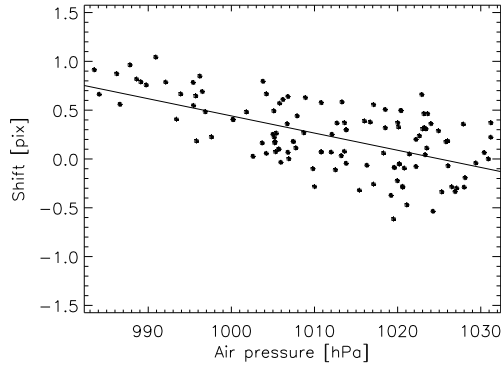
Figure 5.1: The pixel shifts of the relative order 6 vs. the air pressure.
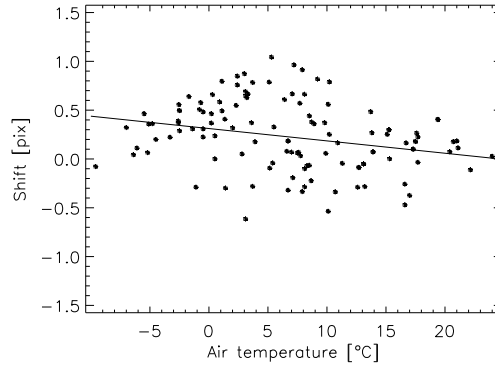
Figure 5.2: The pixel shifts of the relative order 6 vs. the air temperature.
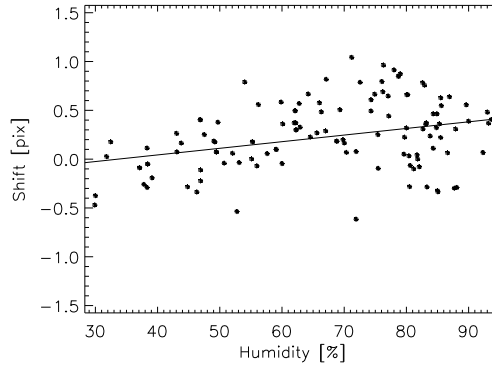
Figure 5.3: The pixel shifts of the relative order 6 vs. the humidity.

number of measurements, the t value Eq. 5.1 (Bronstein et al. 2001) can be estimated.

$$t = \frac{r\sqrt{n-2}}{\sqrt{1-r^2}} \tag{5.1}$$

The value of t_{cutoff}, for which one can consider a significant correlation between the pixel shift and air pressure, air temperature and humidity is ≥ 3.38 for a significance level $\geq 99.9\%$ (Bronstein et al. 2001). The average correlation coefficient r and average t-Student value are given in Table 5.1. The average t values show that the significance level

	|r|	| t |
Air pressure	0.592±0.001	8.01±0.02
Air temperature	0.304±0.002	3.48±0.02
Humidity	0.360±0.001	4.21±0.01

Table 5.1: The average correlation coefficient r and average t-Student value

for a correlation between the pixel shift and air pressure, air temperature and humidity is higher than 99.9%. The average slopes are given in Table 5.2. In the column 2 of Table

	<b [Δpix]>	<b [m/sec]>
Air pressure	-0.0168±0.0001 [Δpix/hPa]	-67.5±0.4 [m/sec/hPa]
Air temperature	-0.0135±0.0002 [Δpix/°C]	-54.2±0.8 [m/sec/°C]
Humidity	0.0070±0.0001 [Δpix/%]	28.1±0.4 [m/sec/%]

Table 5.2: The average slope in [Δpix] and [m/sec]

5.2, the slope is shown in pixel shift and in column 3 the shift is converted to a velocity shift, with a $\Delta\lambda$ of 0.067 Å per pixel at 5000 Å. The individual offsets and the slopes of each order are shown in the Fig. 5.7-5.12. Additionally, I checked the correlation between the air pressure, air temperature and humidity.
A correlation between air pressure and air temperature is shown in Fig. 5.4. On the other hand, the air pressure is not correlated with the humidity, see Fig. 5.5. Finally, the air
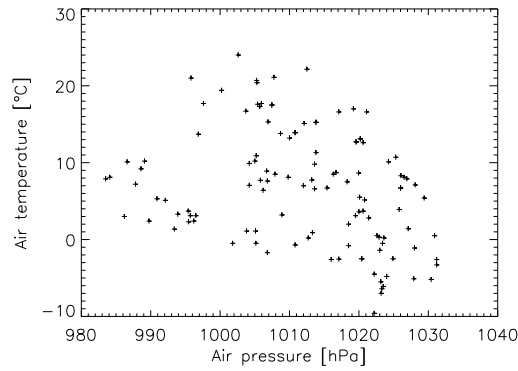

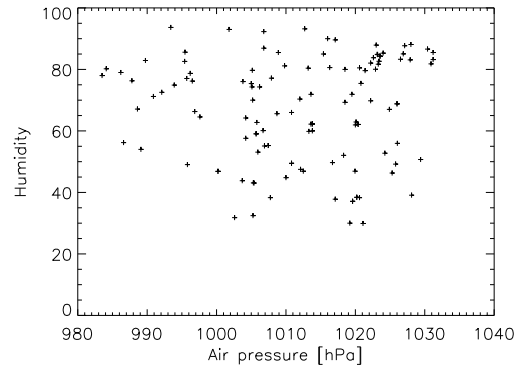Figure 5.4: Air pressure vs. air temperature
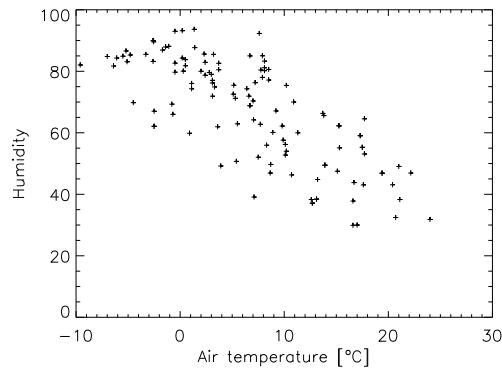

Figure 5.5: Air pressure vs. humidity

Figure 5.6: Air temperature vs. humidity

temperature vs. humidity is shown in Fig. 5.6. Here clearly exists a correlation. In Table 5.3, the correlations values r and t-value are given. The correlation is a strongest between humidity and air temperature and on the other hand the humidity and air pressure

	Air pressure r | |t|	Air Temperature r | |t|	Humidity r | |t|
Air pressure	1.0		
Air temperature	-0.33 | 3.8	1.0	
Humidity	0.02 | 0.2	-0.75 | 12.6	1.0

Table 5.3: The correlation coefficient

are not correlated. The air temperature and air pressure are correlated slightly. These result were not unexpected, see Fig. 5.4-5.6. Next, the dependence of the air pressures, air temperatures and humidities for each order are investigated. Therefore, the offsets and slopes of the linear fits between the shifts and air pressures, air temperatures and humidities for each order are plotted and the trends are calculated, see Fig. 5.7-5.12. The slopes of these trends are given in Table 5.4.

	Slope
Offset of the shift air pressure trend	$(1.3\pm8.0)\cdot10^{-3}$
Slope of the shift air pressure trend	$(-1.7\pm7.8)\cdot10^{-6}$
Offset of the shift air temperature trend	$(0.1\pm2.5)\cdot10^{-4}$
Slope of the shift air temperature trend	$(-3.9\pm0.9)\cdot10^{-5}$
Offset of the shift humidity trend	$(-1.9\pm0.3)\cdot10^{-3}$
Slope of the shift humidity trend	$(2.4\pm0.5)\cdot10^{-5}$

Table 5.4: The slope of the offset and slope trends in the Fig. (5.7-5.12)

The offset and slope of the relation between pixel shift and air pressure are constant because the slope of these trends is consistent with 0. Furthermore, the slope in the offset of the pixel shift air temperature relation is constant. The slopes of the air temperature shift, humidity shift and humidity shift are not constant.
That implies, that the pixel shift according to air temperature and humidity also depends on the position on the CCD and so on the order.

5.2   Correction of these effects

To consider the dependence of the pixel shift on the air pressure, air temperature and humidity, a correction functions for each order are created. The function is a linear combination of the difference of the air pressure (ap), air temperature (t) and humidity (h) to the reference ThAr spectrum. The order of the components is selected as given by the correlation between the shift and parameters. Furthermore, the correlation of the parameter to each other was a criterion. The correction function is defined:

$$pix\_shift \quad = \quad a\Delta ap + b\Delta t + c\Delta h \tag{5.2}$$
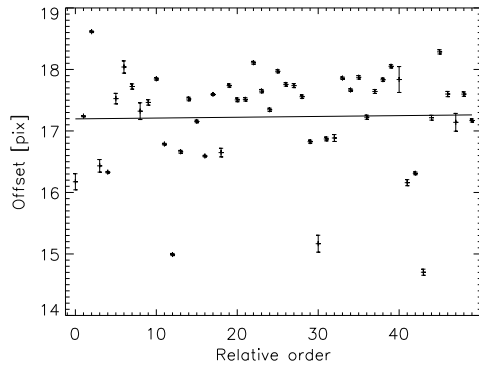
Figure 5.7: The offset of the relation air pressure vs. relative order
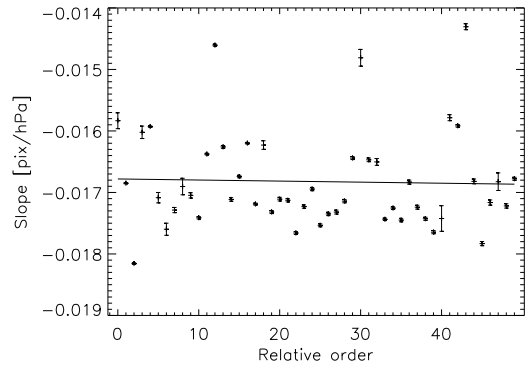
Figure 5.8: The slope of the relation air pressure vs. relative order
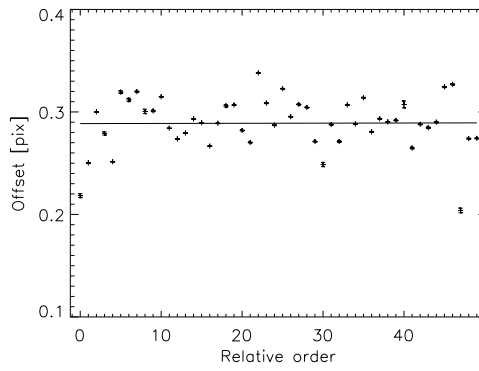
Figure 5.9: The offset of the relation air air temperature vs. relative order
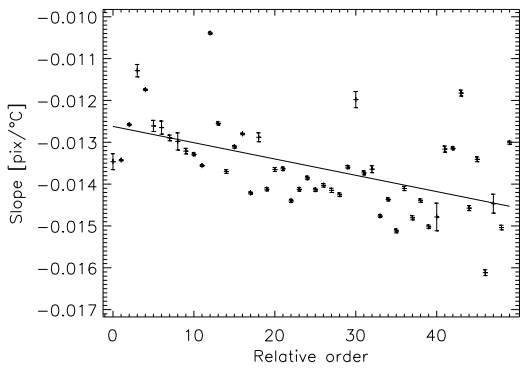
Figure 5.10: The slope of the relation air air temperature vs. relative order
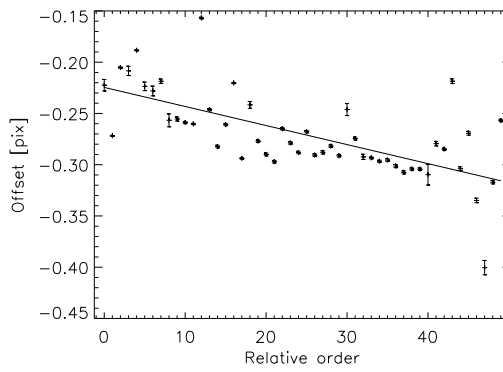
Figure 5.11: The offset of the relation humidity vs. relative order
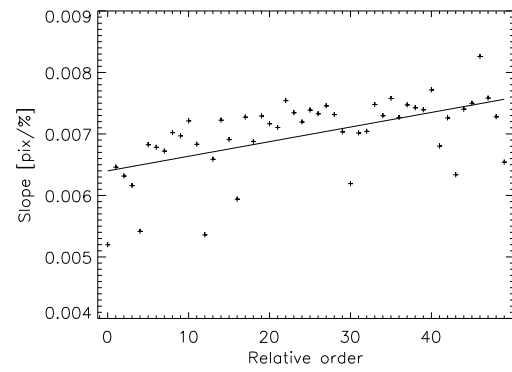
Figure 5.12: The slope of the relation humidity vs. relative order
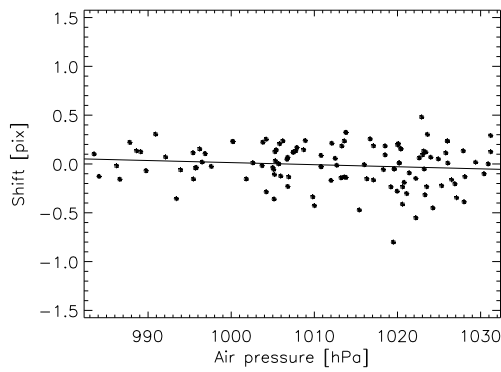
Figure 5.13: The pixel shifts of the relative order 6 vs. air pressure after the shift correction
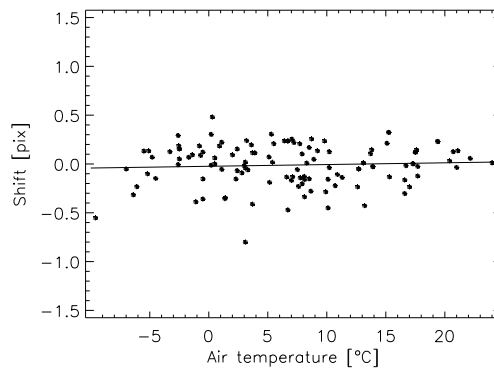
Figure 5.14: The pixel shifts of the relative order 6 vs. air temperature after the shift correction
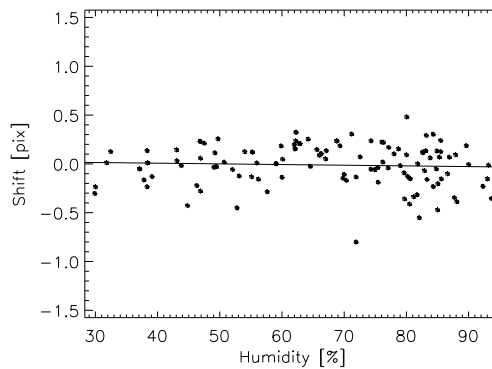
Figure 5.15: The pixel shifts of the relative order 6 vs. humidity after the shift correction

The parameters of this correction function are estimated with a linear least-squares minimisation. The parameters are given in Table A.2.

In Fig. 5.13-5.15, the pixel shift for the relative order 6 vs. the air pressure, air temperature and humidity after the air pressure, air temperature and humidity after the correction are shown. One can see, that strong the air pressure, air temperature and humidity trends are eliminated. To check whether a remaining trend exist, the trends in the corrected pixel shifts are calculated. The average slopes b are given in Table 5.5. These slopes are about 90% smaller, then the slopes without these correction. A complete elimination of the dependences was not expected because it is a three-dimensional parameter space. Furthermore, I performed a principal component analysis (PCA). With this analysis, one obtains the relative contribution of the individual parameters to the total variance in the data. The percentage provides information about the influence and the significance of the individual components. In Table 5.6, the percents of the data variance for the individual components are given. The percentage of variance in the data is only 3% for the humidity.
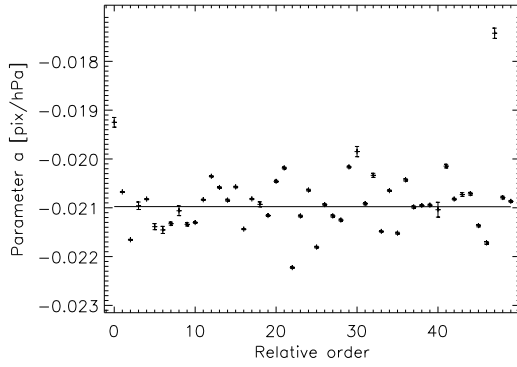
Figure 5.16: The parameter a of the correction equation Eq. (5.2) vs. relative order
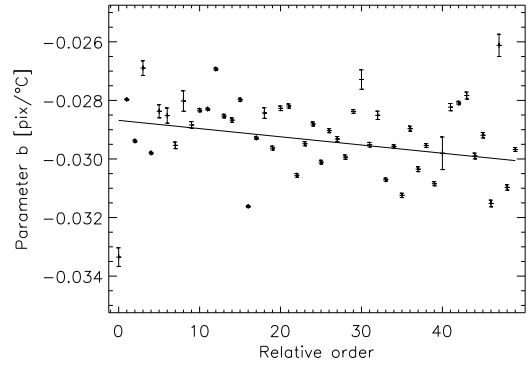
Figure 5.17: The parameter b of the correction equation Eq. (5.2) vs. relative order
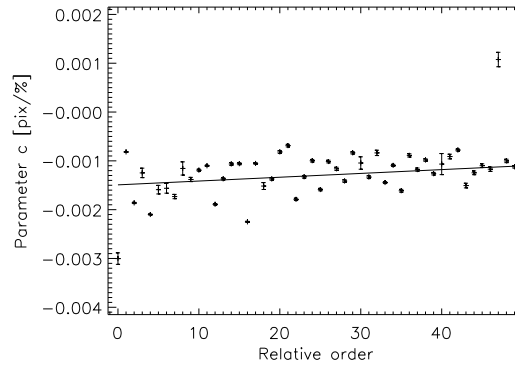
Figure 5.18: The parameter c of the correction equation Eq. (5.2) vs. relative order

	<b [Δpix]>	<b [m/sec]>
Air pressure	-0.00266±0.00008	-10.7±0.3
Air Temperature	0.0019±0.0001	7.6±0.4
Humidity	-0.00084±0.00005	-3.4±0.2

Table 5.5: The average slope of the trends in the residuals in [Δpix] and [m/sec]

Although, the influence of the humidity is small, it is nevertheless considered to obtain an accurately correction.

Next, I check the equation parameters of the correction equation (Eq. 5.2) for each order whether the equation parameters are constant dependent on the order number. In Fig 5.16-5.18, the individual parameter vs. relative order and a linear fit to check the trend of the parameter are shown. The slopes are given in Table 5.7. The parameters b and c of

Component	Percent of variance
Air pressure	66.37
Air temperature	30.34
Humidity	3.30

Table 5.6: The individual component with the percentage of the variance in the data

Parameter	Slope
a	$(-0.6\pm1.9)\cdot10^{-7}$
b	$(-2.8\pm0.06)\cdot10^{-5}$
c	$(7.8\pm0.2)\cdot10^{-6}$

Table 5.7: Slopes of the trends in the parameters of the correction equation Eq. 5.2

the correction equation Eq. 5.2 show trends dependent on the relative order. Thus, the parameters depend on the order location on the CCD. Finally, this correction is tested. The first step of the correction is the determination of the individual and average shifts ($\langle sh \rangle$) of each spectral order of the calibration ThAr spectra to a reference ThAr spectra. In the individual shifts, the air pressure, air temperature and humidity dependences are considered. The scientific spectra were taken at different air pressure, air temperature and humidity compared to the ThAr spectra. These difference are calculated. The pixel shifts caused by the air pressure, air temperature and humidity are determined using Eq. 5.2 and added to the average pixel shifts of the ThAr spectra. With these calculated new shifts of each order, the wavelength corresponding to each pixel is calculated (Sect. 4.4.13) for the scientific spectrum. The wavelengths of the scientific spectrum are also corrected by the barycentric and the radial velocity shift. The radial velocity shift is from the Simbad catalogue. To demonstrate the effect of the air pressure, air temperature and humidity correction, the velocity shifts for four spectral lines with and without correction are calculated. Therefore, the line cores are fitted with a Gaussian and subtracted from

Laboratory wavelength [Å]	shift_corr [m/s]	shift [m/s]	$\Delta shift$ [m/s]
4043.894	624.25±384.19	465.97±384.57	-158.28
4861.33	-61.30±454.88	-200.93±486.28	139.63
5049.796	-496.48±123.42	-555.57±103.74	59.09
5208.44	-301.31±491.38	-364.98±499.88	63.67

Table 5.8: The velocity shifts with and without air pressure, air temperature and humidity correction and the differences of the shifts

the laboratory wavelength. The results are given in Table 5.8. The average velocity shift with and without the correction are (-58.7 ± 244.4) m/s and (-163.9 ± 222.1) m/s, respectively. These values show an improvement of the deviation from the laboratory wavelength if one use the air pressure, air temperature and humidity correction. However, the errors of the average shifts are greater then the average velocity shift. The improvement is also inside of the error. These large errors are caused by the a relative strong scattering of the individual velocity shifts. This is an evidence that the accuracy of the wavelength solution

in each order is strong varied. Next, the individual shifts are compared.

For the shift comparison at the same wavelength, the errors of the shifts can be ignored because the errors of the velocity shifts are caused by the fit and the fit conditions are equal for the same wavelength. This is also the reason why the errors are not very different for the same wavelength.

If one compares the individual results at the same wavelength, one sees that at three wavelengths, the absolute values of the velocity shifts with the correction are smaller then without the correction. Only at one wavelength, the shift is greater then with a correction.

5.3   Conclusion

It was possible to show that the pixel shift depends on the air pressure, air temperature and humidity. To optimise the wavelength solution, a correction for these effects has to be performed. Therefore, a correction equation was created to eliminate the influence of the air pressure, air temperature and humidity. The demonstration of this correction shows that this correction works with a small improvement. The test shows also a relatively high scattering in the velocity shifts. At first, this effect should be investigated in a future wavelength solution because this has a stronger influence on the accuracy and the error of the mean radial velocity shift.

This pixel shift correction is not implemented in the current version of the data reduction pipeline. This correction will be implemented in the reduction pipeline after the camera upgrade of the spectrograph.

Chapter 6

The S index and the flux in the Ca II H+K lines

With the HRT, active stars will be observed. For the activity research, the Ca II H+K lines are the most important spectral lines in the optical spectral range because these lines are the most activity sensitive lines. In the Fig. 6.1, a lunar spectrum and of HD131156A are shown as an example for the influence of activity on the line profile. The Sun was in
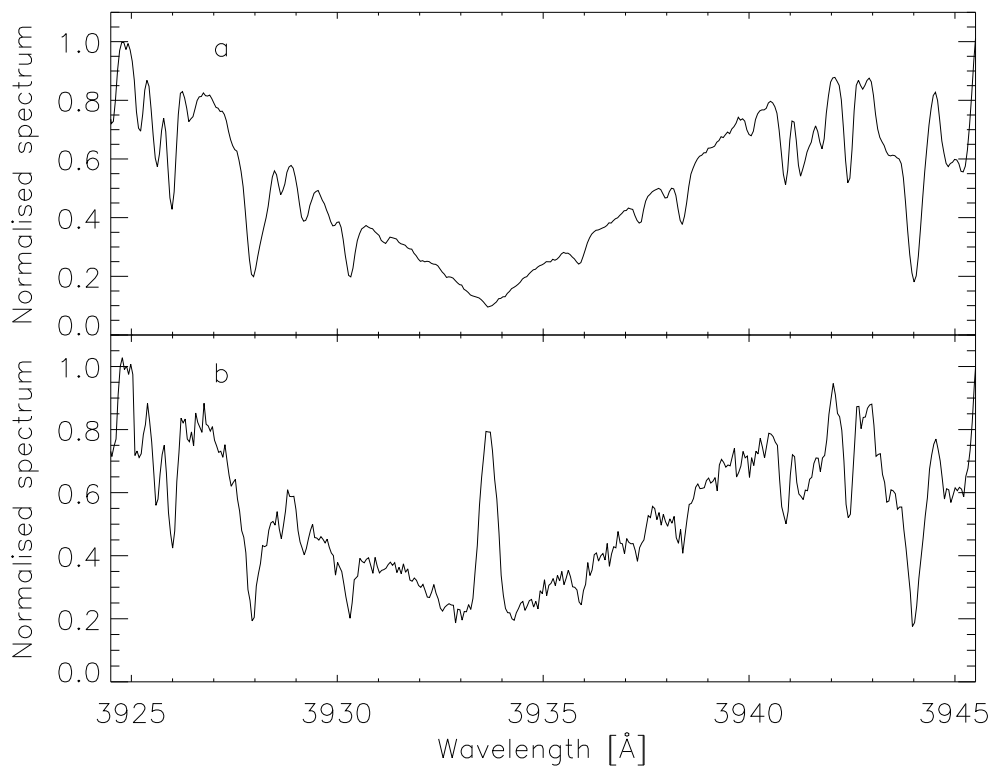
Figure 6.1: The Ca II K line a: of the Moon observed at Mar. 8 2009 b: of HD131156A observed at Mar. 20 2009

an activity minimum and the spectrum does not shown an emission peak in the Ca II K line core in contrast to the active star HD131156A.

To measure the activity level of a star, the Mount Wilson S-index is used. This chapter includes a general introduction about the S-index. Furthermore, the creation of a transformation equation from the S-index of the HRT to Mount Wilson S-index is presented. Finally, a conversion factor from the relative to the absolute surface flux is determined.

6.1 Definition and measurement of the Mount Wilson S-index

The Mount Wilson S-index (hereafter S_{MWO}) is the most important standard activity index in the optical spectral range, since Wilson began a long-term monitoring program of main sequence stars "Mount Wilson HK-Project" at the Mount Wilson observatory (MWO) in 1966 (Wilson 1978). This long-term program searched for chromospheric variations in main-sequence stars like the 11 year solar cycle (Wilson 1978; Vaughan et al. 1981; Duncan et al. 1991; Baliunas et al. 1995). A lot of our knowledge about the chromospheric activity is based on the results of this program.

The first detector of the "Mount Wilson HK-Project" was the HKP-1, a two-channel photometer at the Coudé focus of the 2.5m (100 inch) telescope on the Mount Wilson. One channel was centred in the line centre of the Ca II H+K line (3968.47 Å and 3933.66Å, respectively), with a width of 1 Å. The other channel had two bandpasses of 25 Å width. These bandpasses have a distance of 250Å and were located symmetrically around the Ca II H+K lines. This instrument was operated until 1977 and then replaced by the HKP-2. The HKP-2 was a four-channel photon-counting spectrophotometer at the Cassegrain focus of the 1.5m (60 inch) telescope. The S_{MWO} is a composition of these four channels and is defined as (Vaughan et al. 1978):

$$S_{MWO} \quad = \quad \alpha \left(\frac{N_H + N_K}{N_R + N_V} \right) \qquad (6.1)$$

This index is the ratio of the number of counts N_H and N_K in the triangular bandpasses H and K with a FWHM of 1.09 Å centre in the Ca II H+K line cores and the number of counts N_R and N_V in the 20 Å continuum bandpasses R and V centred at 3901.07 Å and 4001.07 Å, respectively, after a time normalisation and a sky correction. The reason to use a triangular bandpass was the instrumental profile of the HKP-2 in the H and K channel. The factor α is a calibration factor to be able to compare the values of HKP1 and HKP2 determined for each night. Duncan adopted the factor α as a constant with α=2.4, because the night to night variations of α were less than the precision of the S index (Duncan et al. 1991). The S index is thus a dimensionless quantity which allows to estimate the activity level of a star. It depends on the colour index of the object.

The S index shows short- and long-term variations (Vaughan et al. 1981). The short-time variations are caused by the rotational modulation of the Ca II H+K flux of the star (Stimets and Giles 1980; Vaughan et al. 1981). Another reason for the short-time variations is a possible star-planet interaction (SPI) (Shkolnik et al. 2003). The long-term variations come from an activity cycle of the object (Wilson 1978; Vaughan et al. 1981; Baliunas et al. 1995). In 1991 Duncan published a catalogue of 1296 stars with the average S_{MWO} measured from 1966 to 1983 (Duncan et al. 1991).

A new long-term monitoring program was started 1994 at the Lowell Observatory with the Solar-Stellar Spectrograph (SSS) (Hall et al. 2007). This program is practically the successor of the "Mount Wilson HK-Project".

These are further examples for surveys to determine the S-index:, Henry et al. (1996), Gray et al. (2003) and Wright et al. (2004). The survey performed by Henry et al. (1996) observed more than 800 stars on the southern hemisphere and measured the S_{MWO} and the $\log R'_{\mathrm{HK}}$ (Sect. 7.1). Furthermore, Henry et al. (1996) created a definition for the activity state of a star from very inactive to very active (Sect. 8.1). The surveys performed by Gray et al. (2003) and by Wright et al. (2004) observed stars on the northern hemisphere. The survey by Gray et al. (2003) ("NEARBY STARS (NSTARS) PROJECT") collected the spectra of the objects, basic stellar parameter, the estimated S_{MWO} and the activity state of stars in a online database[1]. Wright et al. (2004) estimated the S_{MWO} of ≈ 1200 main-sequence stars and calculated the $\log R'_{\mathrm{HK}}$ and the age of the star.

The S-indices of these surveys were determined from the observed stellar spectrum. The method was introduced by Duncan et al. (1991). At this, the areas in the spectrum of the corresponding bandpasses are determined. These values are used to calculate the S-index. The constant α depends on the instrument, thus α is different for each survey. Finally, a transformation equation to convert the instrumental S-index to S_{MWO} was created.

6.2 Conversion S_{MWO} to the flux of the Ca II H+K lines

With the S-index, one does not have information about the flux in the Ca II H+K lines. Furthermore, the S-index depends on the colour index of the object. Therefore, it is not possible to use the S-index for the comparison of the activity state of two objects with different colour index. Hence, it was necessary to find a possibility for the comparison of the activity states of objects with different colour index.

This possibility was found by Middelkoop (1982). Middelkoop (1982) derived a correction factor to eliminate the colour dependence of the S-index and created the equation to calculate the relative surface flux [au]. He performed these as follows (Middelkoop 1982): The counts in the four bandpasses of the S-index can be interpreted as the absolute flux in these bandpasses. The conversion factor to convert the counts into absolute flux can be ignored because only the flux ratio is used here. The S-index can be written as:

$$S_{\mathrm{MWO}} \;=\; \alpha \left(\frac{\mathcal{F}_{\mathrm{H}} + \mathcal{F}_{\mathrm{K}}}{\mathcal{F}_{\mathrm{R}} + \mathcal{F}_{\mathrm{V}}} \right). \tag{6.2}$$

Eq. 6.2 can be transposed so that one obtains the Ca II H+K flux. The flux is given as:

$$\mathcal{F}_{\mathrm{H}} + \mathcal{F}_{\mathrm{K}} \;=\; \alpha \, \frac{S_{\mathrm{MWO}}}{\alpha} \, (\mathcal{F}_{\mathrm{R}} + \mathcal{F}_{\mathrm{V}}), \tag{6.3}$$

where the flux in the two continua bandpasses is given as:

$$\mathcal{F}_{\mathrm{R}} + \mathcal{F}_{\mathrm{V}} \;=\; \beta \, (N_{\mathrm{R}} + N_{\mathrm{V}}) \, \frac{F_{BOL}}{f_{BOL}}. \tag{6.4}$$

The counts in the two continua bandpasses ($N_{\mathrm{R}} + N_{\mathrm{V}}$), the absolute bolometric flux (F_{BOL}) and apparent flux (f_{BOL}) of the star and a unknown constant (β) are used to obtain the

---

[1]http://stellar.phys.appstate.edu/

flux in the two continua bandpasses. The absolute bolometric flux of a star is defined as:

$$F_{BOL} = \sigma \, T_{eff}^4, \tag{6.5}$$

where σ is the Stefan Boltzmann constant and T_{eff} the effective temperature of the star. The apparent flux (f_{BOL}) of the star is given as:

$$f_{BOL} = \gamma \, 10^{-0.4(m_v+BC)}, \tag{6.6}$$

where, γ is a unknown constant, m_v the apparent visual magnitude and BC the bolometric correction. If one inserts Eq. 6.4, 6.5 and 6.6 in Eq. 6.3 and transposes the equation, one obtains:

$$\mathcal{F}_H + \mathcal{F}_K \frac{\alpha\gamma}{\beta\sigma} = (N_R + N_V) \, 10^{0.4(m_v+BC)} \, S_{MWO} \, T_{eff}^4 = F_{H+K}. \tag{6.7}$$

The bandpass counts and the factor $10^{0.4(m_v+BC)}$ are combined to the C_{cf} factor. This is given as:

$$C_{cf} = (N_R + N_V) \, 10^{0.4(m_v+BC)} \tag{6.8}$$

This factor corrects for the colour dependence of the S-index. The equation to calculate the relative surface flux [au] in the Ca II H+K lines is given as:

$$F_{H+K} = C_{cf} \, S_{MWO} \, T_{eff}^4 \tag{6.9}$$

Middelkoop (1982) created a relation of $\log C_{cf}$ depending on the colour index $B-V$ for the $B-V$ range $0.45 \leq B-V \leq 1.5$. The relation of $\log C_{cf}$ was modified by Noyes et al. (1984). In 1984, Rutten found that the correction factor C_{cf} depends on the luminosity class and created two new equations (for main-sequence stars and giant stars) to calculate the correction factor C_{cf} (Rutten 1984). Also he expanded the definition range, see Eq. 6.10 & 6.11. The relations for the main sequence stars are displayed vs. B-V in Fig 6.2. A difference between the relations of Rutten (1984), Middelkoop (1982) and Noyes et al. (1984) can be found at the definition border $0.45 \leq B-V \leq 0.6$ and $1.35 \leq B-V \leq 1.5$, respectively. To calculate the relative surface flux the correction factor C_{cf} by Rutten (1984) is used in this work. These equations are:
for main-sequence star ($0.3 \leq B-V \leq 1.6$):

$$\log(C_{cf}) = 0.25(B-V)^3 - 1.33(B-V)^2 + 0.43(B-V) + 0.24 \tag{6.10}$$

for subgiants and giants star ($0.3 \leq B-V \leq 1.7$):

$$\log(C_{cf}) = -0.066(B-V)^3 - 0.25(B-V)^2 - 0.49(B-V) + 0.45 \tag{6.11}$$

Rutten (1984) added the scaling factor 10^{-14} to the Eq. 6.9. This factor was obtained at the creation of the correction factor C_{cf} by Rutten (1984). The equation to calculate the relative surface flux in the Ca II H+K lines is (Rutten 1984):

$$F_{H+K} = C_{cf} \, S_{MWO} \, T_{eff}^4 \, 10^{-14} \tag{6.12}$$

In this work, the effective temperature is calculated with the relation between $\log T_{eff}$ and B-V ($0.0 \leq$ B-V ≤ 1.5) (Gray 2005):

$$\log T_{eff} = 3.981 - 0.4728(B-V) + 0.2434(B-V)^2 - 0.0620(B-V)^3 \tag{6.13}$$

The relative surface flux [au] can be converted to the absolute surface flux [erg cm^{-2} s^{-1}] with the relation (Middelkoop 1982; Rutten 1984; Hall et al. 2007):

$$\mathcal{F}_{H+K} = K \, F_{H+K} = K \, C_{cf} \, S_{MWO} \, T_{eff}^4 \, 10^{-14} \tag{6.14}$$
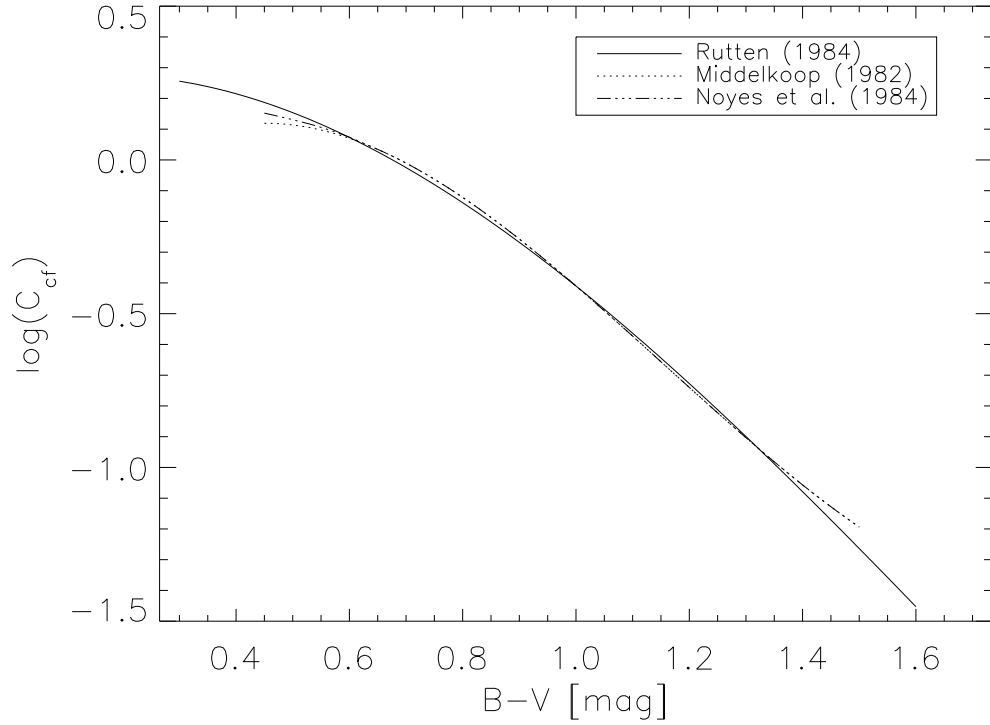
Figure 6.2: The different relations of the correction factor $C_{\rm cf}$

6.3 Formation of the Ca II H+K lines

The Ca II is singly ionised calcium and the Ca II H+K lines are Fraunhofer lines. These lines are formed by the electron transition (Shine et al. 1975):
for the Ca II K line

$$4s^2 S_{1/2} \longleftrightarrow 4p^2 P_{3/2}$$

for the Ca II H line

$$4s^2 S_{1/2} \longleftrightarrow 4p^2 P_{1/2}$$

In the absorption case, the last bound electron will be raised to a higher energy level from $S_{1/2}$ level to the $P_{1/2}$ level and $P_{3/2}$ level for the H line und K line, respectively. In the emission case, the electron transferred from the $P_{1/2}$ level and $P_{3/2}$ level for the H line und K line, respectively to the $S_{1/2}$ level. The notation to describe the energy level of an atom is (Haken and Wolf 2004):

$$n^{2S+1}L_j$$

Here n is the main quantum number of the highest excited-state electron, $2S+1$ the multiplicity, L the orbital angular momentum and j the quantum number of the total angular momentum of the atom. The orbital angular momentum $L = 0, 1, 2, 3, 4, ...$ is defined as
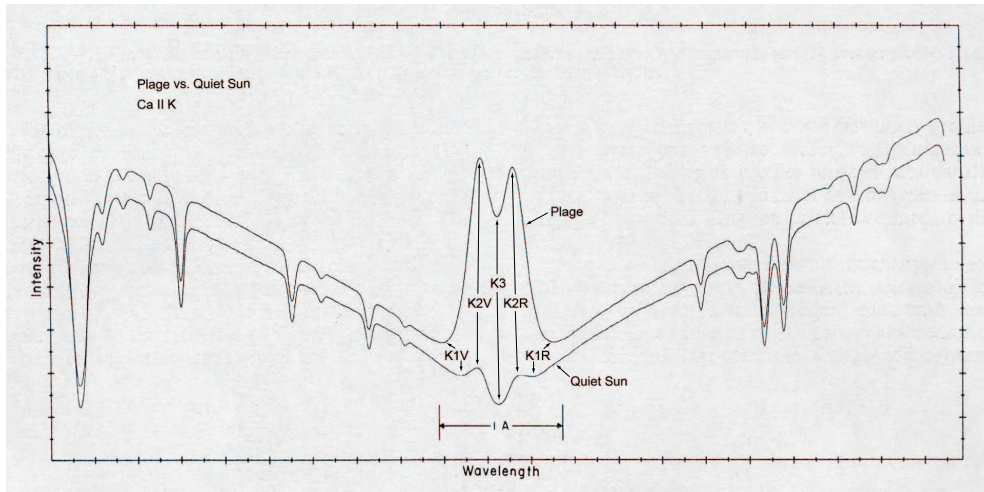
Figure 6.3: The average Ca II K line profiles for a quiet and an active Sun region centred at 3933.682 Å (White and Livingston 1981, modified by Mittag).

S, P, D, F, G, ...

Ca II H+K absorption lines are formed in the photosphere whereas a emission of Ca II H+K lines is generated through the magnetic activity in the chromosphere (Montes et al. 2000). Here, only the formation of the Ca II K line is described briefly because the structure and formation of the Ca II H line is similar to the Ca II K line.

Fig. 6.3 shows the Ca II K line of a quiet and an active Sun region (White and Livingston 1981, modified by Mittag). The upper curve shows the average line profile of the Ca II K line of an active Sun region. A strong emission core in the line centre can be seen. In the lower cure, the average line profile of the Ca II K line of a quiet Sun region is shown. Here, no strong emission core is present. Only a double peak structure can be seen.

The Ca II K line has three marked points in the lines, see Fig 6.3. For the K line, these points are called K1, K2 and K3. In Fig. 6.4, the temperature structure of the photosphere and chromosphere is shown for the averaged quiet Sun (Vernazza et al. 1981). Furthermore, the formation regions of the Ca II K line are shown. The line profile of the Ca II K line is formed in different chromospheric layers. The line at K1 is formed in the temperature minimum of the stellar atmosphere. In this region, the transition from the photoshere to the chromosphere is located. The emission core (plage) of the line, which is labelled with K2, is formed in the middle of the chromosphere and is created by collisions. The temperature range is approximately 5000 K to 6200 K (Fig. 6.4). This temperature range corresponds to an atmospheric level range of approximate 700 km to 1400 km. In the upper chromosphere, the line at the K3 is created. The region has an atmospheric level range of approximate 1800 km to 2000 km and corresponds to a temperature range of approximate 6500 K to 7000 K. In this region, a re-absorption creates the characteristic double peak in the Ca II K line.

The line profile depends on different broadening mechanism (Gray 2005). The main broadening mechanisms are the natural line broadening, pressure broadening and thermal broadening. The natural line broadening is caused by electron transitions. The pressure broadening is generated by the collisional interaction between the atoms and particles.
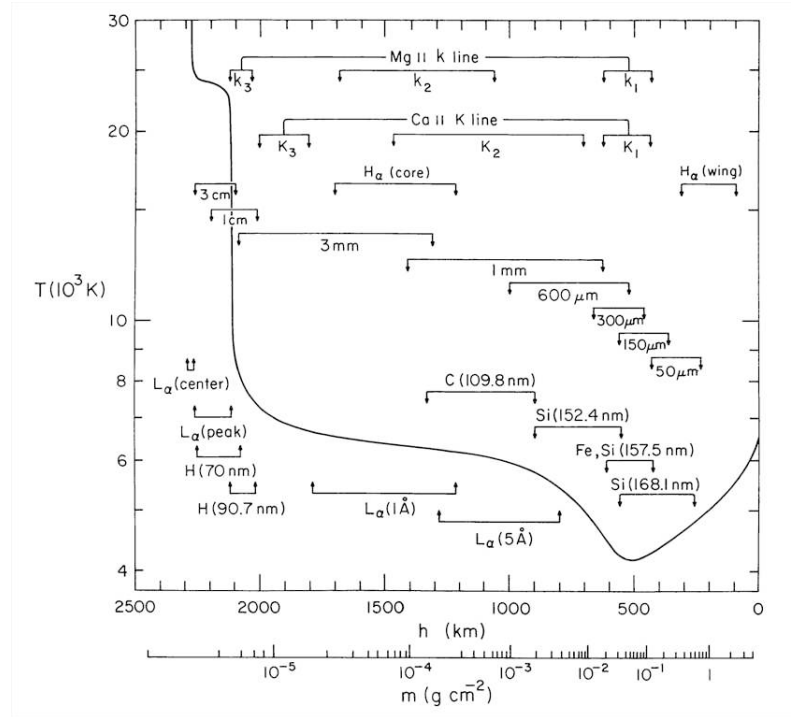
Figure 6.4: The temperature structure of the photosphere and chromosphere for the average quiet Sun with the locations of the line formation regions for different spectral lines (Vernazza et al. 1981)

One distinguishes between Stark and Van-der-Wals broadening. In the case of the Stark broadening, the atoms have an impact on electrons, protons and ions. This broadening is found in hydrogen lines and spectral lines in hot stars. The interaction potential is $\sim 1/r^2$ for the linear or $\sim 1/r^4$ for the quadratic Stark broadening between the atoms and the perturbers. Van-der-Wals broadening is caused by an atom or a molecule having an impact with a neutral hydrogen atom and the interaction potential is $\sim 1/r^6$, with the distance r between the perturbers. The thermal broadening is caused by the motion of the atoms.

The dominant broadening mechanism for the Ca II H+K lines is the pressure broadening of Van-der-Wals type (Linsky 1968). Through this broadening, the Ca II H+K lines have strongly pressure-broadened line wings and are very prominent in a spectrum.

6.4 Determination of the S-index with HRT data

To compare the results of activity measurement of the HRT with the other results, it is essential to determine the S_{MWO}. Furthermore, it is very simply to calculate the Ca II H+K flux with the S_{MWO}. In this section, the calculation of the S_{HRT} and the conversion from S_{HRT} to S_{MWO} are represented.
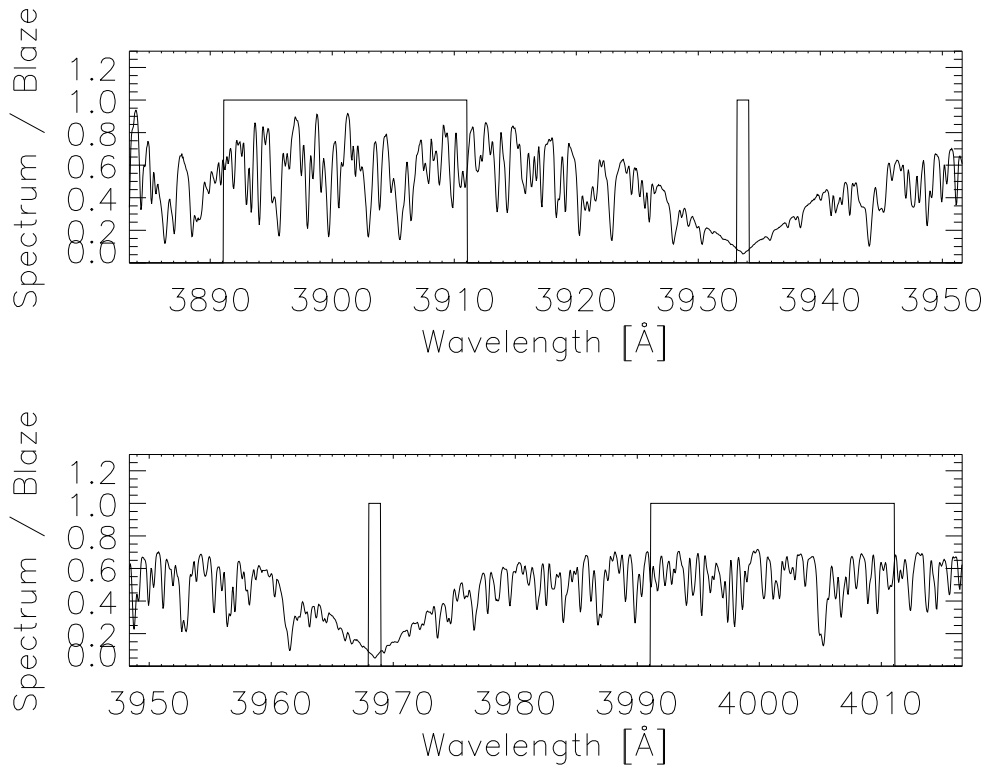
Figure 6.5: The Ca II H+K area of the sun observed at Mar. 8 2009 with the four bandpasses.

6.4.1 S_{HRT} calculation

To calculate S_{HRT}, the blaze-normalised and merged spectrum is used (Sect. 4.2.6.1). First, the radial velocity shift is estimated for the object in the Ca II H+K region (3900 Å to 4000 Å). Here the Ca II H+K region of the observed spectrum is compared to a synthetic spectrum calculated with PHOENIX (Ch. 7), via a cross correlation. To select the suitable synthetic spectrum, the absolute magnitude of the object is calculated with the Hipparcos distance. With the colour index B-V and the absolute magnitude, one obtains the position in the H-R diagram. The H-R diagram is divided in regions for main sequence stars, subgiants and giant stars. The average absolute magnitudes for main-sequence, subgiant and giant stars are defined in Allen (1976). After the estimation of the luminosity class for the object, the colour index B-V is compared to the B-V ranges of the synthetic spectra. The wavelength of the selected synthetic spectrum is converted from vacuum to air wavelengths and thereafter the spectral lines are broadened by the rotation velocity (vsini) and the instrumental broadening (R). With a cross correlation, the radial velocity shift is estimated. The wavelength of the observed spectrum is corrected by the estimated radial velocity shift.

To calculate S_{HRT}, the areas of the four bandpasses of the S-index are estimated in the blaze-normalised and merged spectrum, for which a 1 Å bandpass is used and not the classical triangular bandpass with a FWHM of 1.09 Å for the Ca II H+K lines. The reason

for using the 1 Å bandpass is that one does not have a triangular instrumental profile in the spectrum of the Ca II H+K lines. Fig. 6.5 shows the Ca II H+K area for the sun with the four bandpasses. Finally, the ratio of these four areas is calculated with Eq. 6.1. The factor α is set to 1, because this factor has only an influence on the slope and not on the constant and the precision of the transformation Eq. 6.20.

At present, it is not possible to use the signal to noise (S/N) in the line core as error for the S-index due to the high dark noise, see Sect. 4.2.2. Therefore, the error of S_{HRT} ($\sigma_{S_{\text{HRT}}}$) is estimated with the arithmetic mean of the S/N in the four bandpasses divided by the arithmetic mean of counts of the blaze in the corresponding bandpasses.

$$\sigma_i \;=\; \frac{\langle S/N \rangle_i}{\langle blaze \rangle_i} \tag{6.15}$$

The index i is the corresponding bandpass. Next, the errors for the line bandpasses and the continua bandpasses are calculated:

$$\sigma_{line} \;=\; \sqrt{\sigma_K^2 + \sigma_H^2} \tag{6.16}$$

$$\sigma_{cont} \;=\; \sqrt{\sigma_R^2 + \sigma_V^2} \tag{6.17}$$

Finally, the error ($\sigma_{S_{\text{HRT}}}$) is calculated:

$$\sigma_{S_{\text{HRT}}} \;=\; \sqrt{\left(\frac{1}{(N_{\text{R}} + N_{\text{V}})} \right)^2 \sigma_{line}^2 + \left(\frac{(N_{\text{H}} + N_{\text{K}})}{(N_{\text{R}} + N_{\text{V}})^2} \right)^2 \sigma_{cont}^2} \tag{6.18}$$

6.4.2 Conversion from S_{HRT} to S_{MWO}

The S-index from different instruments have to be converted to the Mount Wilson S-index in order to be comparable. Therefore, it is necessary to create a transformation equation from S_{HRT} to S_{MWO}. For the creation of this transformation equation, I selected mainly flat active and active variable stars. Therefore, I used two data sets. The first data set is the data from Baliunas et al. (1995) and the second data set the first results of long-term monitoring program with the SSS at the Lowell Observatory Hall et al. (2007). For the second data set, S_{MWO} were obtained via private communication with Hall. Hall sent the time series of the S-index so that it was possible to use the S-index of the object if the object was observed in the last year. If the object was not observed in the last year, the average S_{MWO} was used. Furthermore, for two objects, S_{MWO} was taken from Hall et al. (2009). For one object, the S-index was extrapolated from the period derived by Baliunas et al. (1995). The method how Hall obtains S_{MWO} is as follow:

The observed spectra of the Ca II H+K region are continuum normalised. Before the S-index is determined, the spectra are normalised again so that one obtains the true intensity ratio of the two bandpasses of the star. The method and the equations are described in Hall and Lockwood (1995) and on the homepage of the SSS project (http://www.lowell.edu/ users/jch/sss/article.php?r=t_dataanlyz_hkabs). The S-index is calculated from the areas of the four bandpasses of this spectrum. Hall uses a 1Å bandpass for the bandpass in the Ca II H+K line cores. Hall uses for the factor α in Eq. 6.1 the values 19.2 (Hall et al. 2007). Finally, he converts the S-index to the Mount Wilson S-index with a transformation equation (Hall and Lockwood 2004).

Object	S_{MWO}	Ref.	long-term variations	Ref.	HRT S_{MWO}	*prv*	nobs
HD6920	0.189	2	Var/HV	1/2	0.188±0.009	0.79	2
HD10307	0.155	2	LV	2	0.146±0.006	5.93	2
HD10476	0.183	2	P=9.6/LV	1/2	0.181±0.009	1.20	2
HD13421	0.131	1	FA/N	1/2	0.139±0.013	5.96	2
HD19373	0.149	2	N	2	0.144±0.005	3.32	2
HD22072	0.131	1	Var	1	0.147±0.008	12.26	1
HD32923	0.143	2	N	2	0.143±0.006	0.15	3
HD35296	0.318	2	Long/FA	1/2	0.307±0.008	3.37	1
HD39587	0.340	2	Var/FA	1/2	0.340±0.011	0.03	1
HD41330	0.143	2	FA	2	0.156±0.008	8.81	1
HD42807	0.352	2	FA	2	0.349±0.017	0.76	2
HD43587	0.156	1	FA?/SV	1/2	0.153±0.008	1.89	2
HD61421	0.171	1	Var	1	0.157±0.006	8.42	5
HD72905	0.367	1	Var	1	0.359±0.014	2.23	4
HD75332	0.279	1	Var/HV	1/2	0.279±0.012	0.11	5
HD75528	0.128	2	LV	2	0.138±0.006	7.72	1
HD79028	0.137	2	N	2	0.149±0.008	8.76	23
HD89744	0.137	1	FA	1	0.144±0.009	5.33	9
HD101501	0.316	3	Var/HV	1/2	0.341±0.016	7.94	8
HD114378	0.244	1	Long	1	0.229±0.008	6.14	4
HD115383	0.313	1	Var	1	0.309±0.026	1.33	5
HD120136	0.192	3	P=11.6/HV	1/2	0.184±0.008	4.14	20
HD121370	0.126	2	N	2	0.135±0.007	7.14	95
HD124570	0.134	2	FA/N	1/2	0.136±0.009	1.44	5
HD131156A	0.461	1	Var	1	0.436±0.015	5.35	4
HD137107	0.184	1	Var	1	0.176±0.008	4.09	3
HD142373	0.147	1	FA	1	0.147±0.012	0.28	50
HD201091	0.700	4	P=7.3/SV	1/2	0.716±0.035	2.28	9
HD217014	0.149	1	Var/N	1/2	0.147±0.008	1.40	6

Table 6.1: The objects used for the calibration from S_{HRT} to S_{MWO}, with the reference S_{MWO} and S_{MWO} measured with the HRT, the absolute value of the percentage of the relative variations *prv* and the number of observations (nobs)

Ref: [1] Baliunas et al. (1995), [2] S_{MWO} private communication Hall and long-term variations Hall et al. (2007), [3] Hall et al. (2009), [4] S_{MWO} extrapolated from the period of the activity cycle

Def: FA: (flat active stars) show no activity cycle, VAR: (variability active stars) shows a variability in the activity but not an activity cycle, P: (active stars) period of the activity cycle, N: $\Delta\mathcal{F}_{\mathrm{Ca}}$ is below the detection limit or the observed variability is within the errors zero, SV: (active stars) solar-activity variables, LV: (active stars) low-activity variables, HV: (active stars) high-activity variables
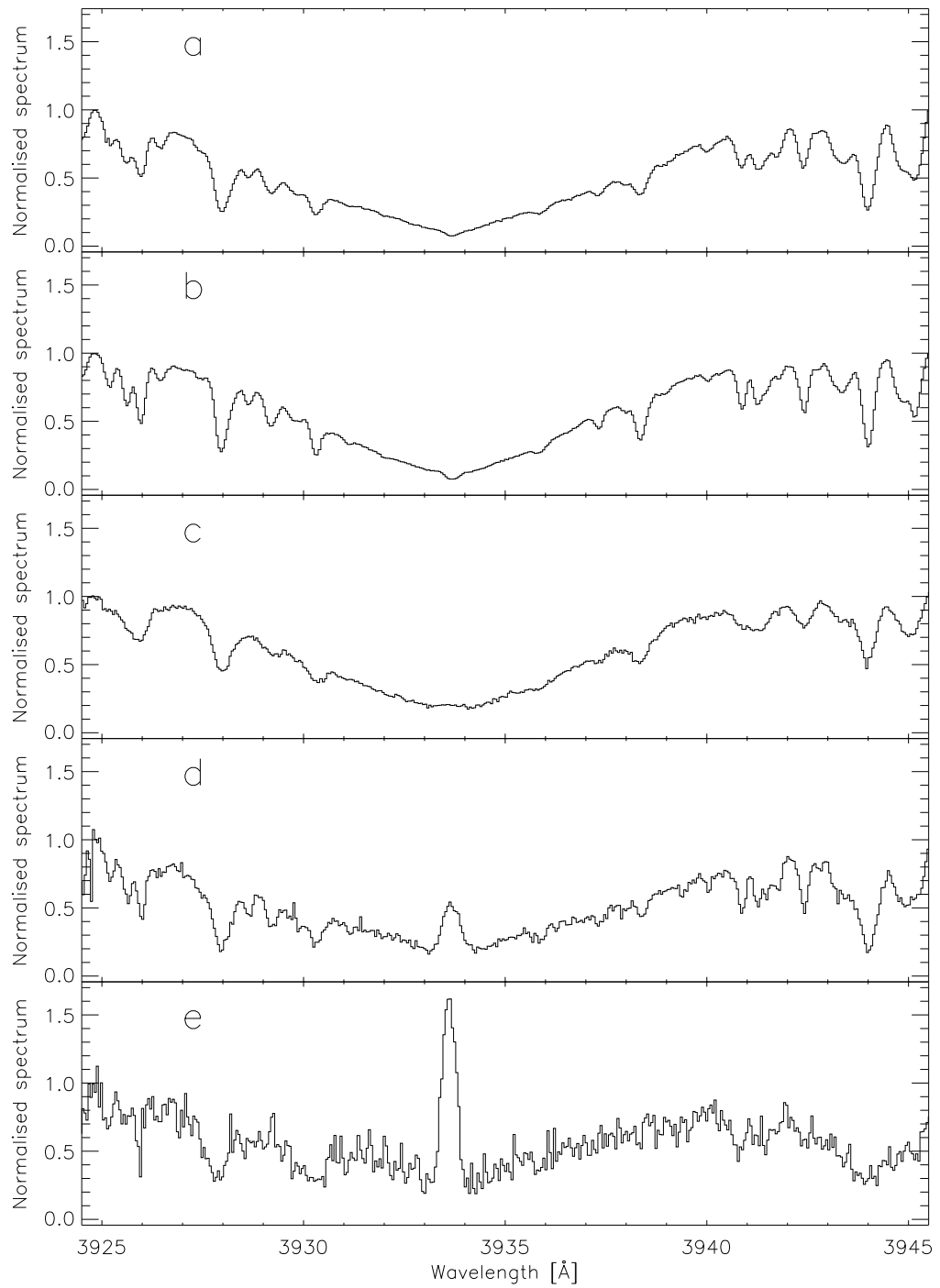
Figure 6.6: Examples of Ca II K lines from objects which were used to create the transformation equation and different activity level; a: HD121370, b: HD61421, c: HD114378, d: HD101501, e: HD201091
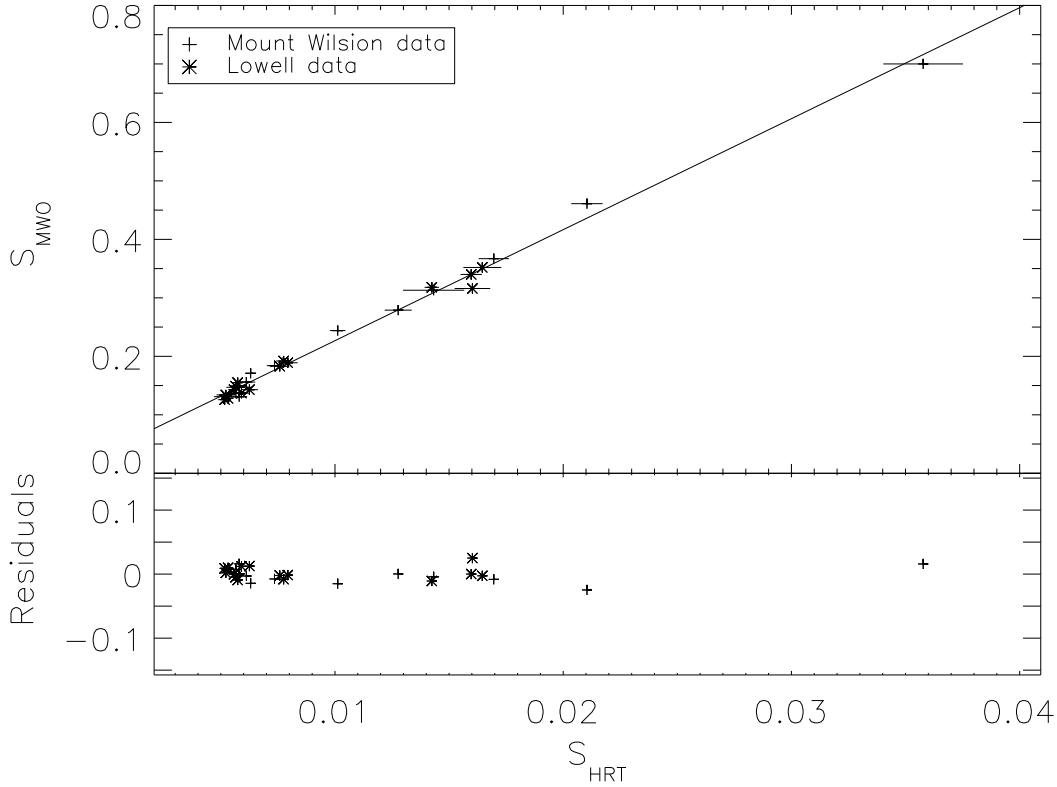
Figure 6.7: S_{MWO} vs. S_{HRT} and the residuals of the fit

The objects which were used to create a transformation equation from the S-index of the HRT to the Mount Wilson S-index are given in Table 6.1. Furthermore, S_{MWO} and the long-term variations are given in Table 6.1. In Fig. 6.6, the spectra of the Ca II K line of five objects are shown, which were used for the derivation of the transformation equation. The spectra are sorted by activity. In Fig. 6.6a, the lowest active star is shown whereas in Fig. 6.6e, the highest active star is shown. In this sequence, one can see the changing of the line profile with the increase of the activity level of the star. The transformation equation was created as follow:

The objects (Table 6.1) are observed with the HRT and the S_{HRT} is calculated, see Sect 6.4.1. If the object was observed several times, the arithmetic mean of the S_{HRT} and the corresponding error is calculated. This error is a composition of the error of the arithmetic mean of S_{HRT} (σ_1), the arithmetic mean of the error of the single measurement (σ_2) and the error of the arithmetic mean of the error of the single measurement (σ_3):

$$\sigma_{\langle S_{\mathrm{HRT}} \rangle} \quad = \quad \sqrt{\sigma_1^2 + \sigma_2^2 + \sigma_3^2}. \tag{6.19}$$

In the upper plot of Fig. 6.7, S_{MWO} vs. S_{HRT} is shown and the solid line represents the fit to convert S_{HRT} to S_{MWO}. The transformation equation is obtained as:

$$S_{\mathrm{MWO}} \quad = \quad (0.0369 \pm 0.0037) + (18.98 \pm 0.30)S_{\mathrm{HRT}} \tag{6.20}$$

K [erg cm^{-2} s^{-1}]	Reference	Flux bandpass
$0.76 \cdot 10^6$	Middelkoop (1982)	H1K1 (Linsky et al. 1979)
$1.21 \cdot 10^6$	Oranje (1983)	HKP2 bandpass
$1.29 \cdot 10^6$	Rutten (1984)	HKP2 bandpass
$1.52 \cdot 10^6$	Schrijver et al. (1989)	1 Å rectangle bandpass
$(0.80 \pm 0.15) \cdot 10^6$	Hall and Lockwood (1995); Hall et al. (2007)	1 Å rectangle bandpass
$(0.97 \pm 0.11) \cdot 10^6$	Hall et al. (2007)	1 Å rectangle bandpass

Table 6.2: The different conversion factors K from the relative surface flux to the absolute surface flux

The HRT S_{MWO} calculated with the transformation Eq. 6.20 are given in Table 6.1. In the lower plot of Fig. 6.7, the residuals of the fit are shown. The standard deviation of the residuals is:

$$\text{Standard deviation of the residuals} = 0.011$$

Furthermore, the absolute value of the percentage of the relative variations $|\,prv\,|$ between the reference S_{MWO} and the HRT S_{MWO} are computed with Eq. 6.21 and the individual results are given in Table 6.1.

$$prv \;\; = \;\; \left(\frac{|\,\mathrm{HRT}\ S_{\mathrm{MWO}} - S_{\mathrm{MWO}}\,|}{S_{\mathrm{MWO}}} \right) \cdot 100. \tag{6.21}$$

The arithmetic mean of the absolute value of the percentage of the relative variations is:

$$\langle prv \rangle = 4.1 \pm 0.6$$

The HRT S_{MWO} deviates from S_{MWO} in the mean by 4%.

6.5 Determination of the conversion factor K

To calculate the absolute flux in the Ca II H+K lines, the Mount Wilson S-index with the help of Eq. 6.14 is used. For the conversion factor K, different values exists and are given in Table 6.2. A reason for the different conversion factors is that the methods to estimate the absolute flux in the Ca II H+K lines are different. To estimate the absolute surface flux, an empirical flux scale (Linsky et al. 1979; Hall and Lockwood 1995; Hall et al. 2007) or a measured flux (Oranje 1983) can be used. The influence of different empirical flux scales can be seen in the variation of the factor K for Hall and Lockwood (1995) and Hall et al. (2007), see Table 6.2. A V-R (Linsky et al. 1979) flux scale and a b-y (Hall 1996) flux scale was used in Hall and Lockwood (1995) and in Hall et al. (2007), respectively. Furthermore, the conversion factor K depends on the colour index $B - V$, the effective temperature T_{eff} and the S-index Hall et al. (2007).

To determine the conversion factor K, the absolute surface flux of the Ca II H+K lines of the Sun $\mathcal{F}_{\mathrm{H+K}} = 2.172 \cdot 10^6$ erg cm^{-2} s^{-1} derived by Oranje (1983) is used. Oranje (1983) determined the flux in a triangular bandpass with FWHM of 1.09 Å. He used the flux of the Sun observation from Feb. 25 1976 during the activity minimum and the Sacramento Peak Observatory (SPO) solar atlas with the absolute irradiance data of

Thekaekara (1974). Thekaekara (1974) estimated an accuracy of the absolute irradiance data of $\pm 5\%$. Therefore, I assumed a uncertainty of $\sigma_{\mathcal{F}_{\mathrm{H+K}}} \approx \pm 0.11 \cdot 10^6$ erg cm^{-2} s^{-1} for the absolute surface flux. This flux is used for consistency because the bandpass of the Ca II H+K lines in the S-index is also a triangular bandpass with FWHM of 1.09 Å.

Furthermore, Oranje (1983) determined the S-index ($S_\odot = 0.159$) of the Sun for the observation on Feb. 25 1976. This S-index is slightly too low, in comparison with the S-index $\langle S_\odot \rangle = 0.164$ of Wilson (1978, see Table 3) for 1976 and the time series of the Sun in Baliunas et al. (1995). Therefore, $\langle S_\odot \rangle = 0.164$ (Wilson 1978) is used to calculate the factor K. Furthermore, the colour index $B - V = (0.642 \pm 0.004)$ mag is used for the Sun (Cayrel de Strobel 1996). This colour index corresponds to an effective temperature $T_{\mathrm{eff}} \approx (5773 \pm 13)$ K calculated with the Eq. 6.13. This value is consistent with the literature value 5777 K (Cox 2000). Thus, I obtain for the conversion factor K:

$$K = (1.10 \pm 0.06) \cdot 10^6 \text{ erg cm}^{-2} \text{ s}^{-1}.$$

The relatively small uncertainty of the conversion factor K results from the small uncertainty of the absolute surface flux $\mathcal{F}_{\mathrm{H+K}}$.

This conversion factor K is different from the other conversion factors (Table 6.2). One reason is that the reference absolute surface flux (calculated with a empirical flux scale) and the bandpass for the surface flux are different from those used by Middelkoop (1982); Schrijver et al. (1989); Hall and Lockwood (1995); Hall et al. (2007). Another reason is the usage of different values for the colour index $B - V$, the effective temperature T_{eff} and S-index. Oranje (1983) and Rutten (1984) used the same absolute surface flux $\mathcal{F}_{\mathrm{H+K}}$ to calculate a conversion factor K, but different values for $B - V$, T_{eff} and S-index. The problem of the different values for $B - V$, T_{eff} and S-index is discussed in detail by Hall et al. (2007). Furthermore, they estimated the conversion factor $K = 1.11 \cdot 10^6$ erg cm^{-2} s^{-1} using the absolute surface flux derived by Oranje (1983). Furthermore, Hall et al. (2007) concluded that the conversion factor K is not very different from $1.0 \cdot 10^6$ erg cm^{-2} s^{-1} and depends on the bandpass.

The conversion factor K in this work is consistent with this conclusion and equal to the conversion factor K calculated by Hall et al. (2007) using the absolute surface flux derived by Oranje (1983).

Chapter 7

New photospheric flux correction with PHOENIX

To calculate the excess flux in the Ca II H+K lines, which is created by chromospheric activity, one needs a photospheric flux correction for these lines. A photospheric flux correction, which depends on the colour index $B - V$ exists only for main sequence stars up to date. A possible reason is that the research is concentrated on solar like stars.

In this Chapter, I present a new photospheric flux correction for the Ca II H+K line flux ($\mathcal{F}_{H+K}$) for main sequence, subgiant and giant stars because the sample of stars, which will be observed with the HRT includes also subgiant and giant stars. These corrections are derived using the stellar atmosphere code PHOENIX. The results of these corrections are compared to the photospheric flux correction by Noyes et al. (1984). Additionally, I create three relations to estimate the rotation period of main sequence stars, which depends on the logarithm of Ca II H+K line excess flux.

7.1 Introduction

The flux in the Ca II H+K lines ($\mathcal{F}_{H+K}$) is calculated with Eq. (6.14). This flux is a composition of the flux that is created in the photospheric and chromospheric atmospheric layers. To determine the chromospheric flux part of the $\mathcal{F}_{H+K}$ flux, one subtracts the photospheric part ($\mathcal{F}_{phot}$). Linsky et al. (1979) defined:

$$R'_{HK} = \frac{\mathcal{F}_{H+K} - \mathcal{F}_{phot}}{\sigma\ T^4_{eff}}. \tag{7.1}$$

Here, the chromospheric excess flux of the Ca II H+K lines is normalised with the bolometric flux. The logarithm of R'_{HK} is one of the most important activity indicators. With log R'_{HK}, it is possible to estimate the rotation period (Noyes et al. 1984) (Sect. 7.5) and the age of the stars (Donahue 1993). Further, Henry et al. (1996) defined the activity state of an object using the activity indicator log R'_{HK} (Sect. 8.1).

The problem is that one cannot measure directly the photospheric flux in the Ca II H+K lines. To obtain the photospheric flux for these lines, one can use a synthetic spectrum. Another method is to define a wavelength range in a spectrum where the flux is only created in the photospheric atmospheric layer. The total flux in this range is used as photospheric correction. This method was used by Noyes et al. (1984) to create a photospheric

flux relation, which depends on the colour index $B - V$. This relation was estimated with six main sequence stars in the $B - V$ range $0.44 < B - V < 0.82$. To determine the photospheric flux part in the H+K photometer bandpass (Sect. 6.1), Noyes et al. (1984) used the photospheric contribution outside the H1 and K1 points of the Ca II H+K line profiles. Noyes et al. (1984) denoted R_{phot} as the ratio of the photospheric flux and bolometric flux of the star:

$$R_{phot} = \frac{\mathcal{F}_{\mathrm{phot}}}{\sigma \ T_{eff}^4},$$ (7.2)

where $\mathcal{F}_{\mathrm{phot}}$ is the photospheric flux, σ the Stefan Boltzmann constant and T_{eff} the effective temperature of the star. To obtain a relation between R_{phot} and the colour index $B - V$, Noyes et al. (1984) fitted $\log R_{\mathrm{phot}}$ from Ca II K lines of six main sequence stars in the range $0.44 < B - V < 0.82$ with a cubic polynomial fit. The equation has the form (Noyes et al. 1984):

$$\log \ R_{phot} \quad = \quad -4.898 + 1.918(B - V)^2 - 2.893(B - V)^3.$$ (7.3)

They used this relation also for objects with $B - V > 0.82$ and adopted a small deviation from the correction for $B - V > 1.0$, because Hartmann et al. (1984) estimated a smaller photospheric flux for $B - V > 1.0$ (Noyes et al. 1984).

This photospheric flux relation has not been determined for subgiant and giant stars. To estimate the excess flux, it is possible to calculate a synthetic spectrum for individual objects. For a large sample of stars, this is not practical because huge computing time is necessary to create a synthetic spectrum. It is more convenient to use a photospheric flux relation depending on $B - V$. To create a relation for subgiant and giant stars, I used synthetic spectra. For consistency, I also used this method to create a relation for main sequence stars. These spectra are computed with the atmosphere code PHOENIX.

7.2   The stellar atmosphere code PHOENIX

PHOENIX is a multi-purpose stellar atmosphere code and can be used to calculate synthetic spectra (Hauschildt and Baron 1999). This atmosphere code is very flexible because one can calculate atmosphere models and synthetic spectra not only for main sequence or giant stars, but also for quite different objects with an atmosphere, e. g. white dwarfs, novae and supernovae.

For a given atmosphere model and stellar parameters (T_{eff} and two of the following four parameters: $\log g$, $M/M_\odot$, $L/L_\odot$ and R), PHOENIX solves the hydrostatic, rate and radiative transfer equations to obtain the radiation field. I used the stellar parameters T_{eff}, $\log g$ and $M/M_\odot$ for the atmosphere model calculation. PHOENIX checks the results of the radiation field after each iteration whether the atmosphere is in a radiative equilibrium. If the atmosphere is not in radiative equilibrium, PHOENIX performs a temperature correction (Hauschildt et al. 2003b). In a new iteration, PHOENIX solves again the hydrostatic, rate and radiative transfer equations until the maximum number of iterations has been reached or until the temperature correction is less than a given value. For the calculation of an atmosphere model, one can use two approximations. The first approximation is to assume an atmosphere, which is in local thermodynamic equilibrium

(LTE) or an atmosphere, which is not in local thermodynamic equilibrium (NLTE). For the atmosphere calculation, one can choose individually for each species whether to use LTE or NLTE approximation.

7.2.1 LTE

In the LTE approximation, one assumes that the particles and the radiation field in a local space element of the atmosphere are in thermodynamic equilibrium. In thermodynamic equilibrium, the particle density is high enough to uniformly distribute the energy via particle collisions. Therefore, an energy equilibrium is reached. Hence, it is possible to define a temperature for this local space element. Using this temperature, the radiation field and the population of the energy levels of the elements can be described. In PHOENIX, the Saha-Boltzmann-distribution is used for the LTE calculation and gives the ratio between the population n_i in the level i and the population n_c in the ionisation state c and is given by (Rutten 2008):

$$\frac{n_c}{n_i} = \frac{1}{N_e}\frac{2g_c}{g_i}\left(\frac{2\pi m_e kT}{h^2}\right)^{3/2} e^{-\chi_{ci}/kT}. \tag{7.4}$$

Here, N_e is the electron density, m_e the electron mass, g_i and g_c the statistical weights for the level i and c, respectively, k the Boltzmann constant, h the Planck constant, T the temperature and χ the ionisation energy between the level i and c.

7.2.2 NLTE

In the NLTE approximation, the radiation field differs significantly from a Planck function with the local kinetic temperature. Furthermore, the particle density is not high enough and the particle collisions are not sufficient to reach thermodynamic equilibrium. Here, it is not possible to define a local temperature, which describes both the radiation field and the population of the energy levels. Therefore, the Saha-Boltzmann-distribution cannot be used to calculate the population of the energy levels. In the case of NLTE, PHOENIX assumes a statistical equilibrium. In the statistical equilibrium, the radiation field and population of the energy levels are constant in time. To compute the population of the energy levels, PHOENIX solves the rate equations, which are described by (Hauschildt and Baron 1999):

$$\sum_{j<i} n_j(R_{ji} + C_{ji}) - n_i \left\{ \sum_{j<i}\left(\frac{n_j^*}{n_i^*}\right)(R_{ij} + C_{ji}) + \sum_{j>i}(R_{ij} + C_{ij}) \right\}$$
$$+ \sum_{j>i} n_j \left(\frac{n_i^*}{n_j^*}\right)(R_{ji} + C_{ji}) = 0. \tag{7.5}$$

Here, R_{ji} are the radiative rates and C_{ji} the collisional rates. Further, n_i is the NLTE population density of the level i and n_i^* is the LTE population density of the level i and is given by (Hauschildt and Baron 1999):

$$n_i^* = \frac{g_i}{g_k}n_k\frac{2h^3 n_e}{(2\pi m)^{3/2}(kT)^{3/2}}e^{-\frac{E_i - E_k}{kT}}. \tag{7.6}$$

Here, g_i and g_k are the statistical weights for the level i and k, respectively, n_k the population density of the ground state of the next higher ionisation stage, n_e the NLTE electron density, m the electron mass, E_i the excitation energy of the level i and E_k the ionisation energy from the ground state to the corresponding ground state of the next higher ionisation stage.

7.3   Calculation of the synthetic spectra

7.3.1   Stellar parameters

For the photospheric flux correction, only the spectral types with small rotation velocities are used because if the rotation velocity is too high, the Ca II H+K lines become too broad. This has an influence on the Mount Wilson S-index. For low active stars, the line core increases and the S-index will be larger. On the other hand for strong active stars, line core decreases and the S-index will be lower. Hence, the S-index is only usable for slow rotators. The influence of the $\log R'_{\mathrm{HK}}$ is shown in Fig. B.7 (Schröder et al. 2009).
The stellar parameters for the calculation are averaged parameters, which depend on the colour index $B-V$ and are given in Table (A.3) for main sequence stars and in Table (A.4) for giant stars (Gray et al. 2003). The total rotation velocity ($vsini'$) is a combination of the microturbulence (ξ) and the true rotational velocity ($vsini$) and is calculated as:

$$vsini' \quad = \quad \sqrt{\xi^2 + vsini^2}. \tag{7.7}$$

Hereafter, the total rotation velocity ($vsini'$) is designated as ($vsini$). The macroturbulence is considered in the spectrum calculation.
For the subgiant stars, the average stellar parameters $M/M_\odot$, $\log g$, T_{eff} and $vsini$ are not given in Gray et al. (2003). To obtain the average stellar parameters, I determined the average stellar parameters for $B-V = (0.44, 0.5, 0.6, 0.7, 0.8, 0.9, 1.0, 1.1)$.
The parameters $M/M_\odot$ and $\log g$ are taken from the star catalogue by Allende Prieto and Lambert (1999). I selected the subgiant stars from this catalogue and averaged the $M/M_\odot$ and $\log g$ over a $B-V$ range ± 0.025 around the above $B-V$ values (Fig. B.2 & B.4). The results are given in Table (A.5).
The effective temperatures (T_{eff}) corresponding to these $B-V$ are calculated with Eq. 6.13.
To approximate rotational velocities ($vsini$), which depend on $B-V$, I selected a set of rotational velocities ($vsini$) from Schrijver and Pols (1993) (Fig. B.5). These values are averaged for the $B-V$ and these values are fitted in the range from $0.6 < B-V < 1.1$. The results are given in Table (A.5). The average rotational velocity ($vsini$) of subgiants rises at $B-V < 0.55$ relatively fast and the Ca II H+K lines become too broad. For these objects, the S-index is not usable. However, these are not only fast rotators of subgiants in the range from $0.44 < B-V < 0.55$, but also slow rotators. Therefore, I set the rotation velocities for $B-V = 0.44$ and $B-V = 0.5$ to 26.0 km/s. This is the averaged rotation velocity of giants at the $B-V = 0.76$ (Fig. B.6) and a threshold of the velocity for, which the influence on the line broadening through rotation is small enough to ignore.

7.3.2 Spectrum calculation

To calculate the synthetic spectra, I assumed a solar metallicity in the synthetic spectra and used the solar abundances by Asplund et al. (2005). In a first step to create a synthetic spectrum, the atmosphere model for the corresponding stellar parameter was calculated with the LTE approximation. The initial atmosphere model was a GAIA model (Hauschildt et al. 2003a) with stellar parameters comparable to my average T_{eff} and $\log g$. The next step was to compute the final atmosphere model. Here, the NLTE approximation was used for several elements. The elements were H I, He I-II, Fe I-III, Ca I-III, Na I-II, Mg I-III, K I-II, Al I-II and Si I-II. The reason, why I used not only H I, He I-II, Fe I-III and Ca I-III is, that these spectra will be usable for other investigations, e. g., the Ca II triplet in the near infrared. At last, a high resolution spectrum was computed.

Furthermore, these synthetic spectra are used to determine the radial velocity shift via a cross correlation. This is performed to determine the S-Index for the Ca II H+K region (Sect 6.4.1). The spectra are also used to measure the radial velocity shifts of HD79028 and HD120136 (Sect. 9.3.2 and 9.4.2). In this cases, a new high resolution spectrum was computed.

7.4 Results

7.4.1 Photospheric relation depending on the colour index B-V

Before the photospheric flux of the Ca II H+K lines ($\mathcal{F}_{\mathrm{phot}}$) is calculated, one has to consider the rotational velocity ($vsini$) and the instrumental broadening. The instrumental broadening corresponds to a spectral resolution of R = 190000 (Beckers et al. 1976). This resolution is similar to the spectral resolution of the spectrograph with, which the solar spectrum of the SPO atlas (Beckers et al. 1976) was obtained.

$\mathcal{F}_{\mathrm{phot}}$ in unit of [erg/(cm^2 s)] is the integrated flux in the Ca II H+K lines of synthetic spectra in the same bandpass as the absolute surface flux $\mathcal{F}_{\mathrm{H+K}}$ derived by Oranje (1983). Oranje (1983) used the same bandpass as the Mount Wilson S-index in the line cores of the Ca II H+K lines.

In Fig. 7.1, $\log \mathcal{F}_{\mathrm{phot}}$ vs. the colour index $B - V$ is shown for main sequence, subgiant and giant stars. These $\log \mathcal{F}_{\mathrm{phot}}$ show a linear dependence on $B - V$. The solid line is the linear fit for the main sequence stars, the dashed line the fit for the subgiant stars and the dash-dotted line the fit for the giant stars. The fits of $\log \mathcal{F}_{\mathrm{phot}}(B - V)$ are given by the following equations:

for main sequence stars ($0.44 \leq B - V \leq 1.28$):

$$\log \mathcal{F}_{\mathrm{phot}} = (7.488 \pm 0.012) - (2.057 \pm 0.014)(B - V), \qquad (7.8)$$

for subgiant stars ($0.44 \leq B - V \leq 1.1$):

$$\log \mathcal{F}_{\mathrm{phot}} = (7.567 \pm 0.013) - (2.251 \pm 0.016)(B - V), \qquad (7.9)$$

for giant stars ($0.76 \leq B - V \leq 1.18$):

$$\log \mathcal{F}_{\mathrm{phot}} = (7.607 \pm 0.025) - (2.369 \pm 0.026)(B - V). \qquad (7.10)$$
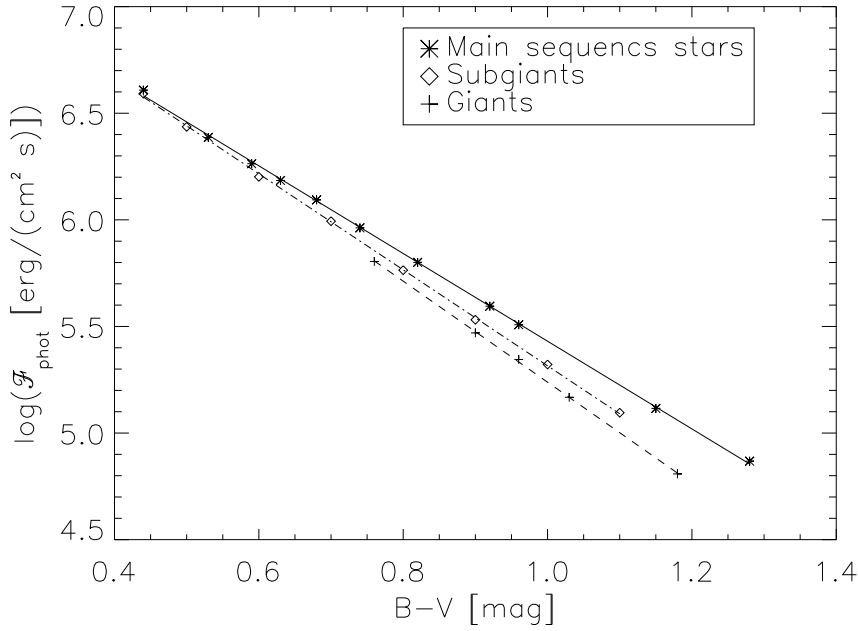
Figure 7.1: The photospheric flux vs. the colour index B-V

The standard deviation of the residuals are:

> for main sequence stars = 0.011,
> for subgiant stars = 0.009,
> for giant star = 0.007.

The spectra are calculated with solar metallicity. The question is, how strong is the influence of the metallicity on $\mathcal{F}_{\mathrm{phot}}$? To check the influence of the metallicity, I computed as example the spectra for two spectral types (G2V and K0V) with different metallicities (z=+0.5, 0.0, -0.25, -0.5, -0.75, -1.0) and then the $\mathcal{F}_{\mathrm{phot}}$ are calculated. Here, the global metallicity was changed (all elements). Normally, the metallicities of the different elements in stars are not equal for all elements, but mostly the metallicity of Fe in a star is estimated and this is assumed to be the global metallicity of the star. In Fig. 7.2, $\mathcal{F}_{\mathrm{phot}}$ vs. metallicity is shown. One sees that the slope in the trends are different and linear. The slope is represented in Table 7.1. The slope between the $\mathcal{F}_{\mathrm{phot}}$ vs. metallicity is greater for G2V than for K2V. Though, the percentage change in $\mathcal{F}_{\mathrm{phot}}$ is slightly greater for K0V than

	Slope [erg/(cm^2 s) / z]
G2V	$(-5.70 \pm 0.26) \cdot 10^5$
K0V	$(-2.63 \pm 0.15) \cdot 10^5$

Table 7.1: Slopes of the trends in the $\mathcal{F}_{\mathrm{phot}}$ vs. metallicity z
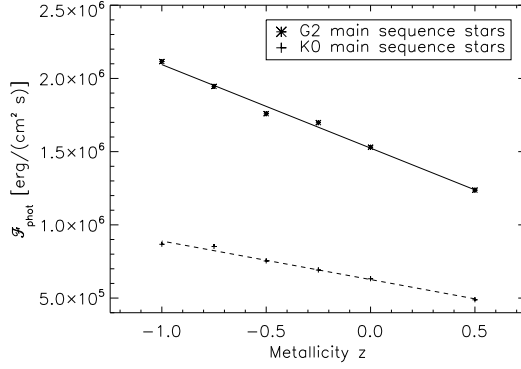
Figure 7.2: $\mathcal{F}_{\mathrm{phot}}$ vs. metallicity z
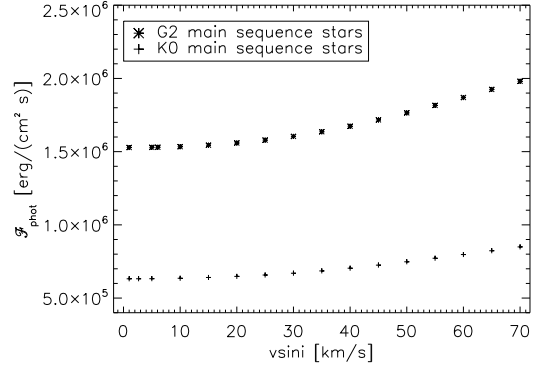
Figure 7.3: $\mathcal{F}_{\mathrm{phot}}$ (z=0) vs. *vsini*
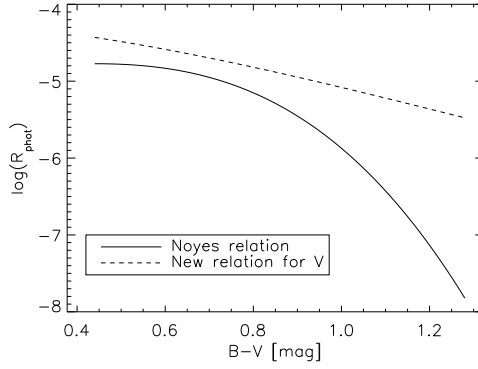
Figure 7.4: The Noyes relation (Noyes et al. 1984) and the new relation for main sequence star vs. B-V
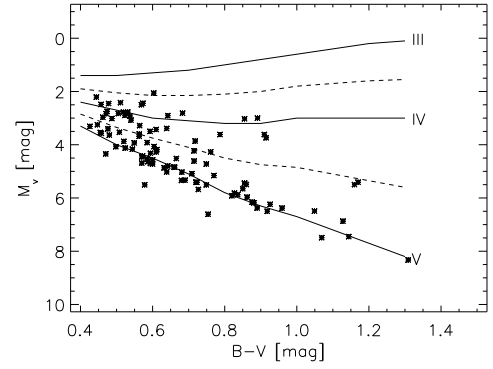
Figure 7.5: The position of all objects in the data set by Noyes et al. (1984) in the H-R diagram

for G2V. If one compares $\mathcal{F}_{\mathrm{phot}}(z = 0)$ to $\mathcal{F}_{\mathrm{phot}}(z = -0.1)$ and $\mathcal{F}_{\mathrm{phot}}(z = -0.3)$, the $\mathcal{F}_{\mathrm{phot}}$ is 3.7% and 11, 2%, respectively and 4.2% and 12.6%, respectively lower, for the G2V and K0V, respectively.

These two examples show the impact of metallicity on $\mathcal{F}_{\mathrm{phot}}$. Thus, the $\mathcal{F}_{\mathrm{phot}}$ is too small for a star with z$\ll$ 0 and R'_{HK} too high and in reverse for z$\gg$ 0.

Furthermore, the difference of *vsini* of a star to the average *vsini* can have an influence on $\mathcal{F}_{\mathrm{phot}}$. To check this influence, $\mathcal{F}_{\mathrm{phot}}$ at z=0 is calculated for G2V and K0V with different *vsini*. The average *vsini* for G2V and K0V is 6.1 km/s and 2.6 km/s, respectively. $\mathcal{F}_{\mathrm{phot}}$ vs. *vsini* is shown in Fig. 7.3. One can see that the change in $\mathcal{F}_{\mathrm{phot}}$ is not significant for *vsini* $\leq$ 25 km/s for G2V and K2V, respectively. This *vsini* is a factor of 4 and 10 larger than the average *vsini* of G2V and K2V, respectively. $\mathcal{F}_{\mathrm{phot}}$ at *vsini* = 25 km/s is only 3.2% and 4.0% greater than $\mathcal{F}_{\mathrm{phot}}$ at the average *vsini* for G2V and K0V, respectively.

7.4.2 Comparison with the photospheric correction by Noyes et al. (1984)

The Noyes relation Eq. 7.3 and the new relation Eq. 7.8 are plotted in Fig. 7.4 where the fluxes are plotted as log R_{phot}. One has to note that the log R_{phot} by Noyes et al.
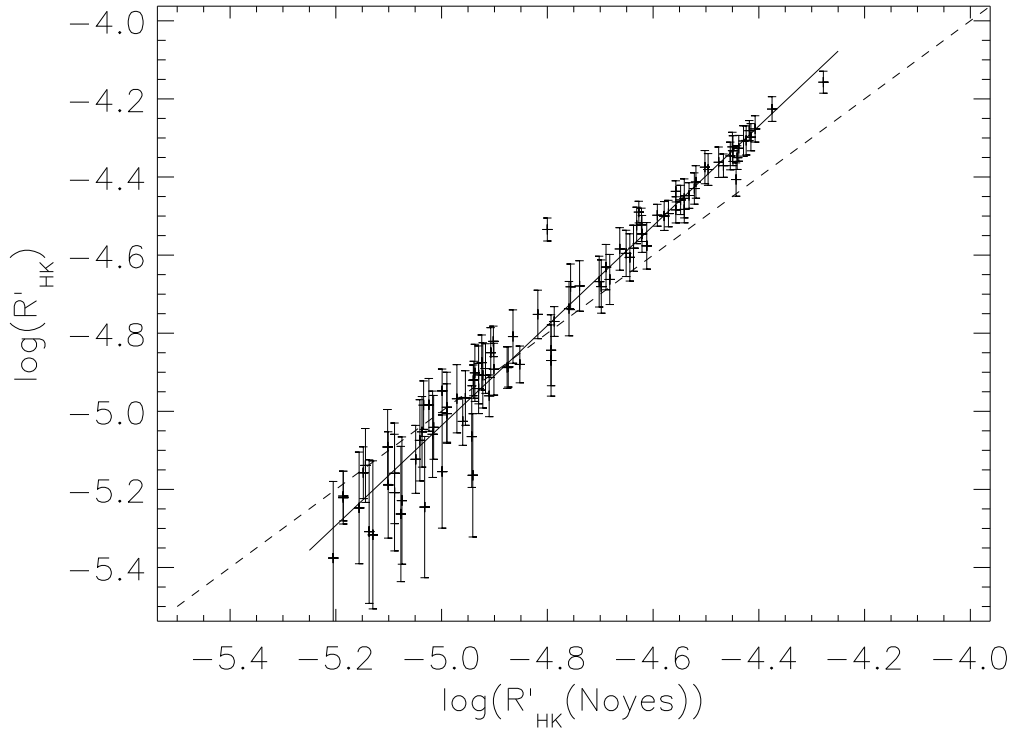
Figure 7.6: Comparison of the $\log R'_{\mathrm{HK}}(Noyes)$ and $\log R'_{\mathrm{HK}}$ with the new relations

(1984) are significantly smaller than the new relation and shows a strong decrease for $B - V > 0.90$. These differences result from the method and the $B - V$ range of objects used for determining the $\log R_{\mathrm{phot}}$ relation.

Next, the $\log R'_{\mathrm{HK}}$ by Noyes et al. (1984) (hereafter $\log R'_{\mathrm{HK}}(Noyes)$) and $\log R'_{\mathrm{HK}}$ calculated with the new photospheric correction are compared. For the $\log R'_{\mathrm{HK}}$, the $\mathcal{F}_{\mathrm{H+K}}$ was calculated with the S-indices from Noyes et al. (1984) and with Eq. 6.14 with the conversion factor $K = 1.10 \cdot 10^6$ erg cm^{-2} s^{-1} from this work. The effective temperature was calculated with Eq. 6.13 and the C_{cf} factor was calculated with Eq. 6.10 and 6.11. To calculate the effective temperature and the C_{cf}, the colour indices from the Hipparcos Main Catalogue are used.

First, the luminosity class of the object was defined, see Sect. 6.4.1. In Fig. 7.5, the absolute magnitude vs. $B - V$ for the objects is plotted. The solid lines represent the average absolute magnitudes for main sequence, subgiant and giant stars as defined in Allen (1976). One sees that the data set by Noyes et al. (1984) includes not only main sequence stars, but also a lot of subgiant stars and one giant star. Thereafter, the $\log R'_{\mathrm{HK}}$ is calculated with the new photospheric correction and these values are plotted vs. the $\log R'_{\mathrm{HK}}(Noyes)$ in Fig 7.6.

The results of the $\log R'_{\mathrm{HK}}$ with the new photospheric correction are significantly different from the $\log R'_{\mathrm{HK}}(Noyes)$ for $\log R'_{\mathrm{HK}}(Noyes) \geq 5.0$ and $\log R'_{\mathrm{HK}}(Noyes) > -4.6$. For objects with a $\log R'_{\mathrm{HK}}(Noyes) \geq 5.0$, the $\log R'_{\mathrm{HK}}$ is smaller and these objects are redefined

as subgiants. On the other hand, the $\log R'_{\mathrm{HK}}$ is clearly greater than $\log R'_{\mathrm{HK}}(Noyes)$ for $\log R'_{\mathrm{HK}}(Noyes > -4.6$.

The trend between $\log R'_{\mathrm{HK}}$ and $\log R'_{\mathrm{HK}}(Noyes)$ is represent by a solid line in Fig. 7.6. The slope is ≈ 1.3. The values of $\log R'_{\mathrm{HK}}$ and $\log R'_{\mathrm{HK}}(Noyes)$ are given in Table A.6.

7.5 R'_{HK} vs. the rotation period

Noyes et al. (1984) found a relation between the ratio of the rotation period (P) of a star to the convective turnover time τ_c and the R'_{HK}. The ratio P/τ_c is called Rossby number Ro. The relation between Ro and R'_{HK} has the form (Noyes et al. 1984):

$$\log Ro \;=\; \log\left(\frac{P}{\tau_c}\right) \;=\; 0.324 - 0.400y - 0.283y^2 - 1.325y^3, \qquad (7.11)$$

where $y = \log(R'_{\mathrm{HK}}10^5)$. The convective turnover time τ_c is given as (Noyes et al. 1984):

$$\tau_c \;=\; \begin{cases} 1.362 - 0.166x + 0.025x^2 - 5.323x^3 & x > 0 \\ 1.362 - 0.14x & x < 0 \end{cases} \qquad (7.12)$$

where $x = 1 - (B - V)$.

I calculated the rotation period with the Eq. 7.11 and 7.12 and the $\log R'_{\mathrm{HK}}$. To calculate the convective turnover time, I used the colour indices from the Hipparcos Main Catalogue. Thereafter, I compared the results to the values by Noyes et al. (1984). Therefore, the standard deviations of the residuals are calculated. For the periods calculated with $\log R'_{\mathrm{HK}}$, I obtained a standard deviation of the residuals of 3.9 day whereas for the periods calculated by Noyes et al. (1984), I obtained a standard deviation of the residuals 2.6 day. The periods calculated with the $\log R'_{\mathrm{HK}}$ deviate strongly from the values by Noyes et al. (1984). One possible reason could be the different calculation of R'_{HK}, which results in different relation parameters between the R'_{HK} and the Rossby number. Therefore, I determined the parameter in the relation between the Rossby number and the new $\log R'_{\mathrm{HK}}$.

For this calculation, I collected additional rotation periods for objects, which do not have a rotation period in Noyes et al. (1984). Furthermore, I replaced the S-indices by the average S-indices by Baliunas et al. (1995) because these values are obtained from a longer time series. Additionally, I removed the variable stars of RS CVn types (HD17925, HD82885 and HD156026) from this list. RS CVn is a close binary where the objects are coupled by gravity (Strassmeier 1997). One also assumes that the stars are possibly connected by the magnetic field (Linsky 1985). This can have an influence on the activity level of the stars. Additionally, I collected objects with the corresponding rotation period and S-index and added them to this list. The data set, which is used for the calculation, is given in (Table A.7). To determine the relation between $\log R'_{\mathrm{HK}}$ and Ro, I used only the main sequence stars from Table A.7. In Fig. 7.7, $\log Ro$ vs. $\log(R'_{\mathrm{HK}}10^5)$ is shown and in Fig. 7.8 $\log Ro$ vs. $R'_{\mathrm{HK}}10^5$. One sees that the relation is simplified to a linear relation if $R'_{\mathrm{HK}}10^5$ is used instead of $\log(R'_{\mathrm{HK}}10^5)$. The correlation coefficient r is $r = -0.94$ for $R'_{\mathrm{HK}}10^5$ vs. $\log Ro$ and is slightly greater than for $\log(R'_{\mathrm{HK}}10^5)$ vs. $\log Ro$ with $r = -0.90$. The solid line in Fig 7.8 represents the fit and the equation is obtained as:

$$\log Ro \;=\; \log\left(\frac{P}{\tau_c}\right) \;=\; (0.448 \pm 0.026) - (0.0130 \pm 0.0007)(R'_{\mathrm{HK}}10^5). \quad (7.13)$$
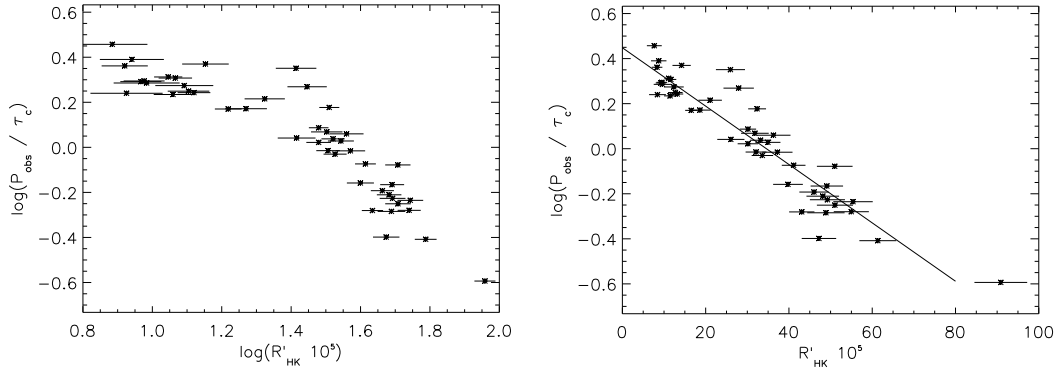
Figure 7.7: $\log(P_{obs}/\tau_c)$ vs. $\log(R'_{\mathrm{HK}}10^5)$ Figure 7.8: $\log(P_{obs}/\tau_c)$ vs. $R'_{\mathrm{HK}}10^5$ with the linear fit

The standard deviation of the residuals is:

$$\text{Standard deviation of residuals} = 3.1 \text{ day.}$$

The results are compared with the results by Noyes et al. (1984). To compare the results, I used only the stars in the intersection of my and the Noyes data set. The standard deviations of residuals are 3.1 day for the results with Eq. 7.13 and 2.5 day for the results by Noyes et al. (1984). Here, the standard deviations of the residuals for the results with Eq. 7.13 are greater than the standard deviation of the residuals with the periods calculated by Noyes et al. (1984). The possible reason is the convective turnover time τ_c. Noyes et al. (1984) used the $\log R'_{\mathrm{HK}}(Noyes)$ to find the best solution for the τ_c relation with $\alpha = 1.9$. Here, α is the ratio of the mixing length to the scale height. On the basis of this fact, the periods calculated with Eq. 7.13 and the R'_{HK} compare very well with the periods calculated by Noyes et al. (1984).

For the sake of completeness, I note that Stepien (1994) found a linear relation between the $\log R'_{\mathrm{HK}}(Noyes)$ and Rossby number Ro. He used the convective turnover time τ_c, which he found in Stepien (1989), to calculate the Rossby number .

7.6 $\log \Delta\mathcal{F}'_{\mathrm{HK}}$ vs. the rotation period

In this section, the excess flux of the Ca II H+K lines vs. the rotation period will be investigated to find a more accurate relation to estimate the rotation period for the main sequence stars (compared to Eq. 7.13). The excess flux is calculated with:

$$\Delta\mathcal{F}'_{\mathrm{HK}} = \mathcal{F}_{\mathrm{HK}} - \mathcal{F}_{\mathrm{phot}}, \tag{7.14}$$

where $\mathcal{F}_{\mathrm{phot}}$ is calculated with the Eq. 7.8 - 7.10. This investigation is performed with the same data set as used for the determination of Eq. 7.13 (Table A.7). In the first paragraph, the influence of the stellar age is investigated. In the second paragraph, a relation between $\Delta\mathcal{F}'_{\mathrm{HK}}$ and the rotation period is created for main sequence stars.

7.6.1   The influence of the stellar age

First, the rotation period vs. $\log \Delta\mathcal{F}'_{\mathrm{HK}}$ is shown in Fig. 7.9. The plus signs and the

Figure 7.9: The rotation period P vs. log $\Delta\mathcal{F}'_{\mathrm{HK}}$

Figure 7.10: The log S vs. the colour index B-V

asterisks label the young and old stars, respectively, by Noyes et al. (1984) and based on the definition by Vaughan (1980). Vaughan (1980) found that he could split the logarithm of the Mount Wilson S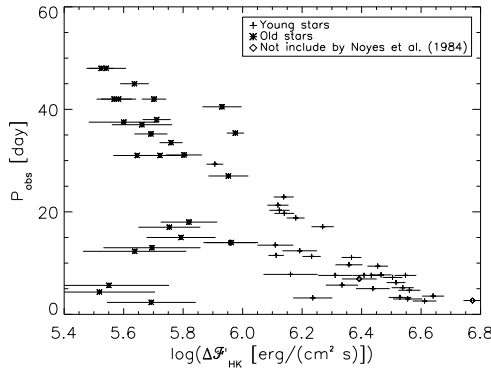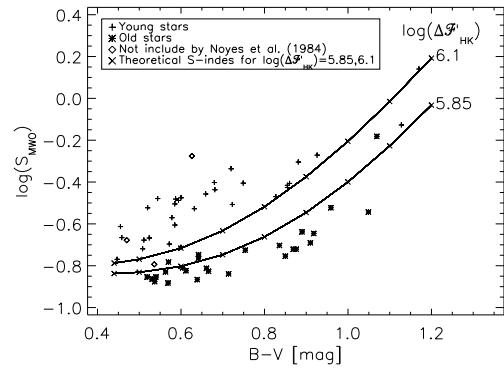-index from Wilson (1978) vs. $B - V$ in two areas, in young and old star. The border is a linear relation whereas the stars above this border are young star and below the border are old stars. The diamonds label the objects, which are not included in Noyes et al. (1984).

In Fig. 7.9, a clear separation between young and old stars is found. The old stars show a long rotation period and a small $\Delta\mathcal{F}'_{\mathrm{HK}}$ and the young stars a short rotation period and a high $\Delta\mathcal{F}'_{\mathrm{HK}}$. This finding is consistent with theory. In contrast to theory, some stars show a small rotation period and $\Delta\mathcal{F}'_{\mathrm{HK}}$. This will be discussed in Sect. 7.6.2.

In the region between log $\Delta\mathcal{F}'_{\mathrm{HK}} = 5.85$ and log $\Delta\mathcal{F}'_{\mathrm{HK}} = 6.1$, the object density is very low. Here, only five stars are located: one young, three old and one star which was not included in Noyes et al. (1984). Additionally, I calculated the theoretical S-indices for log $\Delta\mathcal{F}'_{\mathrm{HK}} = 5.85$ and log $\Delta\mathcal{F}'_{\mathrm{HK}} = 6.1$ for $B-V = (0.44, 0.5, 0.6, 0.7, 0.8, 0.9, 1.0, 1.1, 1.2)$. For this purpose, I used the corresponding relations for main sequence stars, Eq. 7.8 and Eq. 6.10, the conversion factor $K = (1.10 \pm 0.06) \cdot 10^6$ erg cm^{-2} s^{-1} for the Eq. 6.14. The effective temperature in Eq. 6.14 is calculated with Eq. 6.13.

The S-indices are plotted in Fig. 7.10. It shows the individual log S of the objects vs. $B - V$. The objects are labelled as in Fig. 7.9. The observations log $S(B - V)$ show a clear separation between young and old stars. However, the border lines of the gap are nicely marked by the theoretical log $S(B - V)$ lines calculated for log $\Delta\mathcal{F}'_{\mathrm{HK}} = 5.85$ and 6.1, respectively. I conclude that the region $5.85 <$ log $\Delta\mathcal{F}'_{\mathrm{HK}} < 6.1$ is a transition region between young and old stars. In this region, the Vaunghan-Preston gap is located. The Vaunghan-Preston gap was found by Vaughan and Preston (1980). It is a region $(0.5 < B - V < 1.0)$ with a very low objects density in the log S vs. $B - V$ plot.

7.6.2 Relation between log $\Delta\mathcal{F}'_{\mathrm{HK}}$ and rotation period

Here, I investigated the relation between $\Delta\mathcal{F}'_{\mathrm{HK}}$ vs. rotation period. Rutten (1987) found that log $\Delta\mathcal{F}'_{\mathrm{HK}}$ is correlated with log P and that the relation depends on the $B - V$ ranges, $0.5 < B - V < 0.6$, $0.6 < B - V < 0.7$, $0.7 < B - V < 0.9$, $0.9 < B - V < 1.1$ and
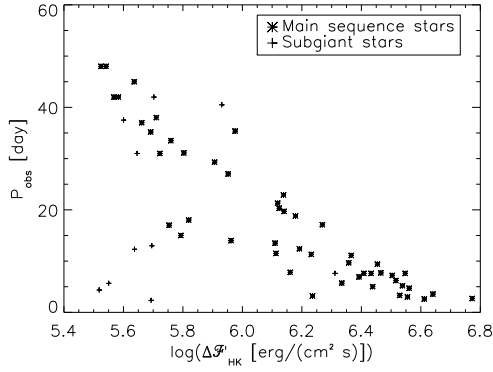
Figure 7.11: The rotation period P vs. log $\Delta\mathcal{F}'_{HK}$ labelled as main sequence, subgiant and giant stars
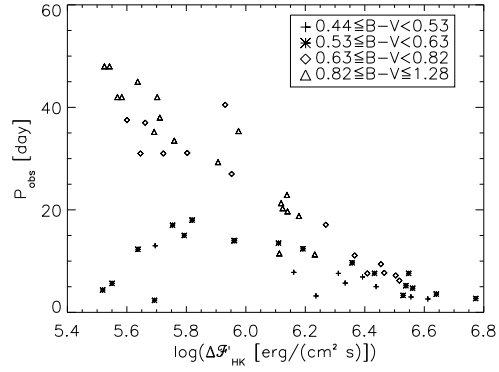
Figure 7.12: The rotation period P vs. log $\Delta\mathcal{F}'_{HK}$ labelled for different $B - V$ ranges

$1.1 < B - V < 1.3$. $\Delta\mathcal{F}'_{HK}$ is calculated by (Rutten 1987):

$$\Delta\mathcal{F}'_{HK} \quad = \quad \mathcal{F}_{HK} - \mathcal{F}_{min} \tag{7.15}$$

where $\mathcal{F}_{min}$ is the minimal flux of the Ca II H+K lines. $\mathcal{F}_{min}$ was defined empirically by Rutten (1987) as the lower envelope of the logarithm of the measured $\mathcal{F}_{HK}$ vs. $B - V$. Stepien (1989) used this dependency of log $\Delta\mathcal{F}'_{HK}$ on log P for different $B - V$ ranges to determine a convective turnover time τ_c depending on $B - V$ in order to find a relation between the $\Delta\mathcal{F}'_{HK}$ and the Rossby number. Contrary to the investigation in this work, Stepien (1989) wanted to find a relation between Rossby number and excess flux. Another difference is the method to calculate $\Delta\mathcal{F}'_{HK}$. Furthermore, Stepien (1989) used calculated rotation periods whereas only observed periods are used in this work.

This investigation was performed with the data set (Table A.7), which was composed for the determination of Eq. 7.13. In Fig. 7.11 and 7.12, the rotation period P vs. log $\Delta\mathcal{F}'_{HK}$ is shown. The former plot features different labels for main sequence and subgiant stars whereas the letter plot distinguishes between different $B - V$ ranges. From a comparison between Fig. 7.9 and Fig. 7.11, it is clear that the old stars with a small rotation period and $\Delta\mathcal{F}'_{HK}$ are subgiants and are located in the range $0.53 \le B - V < 0.63$, see Fig. 7.12. These stars are evolved F stars. A possible reason is that the magnetic breaking has started after the main sequence period for these stars. This is only a hypothesis and incapable of proof yet. The main sequence stars from this data set are selected with the method described in Sect. 6.4.1. Additionally, I defined a transition area between the main sequence and subgiant stars, see Fig. 7.13. The border of the transition area is given in Table 7.2. This transition area is introduced to sort out stars in the transition phase from main sequence to subgiant stars.

In Fig. 7.14, one can see two general trends between the rotation period (P) and the excess flux of the Ca II H+K lines ($\Delta\mathcal{F}'_{HK}$) for stars with $B - V$ of $< 0.63 \le$. The colour index $B - V = 0.63$ mag is average colour index of stars of the spectral type of G2V. This border was obtained by fitting the trends for different $B - V$ ranges. For the limits of these ranges, the average $B - V$ for the spectral types (Table A.3) were used. The slopes and the correlation coefficients r of the two general trends are given in Table 7.3. To check the
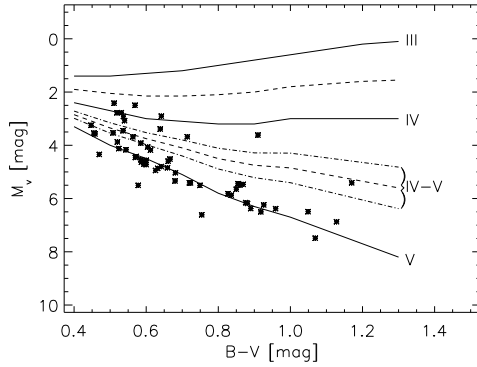
Figure 7.13: H-R diagram of the data
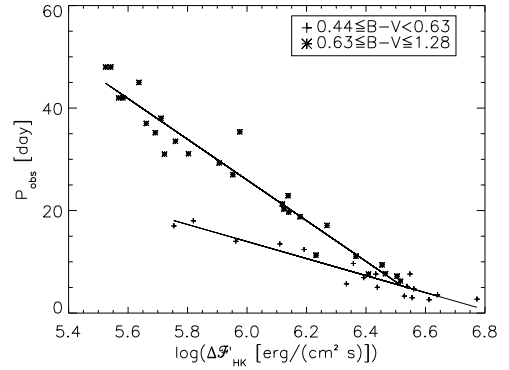
Figure 7.14: The rotation period vs. log $\Delta\mathcal{F}'_{\mathrm{HK}}$ of main sequence stars. The lines denote the two main trends

$B - V$	0.4	0.5	0.6	0.7	0.8	0.9	1.0	1.1	1.2	1.3
VMAG lower	2.7	3.2	3.5	3.8	4.1	4.3	4.3	4.5	4.6	4.8
VMAG upper	3.0	3.5	4.0	4.4	4.9	5.2	5.4	5.7	6.1	6.4

Table 7.2: The lower and upper absolute magnitude (VMAG) depending on the colour index $B - V$ of the transition area between the main sequence and subgiant stars

significance of the correlation, a t-Student test is performed (Sect. 5.1) and the results are also given in Table 7.3. The t_{cutoff} is ≥ 3.96 and ≥ 3.71 for the range $0.44 \leq B - V < 0.63$

	Slope [day/$\Delta\mathcal{F}'_{\mathrm{HK}}$]	$\sum$ of objects	r	$\mid t \mid$
$0.44 \leq B - V < 0.63$	(-16.7 ± 1.3)	18	-0.95	12.7
$0.63 \leq B - V \leq 1.28$	(-39.8 ± 1.8)	27	-0.98	22.3

Table 7.3: Slopes, correlation coefficient r of the trends in Fig. 7.14, the corresponding t value of the t-Student test

and $0.63 \leq B - V \leq 1.28$, respectively, for a significance level $\geq 99.9\%$ (Bronstein et al. 2001). The correlation coefficients and the t values show a clear correlation. The data of the range $0.63 \leq B - V \leq 1.28$ are divided in two sub-samples to obtain a higher accuracy. The two sub-samples are $0.63 \leq B - V < 0.82$ and $0.82 \leq B - V \leq 1.28$. This separation is possible because the convective turnover time depending on $B - V$ is included in the parameter of the equations. Further separations are not reasonable, since the statistics worsens. The correlation coefficient and t value are given in Table 7.4. The t_{cutoff} is ≥ 4.59 and ≥ 4.07 for the range $0.63 \leq B - V < 0.82$ and $0.82 \leq B - V \leq 1.28$, respectively, for a significance level $\geq 99.9\%$ (Bronstein et al. 2001). In Fig. 7.15, the lines represent the individual relations between rotation period and the excess flux.
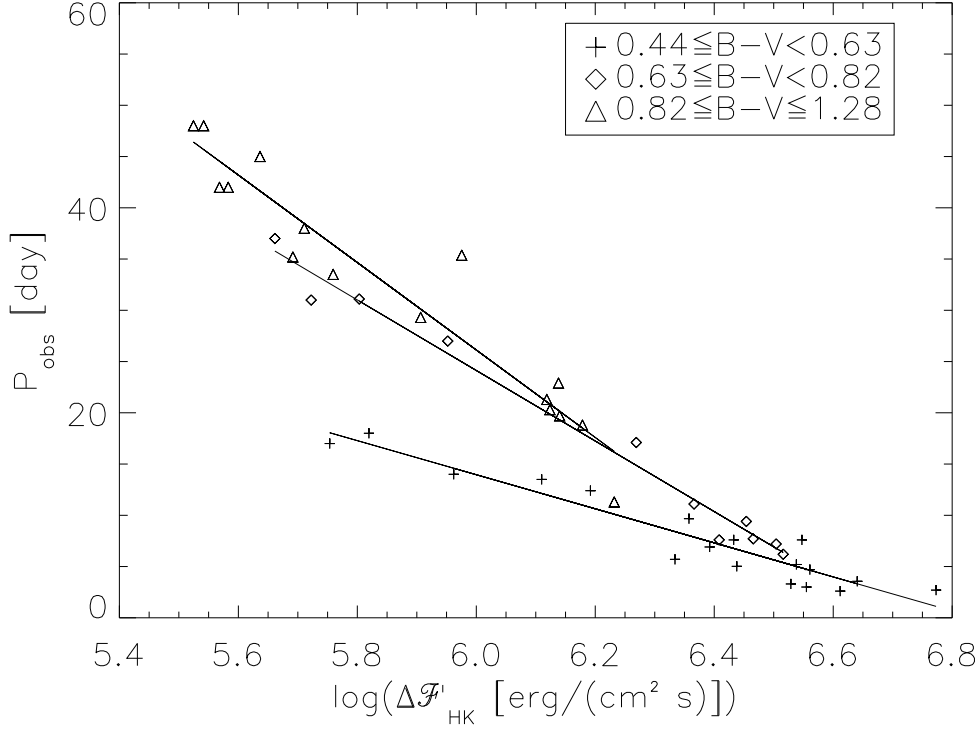
Figure 7.15: The rotation period vs. log $\Delta\mathcal{F}'_{\text{HK}}$ of main sequence stars with the solid line as fit

	$\sum$ of objects	r	$\mid t \mid$
$0.44 \leq B - V < 0.63$	18	-0.95	12.7
$0.63 \leq B - V < 0.82$	11	-0.99	23.2
$0.82 \leq B - V \leq 1.28$	16	-0.96	13.1

Table 7.4: Correlation coefficient of the trends in Fig. 7.15

The fits are given by the following equations:

$$P = \begin{cases} (113.7 \pm 8.4) - (16.6 \pm 1.3)\log(\Delta\mathcal{F}'_{\text{HK}}), & \text{for } 0.44 \leq \text{B} - \text{V} < 0.63 \\ (230.6 \pm 9.2) - (34.4 \pm 1.5)\log(\Delta\mathcal{F}'_{\text{HK}}), & \text{for } 0.63 \leq \text{B} - \text{V} < 0.82 \\ (282.1 \pm 19.2) - (42.7 \pm 3.3)\log(\Delta\mathcal{F}'_{\text{HK}}). & \text{for } 0.82 \leq \text{B} - \text{V} \leq 1.28 \end{cases} \quad (7.16)$$

The corresponding standard deviations of the residuals are:

$$\text{for } 0.44 \leq B - V < 0.63 = 1.5 \text{ day,}$$
$$\text{for } 0.63 \leq B - V < 0.82 = 1.5 \text{ day,}$$
$$\text{for } 0.82 \leq B - V \leq 1.28 = 3.2 \text{ day.}$$

The total standard deviation of the residuals for the three fits is:

$$\text{Standard deviation of the residuals} = 2.2 \text{ day.}$$

Finally, I compared the standard deviation of the residuals from these relations with the standard deviation of the residuals of the data of Noyes et al. (1984). The standard deviation of the residuals with the relation Eq. 7.16 is 2.2 and for the results by Noyes et al. (1984) 2.5.

7.7 Summary and Conclusion

The new photospheric flux corrections are an extension of the correction by Noyes et al. (1984). With the new relations, it is possible to calculate log R'_{HK} for subgiant and giant stars. For consistency, a new photospheric flux correction is also created for main sequence stars. The results of these corrections are compared with the results of the correction by Noyes et al. (1984). The results of the new correction are slightly different for active and non-active stars.

I also refitted the relation between R'_{HK} and the Rossby number. Here, I used a linear fit because I could show that the relation between R'_{HK} vs. Rossby number (Ro) is linear. The standard deviation of the residuals of the calculated periods with the new relation are slightly greater than the standard deviation of the residuals of the periods calculated by Noyes et al. (1984). This larger deviation is caused by the convective turnover time. I used the convective turnover time Eq. 7.12 derived by Noyes et al. (1984). In order to make the deviations smaller, the convective turnover time has to be re-determined.

To avoid the introduction of a further and very uncertain relationship for the convective turnover time, I created new empirically determined relationships between the excess flux of the Ca II H+K line and the rotation period of the star for main sequence stars. The results of these relations are slightly more precise than the periods calculated by Noyes et al. (1984).

In my investigation on log $\Delta\mathcal{F}'_{\text{HK}}$ and the rotation period of the stars, I found two general trends for main sequence stars depending on the colour index $B - V$ where $B - V = 0.63$ mag marks a border line. Furthermore, I investigated the influence of the stellar age on log $\Delta\mathcal{F}'_{\text{HK}}$ and the rotation period and found a transition range between young and old stars. In this transition range, the Vaughan-Preston gap is located. Finally, I can conclude that the new photospheric corrections are working very well. Therefore, these photospheric corrections are used for the rest of this work.

Chapter 8

Template candidates

To investigate the activity level of a star, one possible method is to determine the flux excess of activity sensitive lines with a template star. The problem is, one does not have always an appropriate spectrum of a template star. Therefore, one idea is to create a data base with inactive stars which is usable as template stars.

In this chapter, a definition of a template star is given and the selection criteria are described. Also, the first results of the search for template stars is presented. Here, I only check the line cores of the Ca II H+K lines whether a double peak structure can be seen.

8.1 Definition and selection of template star candidates

The definition for a template star is: **A template star is a non- or very weakly active star. In the Ca II K line, there is no or a very weak double peak structure and in the Ca II H line, no double peak structure exists. Furthermore, the flux of Ca II H+K lines is stable and does not show any short-time variability.** To check if a star is active or not, the Ca II H+K lines are used. These lines are the most activity sensitive lines in the optical. The characteristical double peak structure, as sign of activity, is easy to detect, also for low active stars.

To find template candidates, the S-index and $\log R'_{\mathrm{HK}}$ can be used. Here, one searches for small S-indices or small $\log R'_{\mathrm{HK}}$. Henry et al. (1996) defined a threshold of $\log R'_{\mathrm{HK}}$ for the activity state of stars and these are given as:

$$\begin{aligned}
\log R'_{\mathrm{HK}} &> -4.20, \text{ for very active stars} \\
-4.20 > \log R'_{\mathrm{HK}} &> -4.75, \text{ for active stars} \\
-4.75 > \log R'_{\mathrm{HK}} &> -5.10, \text{ for inactive stars} \\
-5.10 > \log R'_{\mathrm{HK}} &, \text{ for very inactive stars}
\end{aligned}$$

Using $\log R'_{\mathrm{HK}}$ is problematic because some stars are labelled as main sequence stars in the different catalogues, however these stars are subgiant stars as defined by the position in the H-R diagram. The $\log R'_{\mathrm{HK}}$ calculated by Noyes et al. (1984) is only defined for main sequence stars and so the value of $\log R'_{\mathrm{HK}}$ is too small. Another problem is that a star can show an emission peak in the Ca II H+K lines although the star is defined as inactive as defined by Henry et al. (1996). Such a star is unusable as template star.

Hence, I used mainly the S-index of the object to find possible template candidates.

Therefore, I collected the S-indices from different catalogues (e. g., Duncan et al. (1991); Wright et al. (2004)). Thereafter, the S-indices are sorted by luminosity class and by colour index $B - V$ and selected those objects with the smallest S-index for each luminosity class (giant, subgiant and main sequence star) and for $B - V$. Next, I checked if the object has been detected in X-rays because active stars are bright in X-ray. Finally, the rotation period P and the rotation velocity ($vsini$), respectively, are checked as only slow rotators are usable as templates.

Additionally, I observed flat active stars (see. Sect. 6.4.2) with a small S-index and non detected stars (see. Sect. 6.4.2) from the sample by Baliunas et al. (1995) and Hall et al. (2007), respectively, in order to check if these stars are usable as template stars. These stars are selected from the object list which was used to create the transformation equation form the S-index of the HRT to the Mount Wilson S-index.

8.2 Observed template star candidates

In Fig. 8.1 - 8.6, I present the first six observations to find template candidates. Therefore, I checked whether or not a double peak structure can be detected in the Ca II H+K lines of the spectra with the lowest noise in the these lines. Nevertheless, the line cores of Ca II H+K lines are somewhat noisy. This is a result from the relatively high dark noise of the CCD camera, see Sect. 4.2.2. To decrease the noise in the line core, the spectra are rebinned by a factor two. The rebinning does not lead to a loss of spectral resolution R because the $\Delta\lambda$ is dispersed to four pixel, where $\Delta\lambda = \lambda/R$.

For the individual objects, I present some basic information in Table 8.1. I calculated the

Object	$B - V$ [mag]	vmag [mag]	Dist [pc]	VMAG [mag]	Lum. class	T_{eff} [K]
HD32923	0.657 ± 0.012	4.91	15.9 ± 0.2	3.91 ± 0.03	IV	5726 ± 37
HD58855	0.470 ± 0.003	5.35	19.9 ± 0.3	3.86 ± 0.04	V	6399 ± 13
HD84737	0.619 ± 0.007	5.08	18.4 ± 0.3	3.75 ± 0.03	IV	5846 ± 23
HD89744	0.531 ± 0.003	5.73	39.0 ± 1.1	2.78 ± 0.06	IV	6156 ± 11
HD124570	0.537 ± 0.003	5.53	33.3 ± 0.8	2.92 ± 0.05	IV	6133 ± 11
HD142373	0.563 ± 0.014	4.60	15.9 ± 0.1	3.60 ± 0.02	IV	6038 ± 50

Table 8.1: The objects with their colour index $B - V$ [mag], visual magnitude vmag [mag], distance [pc], absolute magnitude VMAG [mag], luminosity class, effective temperature T_{eff} [K]

absolute magnitude and defined the luminosity class of the objects. Therefore, I used the distance [Plx] and the visual magnitude from the Hipparcos Main Catalogue (Perryman and ESA 1997). The colour index $B - V$ from the Hipparcos Main Catalogue is used to calculate effective temperatures with Eq. 6.13.

The S-index and the log R'_{HK} are determined for the objects to show the activity level of the star and are given in the Table 8.2.

In the following, I compare the S-indices from different catalogues with the measured S-index of the spectra which are presented here. Furthermore, I comment briefly on the Ca II H+K line spectra of the six template candidates. Additionally, I designate a rotational

Object	S	log R'_{HK}
HD32923	0.140 ± 0.005	$-5.15 \pm 0.09.$
HD58855	0.147 ± 0.005	$-5.12 \pm 0.10.$
HD84737	0.137 ± 0.005	$-5.19 \pm 0.10.$
HD89744	0.144 ± 0.006	$-5.15 \pm 0.11.$
HD124570	0.130 ± 0.006	$-5.44 \pm 0.21.$
HD142373	0.146 ± 0.006	$-5.11 \pm 0.12.$

Table 8.2: The objects with S-index S and the log R'_{HK}

velocity and a metallicity for each object. In order to decide if a star can be used as a template one has to take into account the rotational velocity. To compare different stars, their metallicities can influence the value of the flux excess.

HD32923 is also called 104 Tau. This star is one of the stars from the star sample which was used to create the transformation equation from S_{HRT} to S_{MWO}. It was selected from Hall et al. (2007). For this object, a long-term variability was not detected and the average S-index is $\langle S \rangle = 0.143$ (Hall et al. 2007). The S-index was also measured for this object by Wright et al. (2004) and by Gray et al. (2003) as $S = 0.155$ and $S = 0.142$, respectively. The here measured S-index (0.140 ± 0.006) is comparable with the values by Hall et al. (2007) and by Gray et al. (2003). The S-index by Wright et al. (2004) is significantly different from all other measurements.

HD32923 has a rotational velocity and metallicity of $vsini = (1.6 \pm 0.6)$ km/s (Glebocki and Stawikowski 2000) and $[Fe/H] = -0.22$ (Holmberg et al. 2009), respectively.

In Fig. 8.1, the Ca II H+K lines of HD32923 are shown. This spectrum was taken on

Figure 8.1: The Ca II H+K lines of HD32923 observed at Jan. 5 2009, the lower curve shows the original spectrum and the upper one is the rebinned spectrum (factor 2); left: Ca II K line with a S/N of 33 electrons/pixel in 1 Å bandpass; right: Ca II H line with a S/N of 40 electrons/pixel in 1 Å bandpass
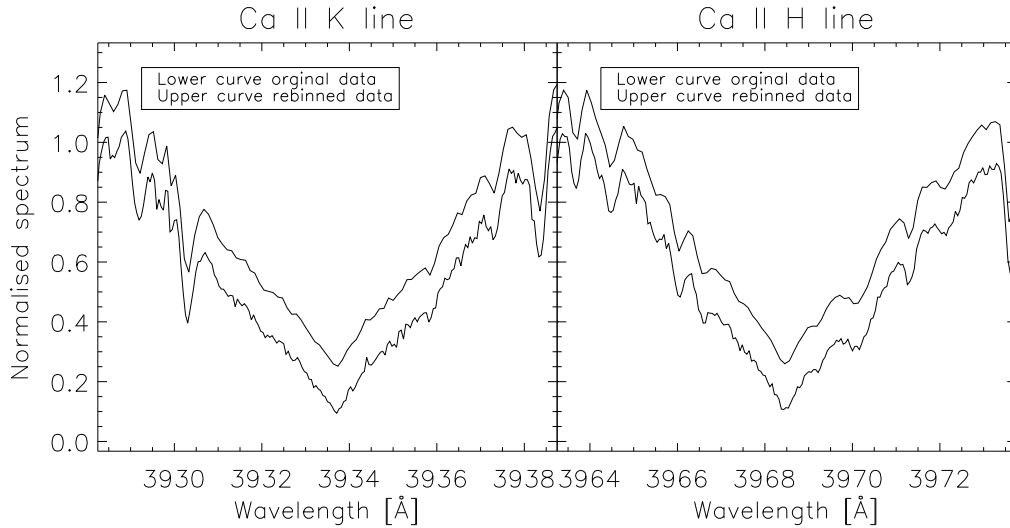
Figure 8.2: The Ca II H+K lines of HD58855 observed at Feb. 12 2009, the lower curve shows the original spectrum and the upper one is the rebinned spectrum (factor 2); left: Ca II K line with a S/N of 68 electrons/pixel in 1 Å bandpass; right: Ca II H line with a S/N of 81 electrons/pixel in 1 Å bandpass

Jan. 5 2009 with an exposure time of 3600 sec. In the rebinned spectrum, one can see a weak double peak structure in the Ca II K line whereas in the Ca II H line there is no such feature. I conclude that this spectrum shows a weak sign of activity.

HD58855 is also called 22 Lyn and was selected from Duncan et al. (1991). The total number of observation is 3 and the average S-index is $\langle S \rangle = (0.150 \pm 0.001)$ (Duncan et al. 1991). To compare this value with the S-index of this measurement (0.147 ± 0.005), both S-indices agree within the errors.

The rotational velocity and metallicity of this object are $vsini = 8.5$ km/s (Schröder et al. 2009) and $[Fe/H] = -0.28$ (Holmberg et al. 2009), respectively.

The spectral ranges of the Ca II H+K lines of HD58855 are shown in Fig. 8.2. This figure shows the co-added spectrum of 3 single observations on Feb. 12 2009. The total exposure time was 10800 sec. In the Ca II H+K lines (Fig. 8.2), no double peak structure can be seen.

It is also possible to calculate a rotation period and I obtained a value of $P = (16.4 \pm 11.5)$ day with Eq. 7.16. The large error is the result of the errors of the equation parameters. Without these parameter errors, I obtain an error of $\sigma = 1.6$ days.

This object does not show any activity signs in its spectrum (Fig. 8.2). Therefore, this object is a very good template candidate.

HD84737 is also called 15 LMi and was selected from Duncan et al. (1991). The total number of observations is one with a S-index of $S = 0.145$. The S-index was also determined by Wright et al. (2004) as $S = 0.130$ and by Gray et al. (2003) as $S = 0.140$. These three S-indices are clearly different. The S-index of this measurement is (0.137 ± 0.005). The object has a rotational velocity of $vsini = (2.8 \pm 0.8)$ km/s (Glebocki and Stawikowski 2000) and a metallicity of $[Fe/H] = 0.07$ (Holmberg et al. 2009).

The Ca II H+K lines of HD84737 are shown in Fig. 8.3. This spectrum is a co-added
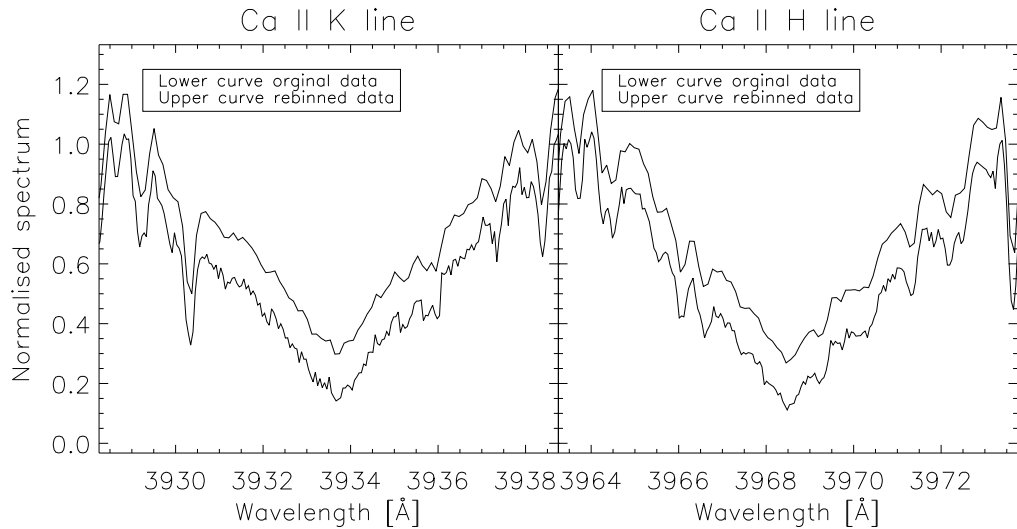
Figure 8.3: The Ca II H+K lines of HD84737 observed at Feb. 11 2009, the lower curve shows the original spectrum and the upper one is the rebinned spectrum (factor 2); left: Ca II K line with a S/N of 49 electrons/pixel in 1 Å bandpass; right: Ca II H line with a S/N of 57 electrons/pixel in 1 Å bandpass

spectrum of 2 single observations on Feb. 11 2009 with a total exposure time of 7200 sec. In the spectrum of the Ca II K line (Fig. 8.3), one sees on the left side of the line core a weak peak. Here, it is not definitely clear whether this peak is caused by activity or by dark noise. Though, because of the missing of a weak peak on the right side of the line core, one can assume that this peak is created by the dark noise. The latter assumption is possible because in the Ca II H line (Fig. 8.3), one does not see a double peak structure. This object is a good template candidate with a small log R'_{HK} even though the Ca II K line shows a peak.

HD89744 is labelled as flat active star in Baliunas et al. (1995) and is one of the stars which was used for S-index calibration (Sect. 6.4.2). The average S-index is $\langle S \rangle = 0.137$. The S-index in Wright et al. (2004) is $S = 0.158$ and in Gray et al. (2003) $S = 0.137$. The S-index for this measurement is ($S = 0.144 \pm 0.006$). The rotational velocity and metallicity of HD89737 are $vsini = 10$ km/s (Glebocki and Stawikowski 2000) and $[Fe/H] = 0.18$ sun (Holmberg et al. 2009), respectively. For this object, X-ray radiation was detected with a count rate of $(1.139 \pm 0.151) \cdot 10^{-2}$ ct/s (Second ROSAT PSPC Catalog 2000).
In Fig. 8.4, the Ca II H+K lines of HD89744 are shown. It is a co-added spectrum of 3 single observations on Dec. 29 2008. The total exposure time was 8100 sec.
The Ca II K line (Fig. 8.4) is too noisy to detect a peak structure. In the rebinned spectrum of the Ca II K line, it is also not possible to detect the double peak structure. On the other hand, one can see a very weak double peak structure in the Ca II H line. Therefore, I can conclude, it is possible that this object has a very low activity level.
HD124570 is also called 14 Boo and is one of the stars from the star sample which was used to perform the S-index calibration (Sect. 6.4.2). The average S-index is $\langle S \rangle = 0.133$ and the star is labelled as flat active star by Baliunas et al. (1995) and by Hall et al. (2007) as "not detected" with an average S-index of $\langle S \rangle = 0.134$. The S-index for this

Figure 8.4: The Ca II H+K lines of HD89744 observed at Dec. 29 2008, the lower curve shows the original spectrum and the upper one is the rebinned spectrum (factor 29; left: Ca II K line with a S/N of 34 electrons/pixel in 1 Å bandpass; right: Ca II H line with a S/N of 36 electrons/pixel in 1 Å bandpass
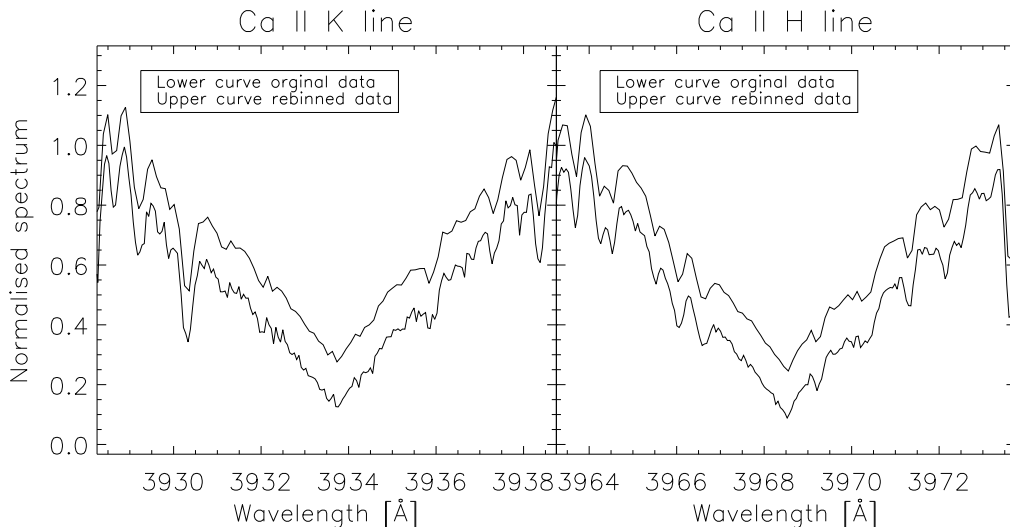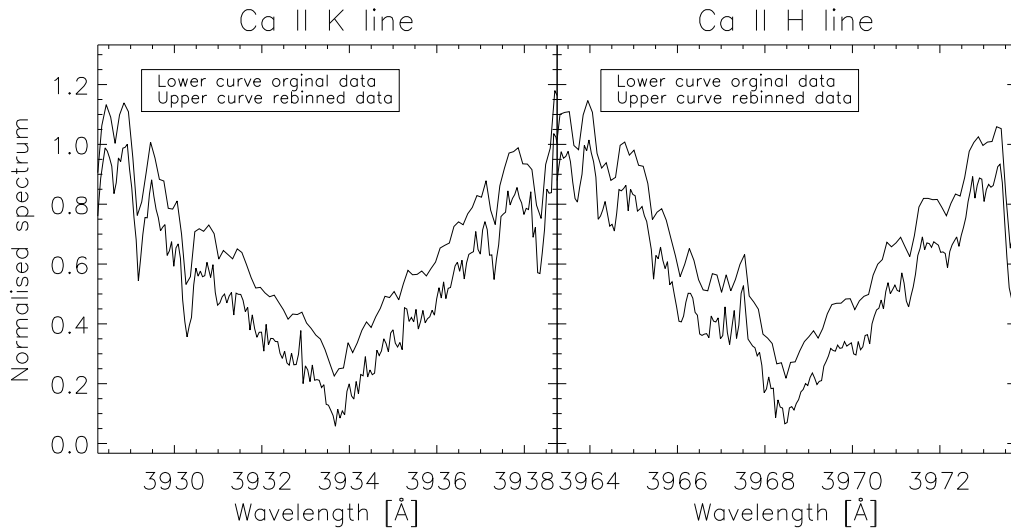

Figure 8.5: The Ca II H+K lines of HD124570 observed at Apr. 18 2009, the lower curve shows the original spectrum and the upper one is the rebinned spectrum (factor 2); left: Ca II K line with a S/N of 31 electrons/pixel in 1 Å bandpass; right: Ca II H line with a S/N of 37 electrons/pixel in 1 Å bandpass

measurement ($S = 0.130 \pm 0.006$) is, within the error, equal to the S-indices by Baliunas et al. (1995) and Hall et al. (2007). HD124570 has a rotational velocity and metallicity of $vsini = (5.6 \pm 1.0)$ km/s (Glebocki and Stawikowski 2000) and $[Fe/H] = 0.07$ (Holmberg
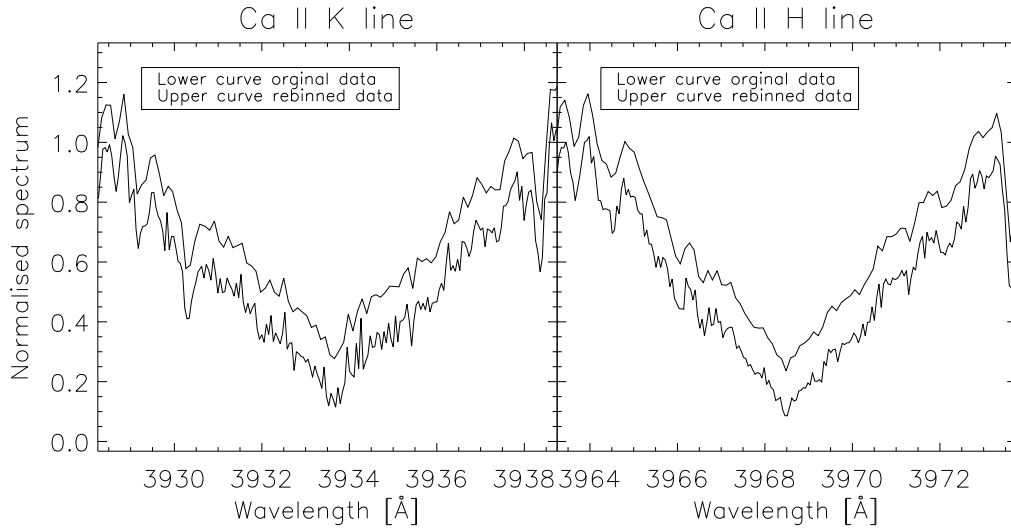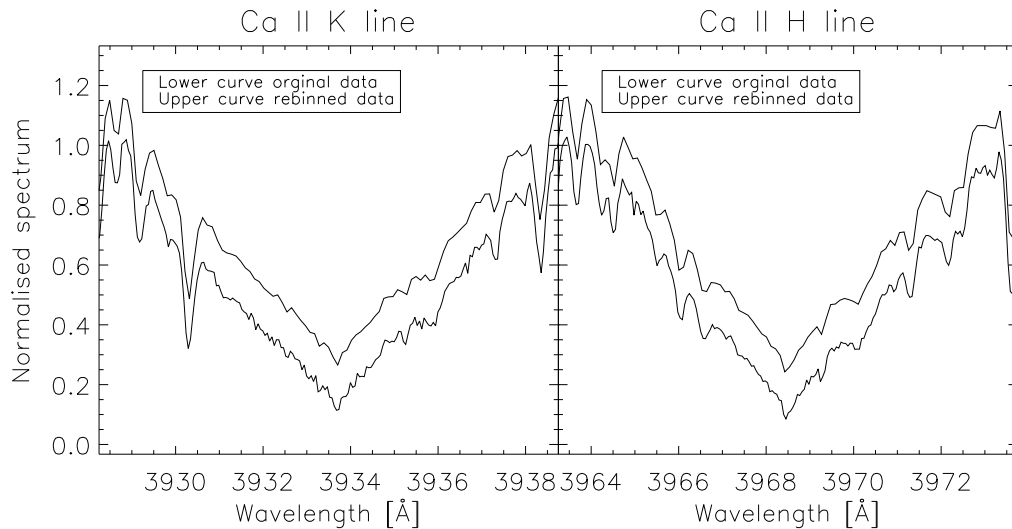
Figure 8.6: The Ca II H+K lines of HD142373 observed at Aug. 13 2009, the lower curve shows the original spectrum and the upper one is the rebinned spectrum (factor 2); left: Ca II K line with a S/N of 38 electrons/pixel in 1 Å bandpass; right: Ca II H line with a S/N of 42 electrons/pixel in 1 Å bandpass

et al. 2009), respectively.

The Ca II H+K lines of HD124570 are shown in Fig. 8.5. The spectrum of HD124570 is a co-added spectrum of 2 single observations on Apr. 18 2009. The total exposure time was 7200 sec.

The Ca II K line is too noisy to detect any feature. In the Ca II H line, one can clearly see a double peak structure in the rebinned spectrum.

It is also possible to compare the S-index with the S-index of HD89744 because these stars have a comparable colour index and evolutionary state. The S-index of HD89744 is greater than the S-index of HD124570 as is the average S-index, see Table 6.1. These objects have different rotational velocities and metallicities and these differences have an influence on the S-index. The issue is, how strong the influence on these differences at the S-index is. For this object, I come to the same conclusion as for HD89744. It is possible that this object has a very low activity level.

HD142373 is also called χ Her and part of the object list, which was used to perform the S-index calibration (Sect. 6.4.2). The average S-index is $\langle S \rangle = 0.147$ and labelled as flat active star by Baliunas et al. (1995). In Hall et al. (2007), this star is labelled as solar-activity variable without a S-index. Nevertheless, this star was listed in the list of template candidates on the basis of the small S-index and the label for long time variables in Baliunas et al. (1995). The average S-index by Baliunas et al. (1995) and the S-index for this measurement (0.146 ± 0.006) are equal. This object has rotational velocity and metallicity of $vsini = (2.40 \pm 0.80)$ km/s (Glebocki and Stawikowski 2000) and $[Fe/H] = -0.50$ (Holmberg et al. 2009), respectively. Furthermore, a faint X-ray radiation was detected with the ROSAT satellite. The count rate was $(4.93 \pm 1.53) \cdot 10^{-3}$ ct/s (Second ROSAT PSPC Catalog 2000). In Fig. 8.6, the spectra of the Ca II H+K lines are shown. This spectrum is a co-added spectrum of 2 single observations on Aug. 13 2009 with a total

exposure time of 3000 sec.

In the rebinned spectrum of the Ca II K line, one can clearly see a weak double peak structure and this is a sign of activity of this star. In the Ca II H line, no double peak can be seen in the spectrum. Hence, I can also conclude for this object, it is possible that this star has a very low activity level.

8.3   Summary

I can summarise that the best template candidate is HD58855. In the Ca II H+K lines spectra (Fig. 8.2), no double peak structure can be seen. HD84737 is also a good template candidate (Fig. 8.3). The peak in the Ca II K line is probably caused by dark noise. All other stars show a weak double peak structure in the Ca II K line or Ca II H line. So, one can assume that these stars are very low active. Whether these stars are usable as template stars will be shown in further investigations.

All objects have to be reobserved with the new CCD camera of the spectrograph (Sect. 4.2.2). With the new CCD camera, the dark problem in the spectra will be eliminated. After this, one can investigate the influence of the rotational velocity and metallicity on the S-index for HD89737 and HD124570.

Furthermore, the objects have to be checked for short-time variability because the short-time variability is also a criterion whether a object is usable as a template. For HD142373, this long-term monitoring was started and the first results of this monitoring is given in Sect. 9.6.

Chapter 9

Results of the first monitoring objects

The HRT is designed for long-term monitoring of active stars in order to obtain time series, e. g., of the S-indices, which allows to investigate activity variations in time. With a time series of the S-index, it is possible to determine the rotation period (Stimets and Giles 1980; Vaughan et al. 1981) and activity cycle (Baliunas et al. 1995) of a star. It is also possible to measure variations in time of the radial velocity.

Since Oct. 2008, scientific observations have been accomplished with the HRT and in this chapter, I present the first results of the long-term monitoring of some objects. Here, I show different time series of the S-index and try to measure a rotation period for the objects.

Therefore, I used only the S-indices with a total count rate of 10000 electrons in a 1Å bandpass centred in the line cores of the Ca II H+K lines. The error bars in the figures of the time series of the S-indices denote only the error of the S-index. They do not include the parameter errors of the transformation equation (Eq. 6.20) because these errors are the same for all data points. However, these errors are considered for the error information of the here presented individual average S-indices.

For HD79028 and HD120136, the radial velocities shifts and the corresponding periods are presented.

The colour indices, the visual magnitudes and distances of the star (without the Sun) are taken from the Hipparcos Main catalogue (Perryman and ESA 1997).

9.1 Period determination and statistical significance

To find a periodical signal in a time series, a Fourier analysis is used. For the investigation of time series, I used the Lomb-Sargle method (Scargle 1982; Horne and Baliunas 1986). With this method, one can investigate unevenly sampled time series and the noise in the data is also considered for the calculation of the power. This power ("scargle power") was normalised with the data noise. With this power, one can calculate the False Alarm Probability (FAP) and obtain the significance of each peak in the periodgram. Hence, the power of a peak corresponds to the probability that the data is periodically variable with this frequency. The FAP is calculated with (Horne and Baliunas 1986):

$$FAP \;\; = \;\; 1 - [1 - e^{-z}]^{N_i}, \tag{9.1}$$

where z is the power of the peak and the exponent N_i is the total number of independent frequencies. The latter is unknown because the time interval of the individual data points (Δt) are not identical. One can use an average Δt, but which method to determine the average Δt is unclear, e. g. mean, median (Scargle 1982). Horne and Baliunas (1986) performed simulations with different time samplings and found the following empirical relation:

$$N_i \;\; = \;\; -6.362 + 1.193 N_0 + 0.00098 N_0^2. \tag{9.2}$$

N_0 is the total number of data points. I used to investigate the time series with the IDL procedure *scargle.pro*[1].

The question is how strong the significance $P(z)$ of a peak has to be for a detection. Commonly accepted is a significance of **99.9**% and **FAP=0.01**, respectively, for a clear detection. The significance is given by:

$$P(z) \; [\%] \;\; = \;\; (1 - FAP) \; \cdot \; 100. \tag{9.3}$$

In this thesis, I used to fit the data with the period (1/frequency) where the peak of the corrsponding period has a significance of FAP<0.25, which corresponds to a significance of 75%. This is only performed to demonstrate the method. Periods below a significance of 99.9% are not surely detected.

The error of the period in the periodogram is caluculated (Baliunas et al. 1995):

$$\Delta P \;\; = \;\; \frac{3 \sigma_n P^2}{4 T A \sqrt{N}}, \tag{9.4}$$

where, σ_n is the standard deviation of the residuals after the substraction of the fit from the data, P the period, T the total length of the observation interval, A the amplitude of the signal and N the total number of data points.

9.2   The Sun

With the start of the scientific observations, the Sun has been observed since Oct 2008. For the Sun, it is possible to simultaneously observe the activity level with the S-index and the surface variations of the star. A visible sign of activity are sunspots which are created in the photosphere of the star. The S-index of the Sun and the relative sunspot number R (Sect. 2.2 and Eq. 2.1) both show the 11 year cycle, see Fig. 9.1 and 9.2. One sees that the activity level measured by the S-index and the numbers of sunspots are correlated. Only for the Sun, it is possible to study the depency of surface variations on the S-index. Therefore, it is interesting to monitor the Sun.

With the end of the 23rd solar cycle, the Sun showed very few sunspots. Hence, it is possible to show the strength of the variation of the S-index for days without sunspots. Furthermore, one can check the line profile of the Ca II H+K lines to see how clearly the double structure in the Ca II H+K lines can be recognised in the phase of relative inactivity, i. e. at spotless days.

To take a solar spectrum with the HRT, two methods were used. The first method was to take a lunar spectrum. Here, one uses the Moon as a mirror reflecting the sunlight. The
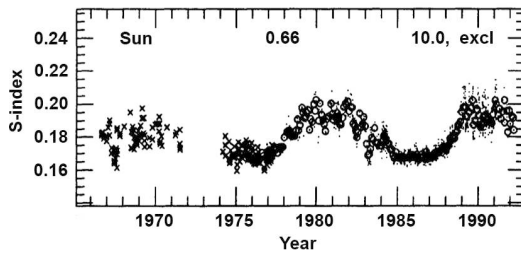
---

[1]Download from: http://astro.uni-tuebingen.de/software/idl/aitlib/timing/scargle.html

Figure 9.1: S-index time-series of the Sun (Baliunas et al. 1995)
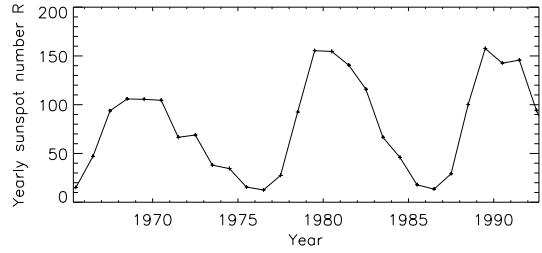
Figure 9.2: Yearly sunspot numbers from 1966 to 1992 (http://sidc.oma.be/sunspot-data/)

second method was to take a spectrum of the day sky in the zenith (day spectrum). Here, the scattering light of the Sun was used. In Fig. 9.3, the Ca II K line of a lunar spectrum and the day time spectrum is shown. In the left plot, one sees the difference between both spectra. This difference is caused by the additional continuum which is created by Rayleigh[2] and Mie[3] scattering. At the following, these types of scattering are described briefly:

Rayleigh scattering: The light is scattered by particles that are small compared to the wavelength (e. g., molecule). The intensity of the scattered light is $\sim 1/\lambda^4$. The blue light is scattered more strongly than red light and, therefore, the sky appears to be blue (Eichler et al. 2004).

Mie scattering: The light is scattered by particles for which the diameter is $d \gtrsim \lambda$ (e. g., dust, water droplets). If the diameter of these particles is $d \gg \lambda$, e. g. clouds, then the wavelength is no longer depending on the diameter of the particles. This explains the white colour of the clouds. (Eichler et al. 2004; Meschede 2006).

This additional continuum has to be eliminated because it leads to a larger S-index. The larger S-index is caused by the higher flux in the line cores of the Ca II H+K lines in the day spectrum. This continuum correction is performed with the following method: The spectrum is compared to a lunar spectrum without this effect in the range from 3850 Å to 4050 Å. The spectra are continuum-normalised such that one can compare the individual spectral lines. The difference in the line cores is created by Rayleigh and Mie scattering. This effect is seen clearest at deep lines because here the additional continuum has the largest influence. With the assumption that the difference in the line cores of deep lines equals the additional continuum, it is possible to determine this continuum. To do this, I used the lines which are given in Table A.8. To obtain the difference between the lines of the day light spectrum and the lunar spectrum, I interpolated the intensity in the line cores and determined the difference. Next, the difference of the lines is fitted depending on the wavelength. This continuum is subtracted from the day light spectrum and, thereafter, the spectrum is continuum-normalised. Finally, the day light spectrum is normalised to the blaze-normalised lunar spectrum to determine the S-index. In Fig. 9.3, the Ca II K line is shown before and after this correction. In the left plot, one clearly sees the increased line core of the day spectrum. In the right plot, this shift in the line is eliminated.

---

[2] John William Strutt, 3rd Baron Rayleigh, English physicist 1842-1919
[3] Gustav Adolf Feodor Wilhelm Ludwig Mie, German physicist 1869-1957
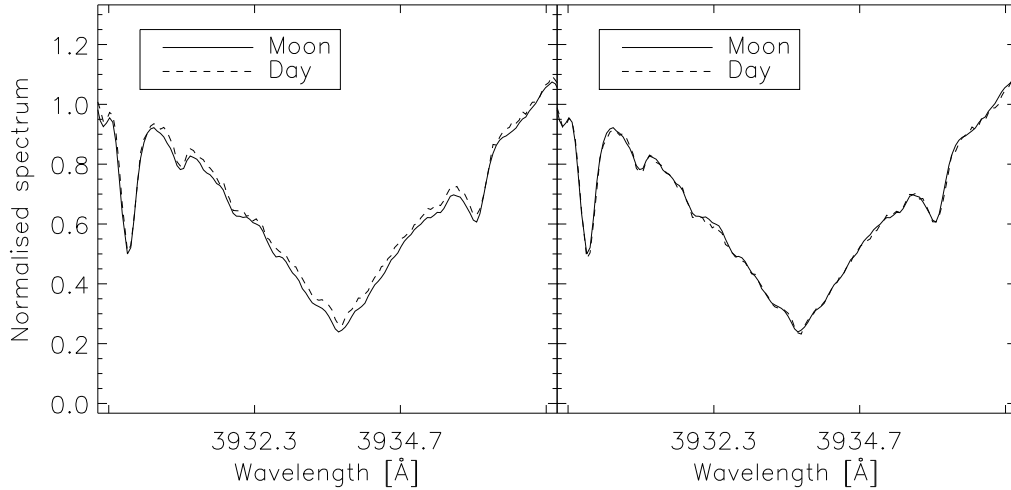
Figure 9.3: The Ca II K of the reference lunar spectrum and solar day time spectrum, left: without the continuum correction, right with the continuum correction

After this corretion, it is possible to determine the solar S-index. In the case of solar spectra, it is possible to use the statistical signal-to-noise in the 1 Å bandpass in the line core as a measurement error for the S-index because the influence of the dark noise in the line core can be ignored.

In Fig. 9.4a, the time series of the S-index from Oct. 2008 until Jul. 2009 observed with the HRT is shown. The data points are labelled with an asterisk and plus sign for day with and without a sunspot number, respectively. Additionally, two solar spectra were taken with help the of the Moon. The corresponding S-indices are plotted as cross signs in Fig. 9.4a. These values are important in order to check the method to eliminate the additional continuum in the day spectra. One sees that the S-indices of the lunar spectra are not different from the general trend and this shows that the method to eliminate the additional continuum is feasible. Furthermore, I checked for the day of the Moon observation whether a sunspot number exists. For the first Moon observation, the Sun has no sunspot number whereas the second Moon observation has a relative sunspot number of $R = 7$ (http://sidc.oma.be/sunspot-data/).

In Fig. 9.4a, one sees that the general trend of the S-index is constant in time. For the average S-index and the corresponding log R'_{HK}, I obtain the values:

$$\langle S \rangle = (0.155 \pm 0.004)$$
$$\log R'_{HK} = (-5.04 \pm 0.06).$$

This average S-index is very small, however, since 2008, the Sun is in a relatively inactive phase and showed sunspots only rarely. In Fig. 9.4b, the daily sunspot numbers are shown for the days of a Sun observation. The average ralative sunspot number of all sunspot numbers in the time range from Oct. 2008 to Jul. 2009 is $\langle R \rangle = (2.2 \pm 0.2)$.

The S-indices vary around the average S-index ($\langle S \rangle = (0.155 \pm 0.004)$) (Fig. 9.4a) for the Sun observations. The minimal and the maximal S-indices are $S = (0.151 \pm 0.004)$ and $S = (0.158 \pm 0.004)$, respectively. One can also see that the variations of the S-indices for
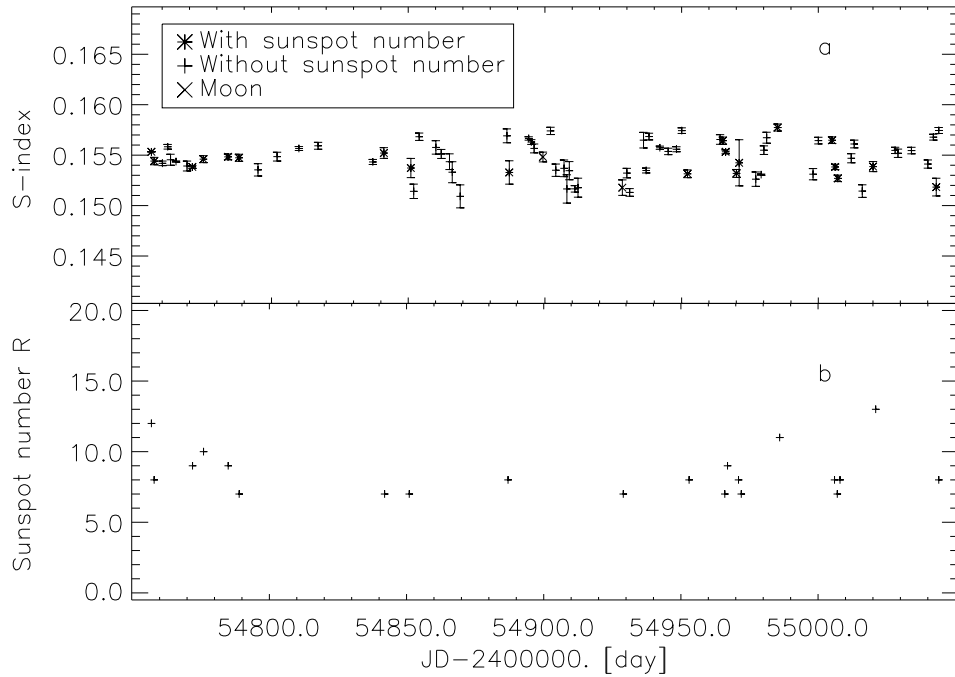
Figure 9.4: a: S-index time series of the Sun; b: Sunspot number R for the day of Sun observation

a day spectra with a sunspot number are not greater than the S-indices for day spectra with sunspot number zero. The average S-index and standard deviation of the S-indices without and with a sunspot number are given in Table 9.1. Hence, the sunspots during this observation time have not a significant influence on the average S-index. The variations

	R=0	R>0
S-index	0.155 ± 0.005	0.154 ± 0.004
Standard deviation	0.0018	0.0015
Number of data points	54	21

Table 9.1: The average S-indices and the standard derivation for the values without and

in the S-indices have two reasons. The main reason is the accuracy of the method to eliminate the additional continuum. To check how strong this influence is and to control the accuracy of the continuum elimination in the day spectra, it is important that lunar spectra are taken. Another reason is that the flux in the Ca II H+K lines is always slightly variable because the magnetic field and the chromosphere also are always slightly variable. To investigate this effect, only the lunar spectra are usable. This is another reason why the Moon spectra are taken.

Furthermore, I investigated the time series of the S-index with a Fourier analysis, see Sect. 9.1, if they are periodic. In Fig. 9.5, the periodogram of the S-index is shown. In the periodogram, a peak with a significance of FAP=0.05 is shown at the frequency of
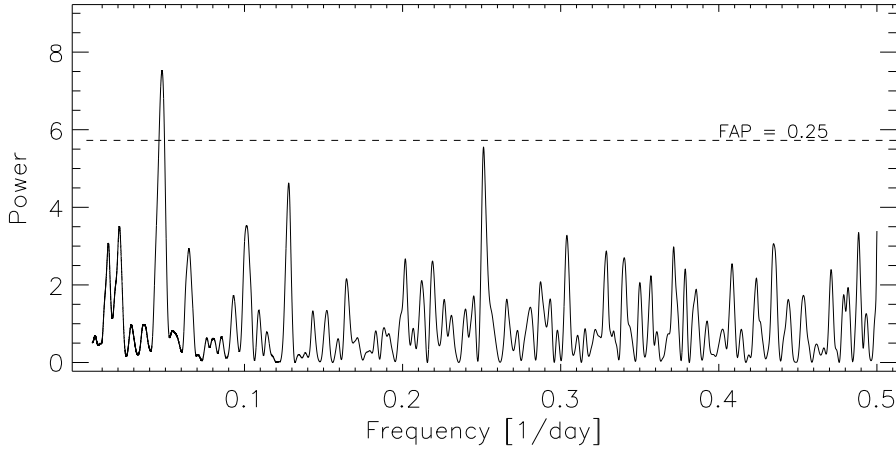
Figure 9.5: a: Periodogram of the time series of the S-index of the Sun

$\nu = 0.04786$ 1/day. This frequency corresponds to a period of:

$$P \quad = \quad 20.9 \text{ day}.$$

This period is different from the synodic rotation period of the Sun ($P = 27$ day (Allen 1976)). I had not expected to find the rotation period of the Sun in the data because most of the time the Sun was spotless. A possible reason for this peak is a superposition of the stellar rotation and the evolution of active regions on the Sun. This effect is discussed in detail by Hempelmann and Donahue (1997); Hempelmann (2002, 2003).

To verify if this period is likely to be real and to determine the amplitude of the variation in the data, I performed a least square fit with the following sine function:

$$data \quad = \quad A \cdot \sin(\frac{2\pi}{P} + \varphi), \tag{9.5}$$

where, *data* are the measured S-indices, A the amplitude and φ the zero phase. I obtained for the amplitude:

$$A \quad = \quad (0.5 \pm 6.7) \cdot 10^{-4}.$$

The amplitude of the variation is consistent with zero. Hence, a periodic variation is too small compared to the data noise.

Finally, I checked whether or not a double peak structure can be seen in the Ca II H+K lines. Therefore, I used a lunar spectrum because with lunar spectra, one does not have the problem of the additional continuum elimination. Therefore, the S-indices can not have an error caused by the continuum elimination. In Fig. 9.6, the co-added spectra of the Ca II H+K lines of the first Moon observation on Mar. 8 2009 are shown. For this day, no sunspot was registered. The average S-index of the single spectra is $\langle S \rangle = (0.155 \pm 0.004)$. In the left plot of Fig. 9.6, the Ca II K line is shown. One can clearly see a weak double structure in the line core. The Ca II H line is shown in the right plot of Fig. 9.6. In this line core one does not see a double structure.
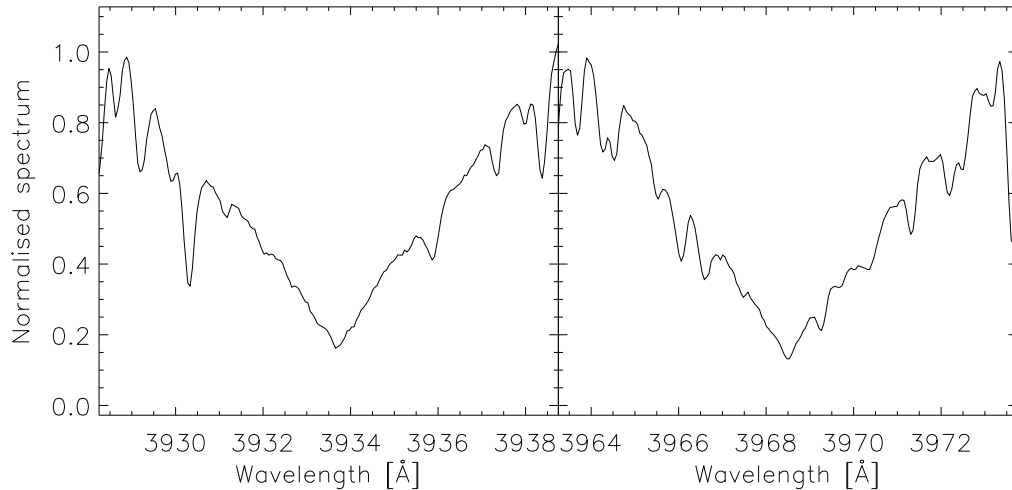
Figure 9.6: The Ca II H+K lines of the co-added spectrum of 5 single Moon observations on Mar. 8 2009; left: Ca II K line with a S/N of 69 electrons/pixel in 1 Å bandpass; right: Ca II H line with a S/N of 81 electrons/pixel in 1 Å bandpass

I can summarise that for the long-term monitoring, the day spectra taken with the scattering sunlight are usable whereas the scattering in the data is relatively high. From Oct. 2008 until Jul. 2009, the Sun was constant in activity. The activity level of the Sun for this time range was very low. This is consistent with the number of sunspots in this time range. In spite of the relative inactivity and without sunspots, a double peak structure is detected in the line core of the Ca II K line. Here, the magnetic field in the chromosphere is not high enough to create sunspots but high enough to generate an excess flux which is responsible for the double peak feature in the Ca II K line. The question is, how strong is the variability in the S-index in the times without sunspots? This issue can only be answered with further Moon observations. Furthermore, this has an influence on the template search. It is the question whether objects with a faint double peak feature in the Ca II K line and not in the Ca II H line are usable as template. Additionally, one has to check whether the time series of the S-index is short-time variable or not.

9.3 HD79028

HD79028 is also called 16 UMa. Determining the S-index, I found a strong variation in the radial velocity. In the Simbad catalogue, this star is labelled as a spectroscopic binary. Abt and Levy (1976) found a radial velocity period of $P = 16.2397$ day. To detect the radial velocity period and to measure the S-index, this star was monitored.

Before I present the results, some basic information about this star is given. The object has a colour index of $B - V = (0.605 \pm 0.003)$ mag. The effective temperature is calculated with Eq. 6.13 and I obtained $T_{eff} = (5893 \pm 10)$ K. The distance and the visual magnitude is (19.56 ± 0.28) pc and 5.18 mag, respectively. With these values, I obtained an absolute magnitude of (3.72 ± 0.03) mag. With the colour index and the absolute magnitude, I obtained the position in the H-R diagram and defined this star to be a subgiant.
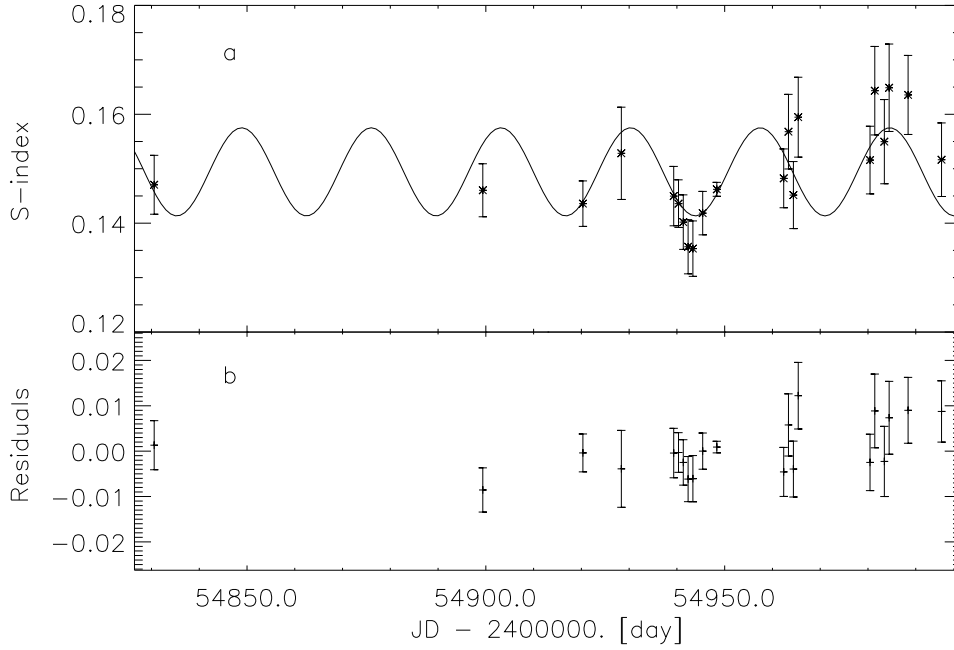
Figure 9.7: a: Time series of the S-index of HD79028 with the sine fit; b: Residuals of the sine fit

It was observed on 33 nights with an exposure time of 3000 sec until Apr. 26 2009 and thereafter with an exposure time of 2400 sec. For the radial velocity measurements, all night were used whereas only 21 nights used for the S-index time series. The reason is that the noise in the Ca II H+K lines in some spectra are too high and, thus, not usable to determine the S-index. First, I present the time series of the S-index and, then, the radial velocity curve and the radial velocity period of HD79028.

9.3.1 S-index

In Fig. 9.7, the S-index vs. time is shown. For the average S-index and $\log R'_{HK}$, I obtained:

$$
\begin{aligned}
\langle S \rangle &= (0.149 \pm 0.008) \\
\log R'_{HK} &= (-5.07 \pm 0.10).
\end{aligned}
$$

The standard deviation of the S-indices is 0.009. The average S-index by Hall (private communication) and Gray et al. (2003) is S = 0.137 and S=0.146, respectively.
A rotation period in the unit of days can be estimated with:

$$
\frac{P}{sini}[\text{day}] = \frac{2\pi R}{vsini \cdot 86400.0}, \tag{9.6}
$$

where R is the radius of the star and *vsini* the rotation velocity. With the factor 86400.0, the unit of the period is converted from sec into day. This period is only a lower limit because the inclination of the star is unknown. Furthermore, this period is dependent
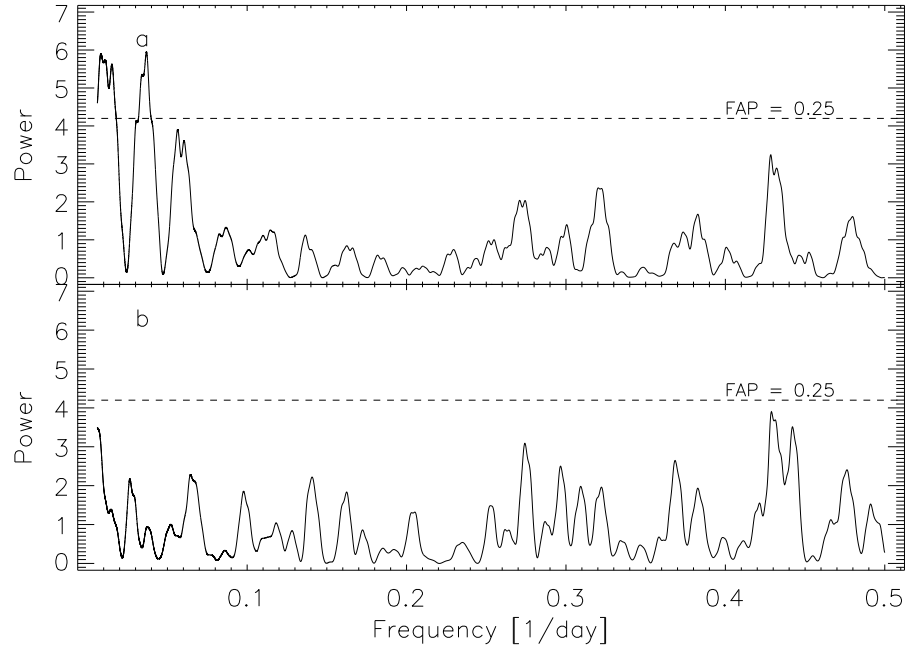
Figure 9.8: a: Periodogram of the time series of the S-index of HD79028; b: Periodgram of the residuals

on the values of the radius and the rotation velocity, which are used. With the radius $logR = (0.17 \pm 0.02) \ R_{\odot}$ (Allende Prieto and Lambert 1999) and the $vsini = 6.1$ km/s (Schröder et al. 2009), I obtained a period of:

$$\frac{P}{sini} \ = \ (12.3 \pm 0.6) \ \text{day}.$$

The time series of the S-index is investigated with a Fourier analysis, see Sect. 9.1 if the S-index variation periodic. In Fig. 9.8a, the periodogram of the S-index is shown. In the periodogram, two significant peaks are shown at the frequencies $\nu = 0.009$ 1/day and $\nu = 0.03685$ 1/day. The first frequency is probably not real due to the data sample. The second frequency corresponds a period of:

$$P \ = \ (27.1 \pm 0.5) \ \text{day}.$$

This peak has a FAP of 0.05. With this period, I fitted the data with the sine function 9.5 to determine the amplitude of the variation and to check this period. I obtained the following values for the amplitude and zero phase:

$$A \ = \ (0.008 \pm 0.002)$$
$$\varphi \ = \ (68.2 \pm 8.6)^{\circ}.$$

In Fig. 9.7a, the solid line represents this fit, which supports the assumption that the period is real. This fit has a reduced χ^2 of:

$$\chi^2 \ = \ 0.90.$$

The residuals of the fit are checked if the periodic variation are eliminated. In Fig. 9.8b, the periodogram of the residuals of the sine fit is shown. One sees that the peak for the period disappeared. The residuals of the fit are shown in Fig. 9.7b and the standard deviation of the residuals is 0.006.

Although the fit with the period of $P = 27.1$ day is quite good, the number of data points and the data sampling are not very good. If one compares this period to the period calculated with Eq. 9.6, then these periods are strongly different whereas the fit period is greater than the calculated period. It is necessary to observe this object further to verify this result because the significance is not high enough.

9.3.2   Radial velocity period

The radial velocity shift of this object is determined via cross correlation with a synthetic spectrum. The synthetic spectrum was calculated for photospheric flux correction of subgiant stars with the average $B - V = 0.6$ mag (Sect. 7.3). The radial velocity shift was determined for different wavelength ranges in the spectrum. The individual wavelength ranges are given in Table A.9. Finally, the radial velocity shift of each night is averaged and the corresponding error was calculated. The average error of the individual measurements was 0.59 ± 0.07 km/s. I obtained the average radial velocity shift using all radial velocity data as:

$$\langle RV \rangle \quad = \quad (-16.1 \pm 4.6) \text{ km/s.}$$

The standard deviation of the radial velocity shifts is 24.8 km/s. In Fig. 9.9a, the radial velocity shift vs. time is shown. One sees very well the periodic variations in the radial velocity. To determine the period of the radial velocity, a Fourier analysis was performed. Therefore, I used the same method as in Sect. 9.3.1.

In Fig. 9.10, the periodogram of the radial velocity is shown. A significant peak is detected at the frequency of $\nu = 0.06152$ 1/day and this corresponds to a period of:

$$P \quad = \quad 16.25 \text{ day.}$$

This period is consistent with the period by Abt and Levy (1976) ($P = 16.2397$ days). This peak has a FAP of $5.6 \cdot 10^{-6}$. Based on this period, the orbial parameters are calculated[4] via a χ^2 minimisation. The calculated orbital parameter are P the period, K the orbital velocity amplitude, V the barycentric velocity, e the orbital eccentricity, ω the longitude of perihelion, τ the zero point of the orbit. The results and the reference values by Abt and Levy (1976) are given in Table 9.2. In Fig. 9.9a, the solid line represents the sine fit. The fit has a reduced χ^2 of:

$$\chi^2 \quad = \quad 1.4.$$

In the residuals of the fit, see Fig. 9.9b, the strong variations are eliminated. Furthermore, the residuals are checked to detect a periodic signal. In Fig. 9.10b, the periodogram of the residuals shows that the peak for the period of $P = 16.25$ day has disappeared. The standard deviation of the residuals is 0.689 km/s. In Fig. 9.11, the radial velocity shift vs. phase is shown and the solid line represents one phase.

---

[4]Matlab procedure written by M. Esposito
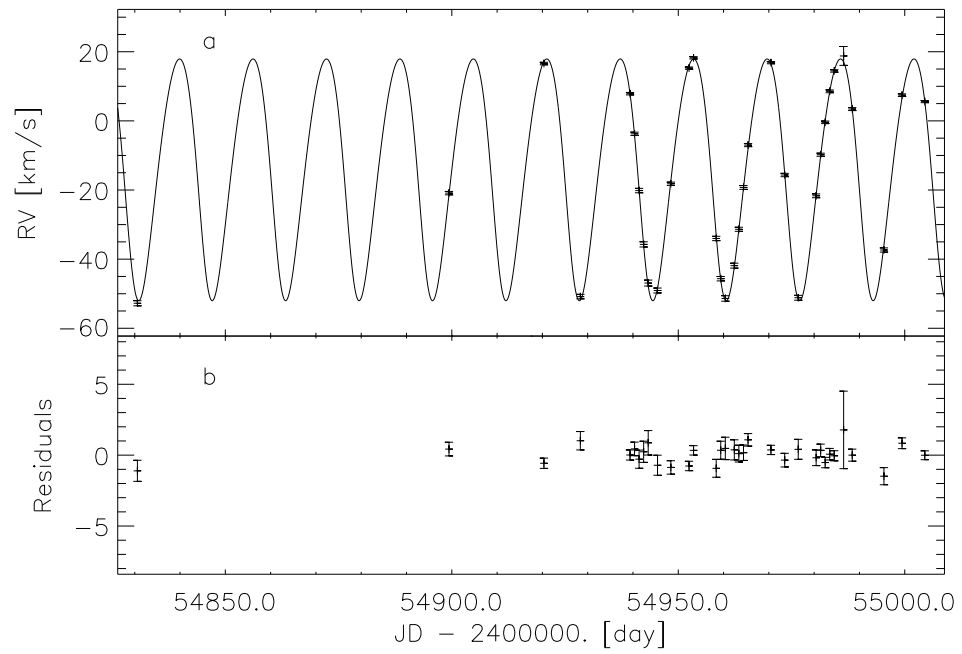
Figure 9.9: a: Radial velocity shifts of HD79028 with the Keplerian fit; b: Residuals of the fit
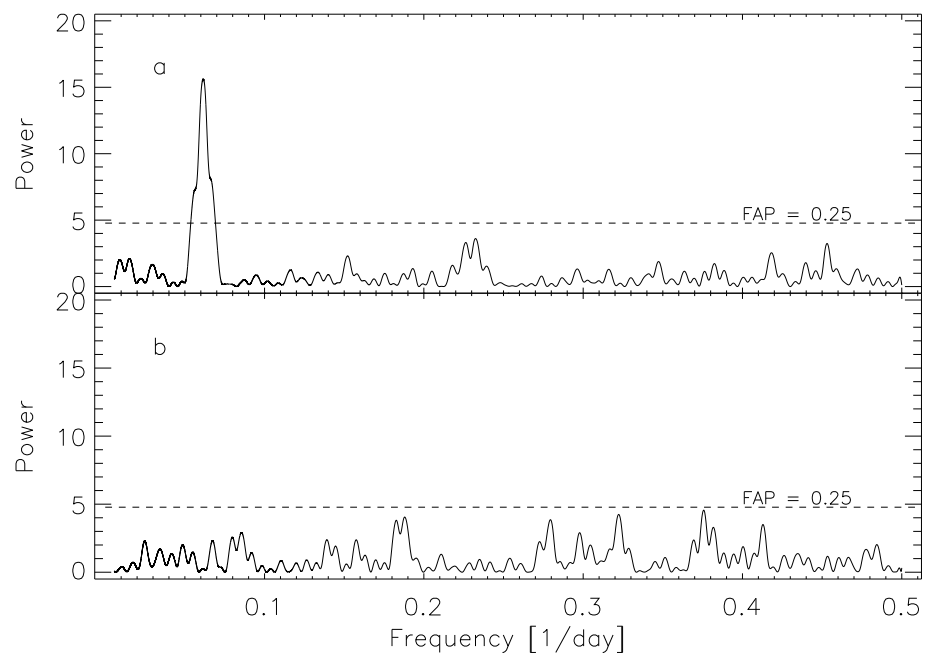
Figure 9.10: a: Periodogram of the radial velocity shifts of HD79028; b: Periodogram of the residuals
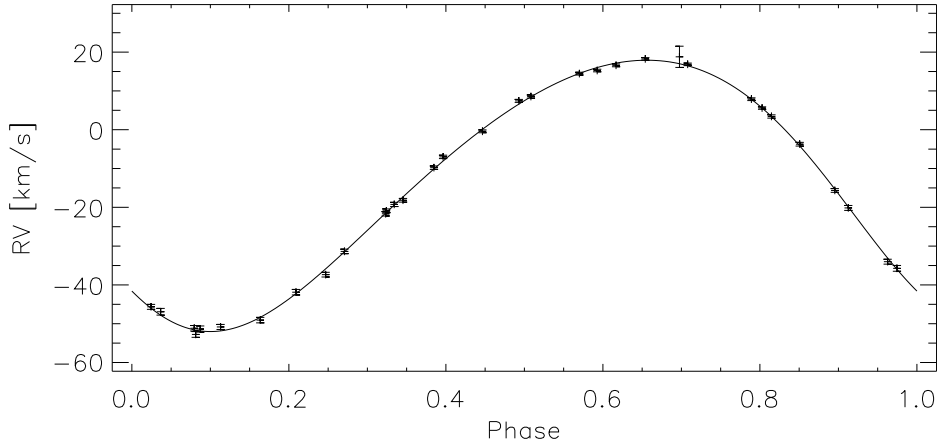
Figure 9.11: Phase plot of the radial velocity shifts of HD79028

Orbital parameter	this work	Abt and Levy (1976)
P [day]	(16.215±0.006)	16.2397
K [km/s]	(34.9±0.1)	35.3
V [km/s]	(-14.03±0.09)	-14.6
e	(0.123±0.003)	0.09
ω [°]	(134.6±2.1)	143.
τ [JD - 2400000.]	(54796.8±0.1)	23048.47

Table 9.2: The calculated orbital parameter and the parameter calculated by Abt and Levy (1976)

9.4 HD120136

Another name of HD120136 is τ Boo. This star is a very interesting object. It is a young main sequence star with a planet. The orbital period P_{orb} of the planet and the rotation period of the star P_{rot} are known. The orbital period is $P_{orb} = 3.31$ day and was found by Butler et al. (1997) via radial velocity measurements. The rotation period of the star is $P_{rot} = 3.2$ day and was measured by Henry et al. (2000) via photometric variations. Another measurement of the rotation period of the star is $P_{rot} = (3.3 \pm 0.5)$ day, Baliunas et al. (1997), which was obtained via variations in the S-index. Both periods are so slightly different that it is possible that the rotation velocity of the star and the orbital velocity of the planet are synchronised (Shkolnik et al. 2008). This star is a good candidate to investigate a possible star-planet interaction (SPI). Furthermore, this star is a good object to check the performance of the telescope. It is possible to check whether the period of the radial velocity shift and the rotation period can be detected. In the following, some object properties are given.

The colour index of HD120136 is $B - V = (0.508 \pm 0.001)$ mag. With this colour index, I obtained an effective temperature of $T_{eff} = (6245 \pm 4)$ K with Eq. 6.13. The error of the
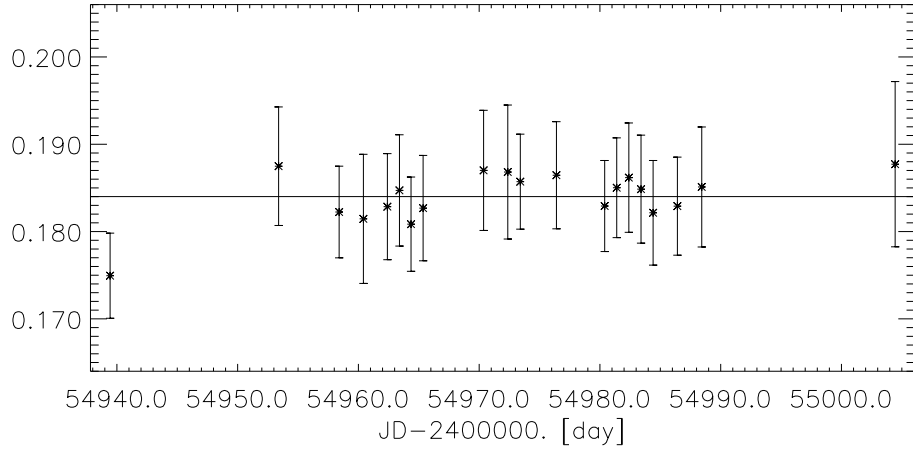
Figure 9.12: Time series of the S-index of HD120136 with the sine fit

effective temperature is very small and caused only by the small error of the colour index. The distance and the visual magnitude is (15.60 ± 0.17) pc and 5.18 mag, respectively. For the absolute magnitude, I obtained (3.53 ± 0.02) mag. Hence, I could determine the position in the H-R diagram. This star is located in the area of main sequence stars. The object was observed on 22 nights with 20 nights being usable for the time series analysis of the S-index. The exposure time was 1800 sec in all nights. In the following, I present the time series of HD120136 and after this the radial velocity shift investigation.

9.4.1 S-index

In Fig. 9.12a, the S-index vs. time is shown. For the average S-index and log R'_{HK}, I obtained:

$$\begin{aligned} \langle S \rangle &= (0.184 \pm 0.008) \\ \log R^{\cdot}_{\mathrm{HK}} &= (-4.74 \pm 0.06). \end{aligned}$$

The standard deviation of the S-indices is 0.003. Before I investigated the time series of the S-index to find a periodic variation, I estimated the period with the Eq. 9.6 and I obtained:

$$\frac{P}{sini} = (4.8 \pm 0.5) \text{ day}.$$

For the estimation of the period, I used $logR = (0.15 \pm 0.02) R_{\odot}$ (Allende Prieto and Lambert 1999) and $vsini = (14.80 \pm 0.80)$ km/s (Glebocki and Stawikowski 2000). HD120136 was defined as main sequence star so that with the Eq. 7.16, the rotation period can be estimated but in this case, it is not possible. The reason is, HD120136 is located in the H-R diagram in the transition region between the subgiants and main sequence stars, see Sect. 7.6.2. Hence, this star is not a pure main sequence star. To find a period in the time series of the S-index of HD120136, I performed a Fourier
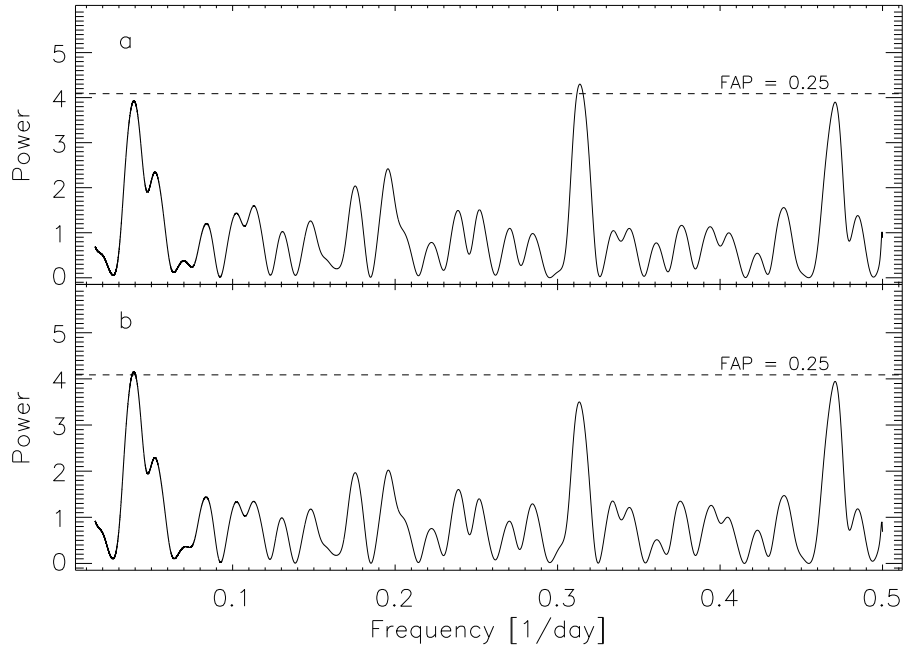
Figure 9.13: a: Periodogram of the time series of the S-index of HD120136; b: Periodogram of the residuals

analysis, see Sect. 9.1. The periodogram of the Fourier analysis is shown in Fig. 9.13a. In the periodogram, three significant peaks at the frequencies $\nu = 0.03923$, $\nu = 0.31369$ and $\nu = 0.47095$ are seen. The peak for the frequency $\nu = 0.31369$ has the significance of 78% and the other two peaks have only a significance of $\approx 70\%$. For these two peaks, the significance is smaller then the limit of 75%. The frequency of $\nu = 0.31369$ corresponds to a period of:

$$P \quad = \quad 3.19 \text{ day}.$$

This period is equal to the known rotation period of $P_{rot} = 3.2$ day by Henry et al. (2000). To check this period, I fitted the data with sine fit, see Eq. 9.5. Thereafter, I checked the residuals of this fit whether or not a peak at the corresponding frequency can be found. In Fig. 9.13b, the periodogram is shown. One sees that the peak at the frequency $\nu = 0.31369$ is smaller. The two other peaks can be seen clearly. For the amplitude, I obtained:

$$A \quad = \quad 0.0006 \pm 0.0020.$$

The error of this amplitude is greater than the amplitude and so, the amplitude is consistent with zero. The reason is that the data noise and the data error in the S-index time series are too strong. Furthermore, the significance of the peak is only 78%. Nevertheless, the highest peak is located at the known period. The period calculated with Eq. 9.6 is larger than the known period. It is unclear how precise the radius and the vsini of HD120136 are because the known rotation period of the star was measured with two different methods.
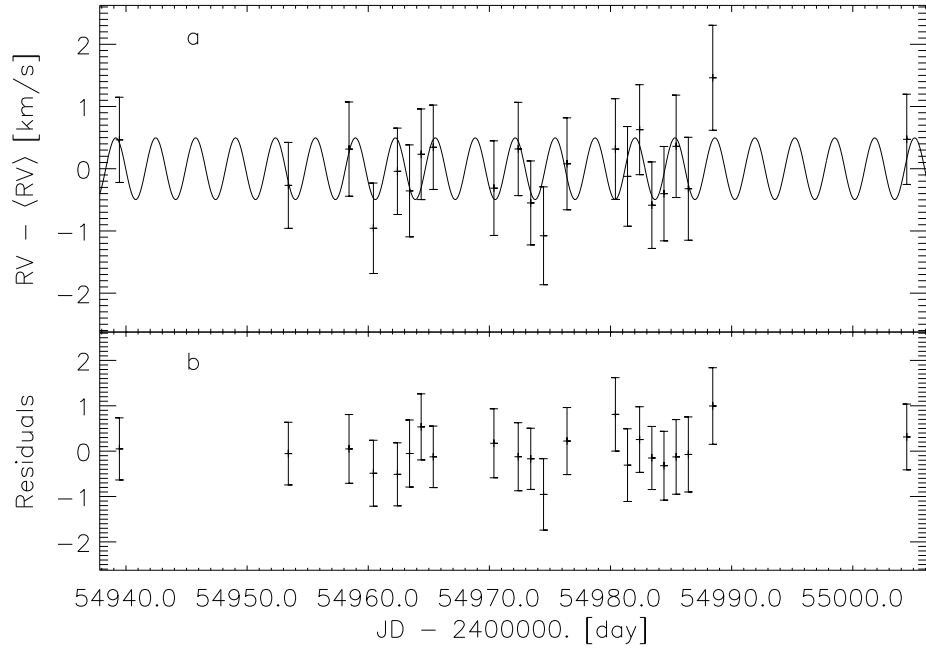
Figure 9.14: a: Time series of the variations of the radial velocity shifts of HD120136 with the sine fit; b: Residuals of the sine fit

9.4.2 Radial velocity period

In this section, I present the radial velocity shifts of HD120136. They are caused by the planet of HD120136. The planet was found by Butler et al. (1997). They had measured a period of $P = 3.3128 \pm 0.0002$ days and a velocity amplitude of $K = 0.469 \pm 0.005$ km/s. To determine the radial velocity shifts, I used the method which was described in Sect. 9.3.2. The synthetic spectrum is a spectrum for a main sequence star with an average $B - V$ of $B - V = 0.53$. I obtained an average radial velocity of:

$$\langle R \rangle = (-14.97 \pm 0.76) \text{ km/s}.$$

Without the errors of the individual data points, the error of the average radial velocity is $\sigma = 0.12$ km/s. The average error of the individual measurements is 0.75 ± 0.01 km/s. The standard deviation of the radial velocity shifts is 0.57 km/s. In Fig. 9.14a, the variations of radial velocity shifts around the average radial velocity shift vs. time are shown. To find a period, a Fourier analysis was performed (Sect. 9.1). The periodogram of this analysis is shown in Fig. 9.15 and one sees a feature at the frequency of $\nu = 0.30325$. This frequency corresponds to a period of:

$$P \quad = \quad (3.30 \pm 0.02) \text{ day}.$$

This period has a FAP of 0.19. The radial velocity data are fitted with the sine function 9.5 and I obtained for the amplitude (A) and zero phase (φ) the following values:

$$A \quad = \quad (0.5 \pm 0.2) \text{ km/s}$$
$$\varphi \quad = \quad (47.6 \pm 12.5)^\circ$$
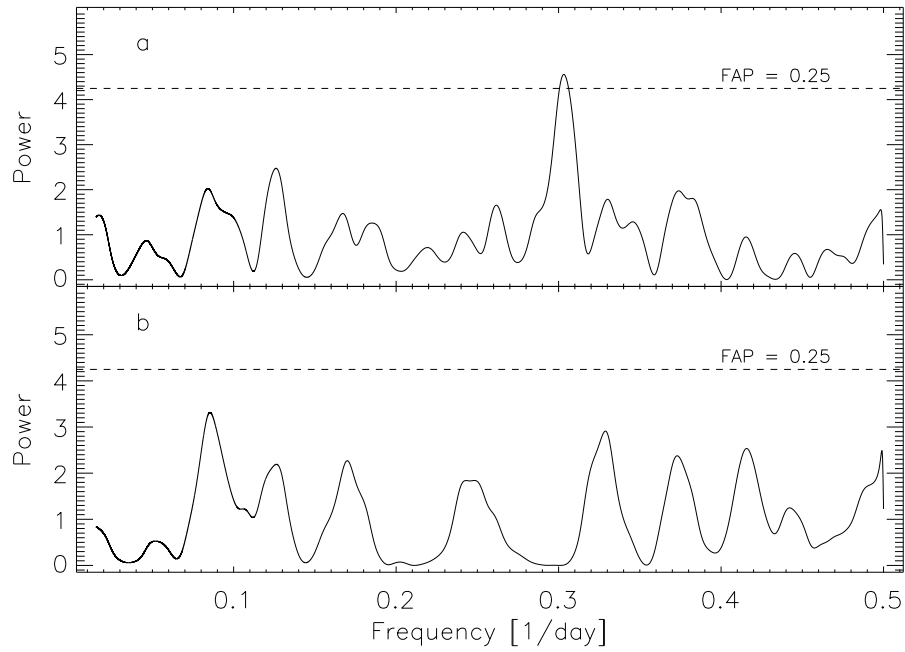
Figure 9.15: a: Periodogram of the radial velocity shifts of HD120136; b: Periodogram of the residuals
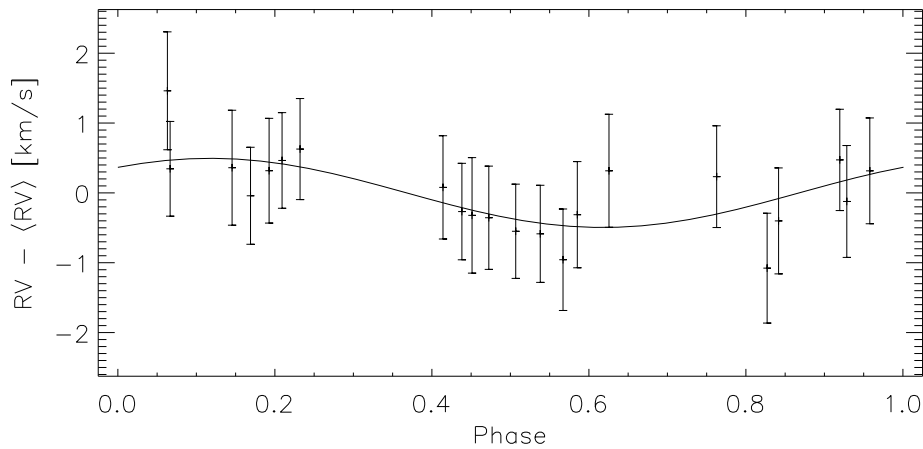
Figure 9.16: Phaseplot of the radial velocity shifts of HD120136

In Fig. 9.14a, the solid line represents the fit. For the reduced χ^2 of this fit, I obtained:

$$\chi^2 \quad = \quad 0.32.$$

This χ^2 is clearly smaller than 1. Here, the errors of the radial velocity shifts are too high to compare the variations. This large error could be caused by the variations of the
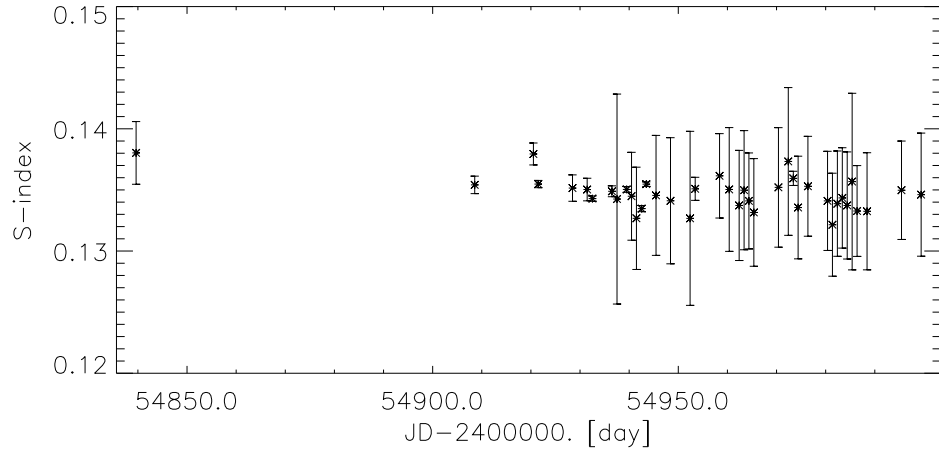
Figure 9.17: Time series of the S-index of HD121370

accuracy of the wavelength solution in the different spectral orders, see Sect. 5.2.

The residuals of this fit are shown in Fig. 9.14b and the standard deviation of the residuals is 0.43 km/s. Furthermore, the periodogram of the residuals does not show a peak at the period of 3.3 day, see Fig. 9.15b.

In Fig. 9.16, the radial velocity vs. phase is shown. The solid line represents the sine function with corresponding amplitude and phase. One sees in Fig. 9.14 and Fig. 9.16 that the fit describes the radial velocity shifts very well.

I can conclude that the period and the velocity amplitude are comparable with the values measured by Butler et al. (1997).

9.5 HD121370

HD121370 is also known as η Boo. This object is a spectroscopic binary with a period of 494 days (Bertiau 1957; Attia et al. 2009). To detect this period, the observation period was too short. Therefore, I present only the time series of the S-index. Before I will give some basic information about this object.

The colour index is $B - V = 0.580$ mag and, therefore, I obtained an effective temperature of $T_{eff} = 5978$ K with Eq. 6.13. The visual magnitude and the distance are 2.68 mag and (11.34 ± 0.10) pc, respectively. Thus, I obtained an absolute magnitude of (2.41 ± 0.09) mag. In connection with the $B - V$, the position in the H-R diagram is located in the subgiant area.

In the following, the time series of the S-index is presented. For this time series of the S-index of HD121370, observations covering 39 nights are used with the exposure time being 480 sec. For the average S-index and log R'_{HK}, I obtained:

$$\langle S \rangle = (0.135 \pm 0.006)$$
$$\log R'_{HK} = (-5.26 \pm 0.13).$$
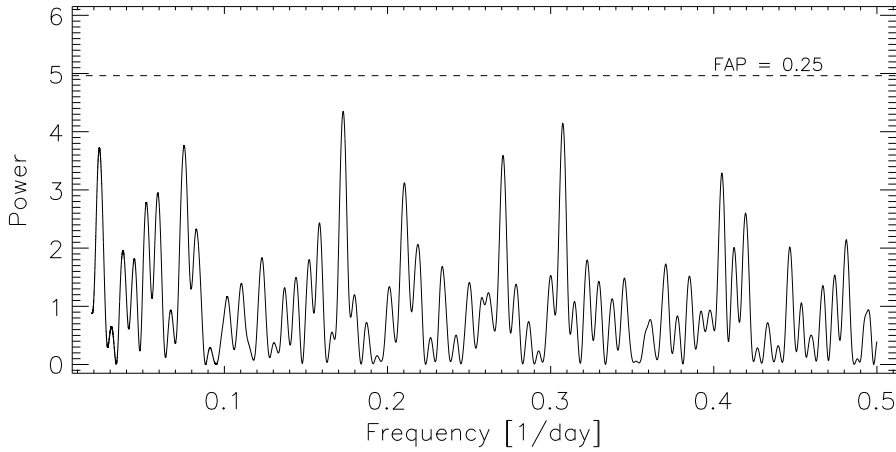
Figure 9.18: Periodogram of the S-index time series of HD121370

The standard deviation of the S-indices is 0.001. With the Eq. 9.6, I estimated a rotation period of:

$$\frac{P}{sini} \;=\; (11.6 \pm 5.0) \text{ day.}$$

For the estimation of this rotation period, I used $logR = (0.40 \pm 0.02)\ R_{\odot}$ (Allende Prieto and Lambert 1999) and the $vsini = (11.0 \pm 3.0)$ km/s (Glebocki and Stawikowski 2000). In Fig. 9.17, the S-index vs. time is shown. Here is no strong periodic variability to be recognised. Nevertheless, I performed a Fourier analysis (Sect. 9.1) to check this time series for a periodicity. In Fig. 9.18, the periodogram is shown and one cannot see a significant peak. Therefore, there is no periodic variation in the time series of the S-index.

9.6   HD142373

HD142373 is called also χ Her. This object is one of the template candidates which are discussed in Sect. 8.2. The basic object parameter are given in Sect. 8.2 Table 8.1. In this section, I present the time series of the S-indices to check whether a periodic variation in the S-index exists. If a period exists, this object is not feasible as a template star.
The S-indices of 40 nights are used for the time series. The exposure time of the spectra was 480 sec. For the average S-index and log R'_{HK}, I obtained:

$$\langle S \rangle \;=\; (0.148 \pm 0.012)$$
$$\log\ R'_{\text{HK}} \;=\; (-5.08 \pm 0.17).$$

The standard deviation of the S-indices is 0.009. First, I estimated the rotation period with the Eq. 9.6 and I obtained:

$$\frac{P}{sini} \;=\; (30.5 \pm 16.1) \text{ day.}$$
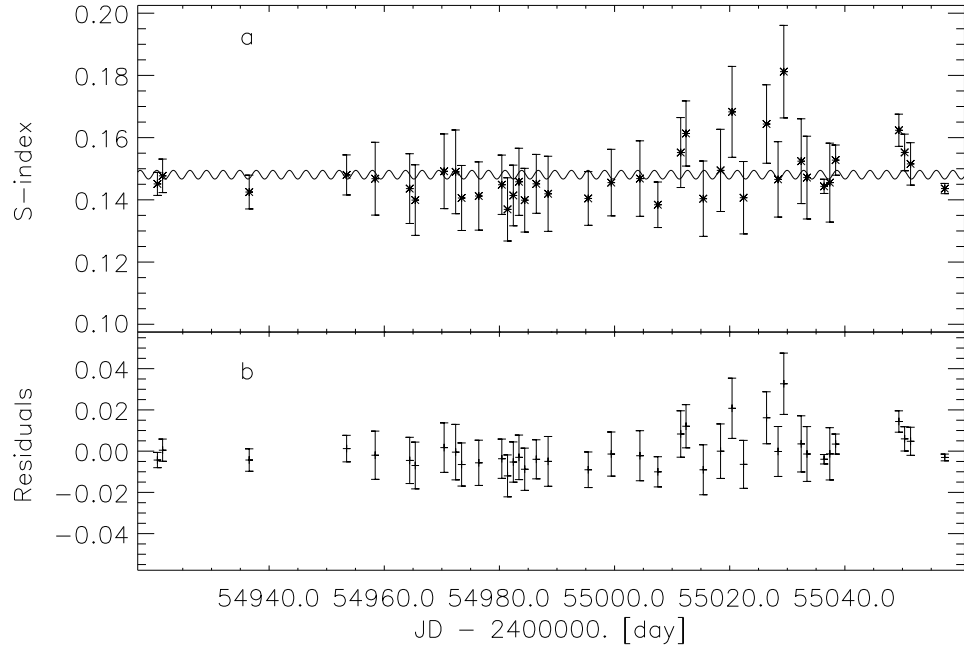
Figure 9.19: a: Time series of the S-index of HD142373 with the sine fit; b: Residuals of the sine fit

For the estimation of this rotation period, I used $logR = (0.16 \pm 0.03)\ R_\odot$ (Allende Prieto and Lambert 1999) and the $vsini = (2.40 \pm 0.80)$ km/s (Glebocki and Stawikowski 2000). In Fig. 9.19a, the S-index vs. time is shown. At the end of the time series, the scattering of the S-indices is larger. To find a period, a Fourier analysis was performed (Sect. 9.1). The periodogram of this analysis is shown in Fig. 9.20 and one can see a significant peak at the frequency $\nu = 0.34712$ 1/day. This frequency corresponds to the period of:

$$P \quad = \quad (2.88 \pm 0.05) \text{ day}.$$

This peak has a FAP of 0.18. With this period, I fitted the data with the sine function 9.5 to determine the amplitude of the variation and to check this period. This fit is represented as a solid line in Fig. 9.19a. The reduced χ^2 of this fit is:

$$\chi^2 \quad = \quad 0.97.$$

I obtained for the amplitude and zero phase of the fit:

$$A \quad = \quad (0.0014 \pm 0.0012)$$
$$\varphi \quad = \quad (103.7 \pm 64.7)^\circ.$$

The amplitude of the S-index variations is very small. The difference between the amplitude and the error of the amplitude is tiny. Based on the small amplitude and the significance of the peak at $\nu = 0.34712$ 1/day in the periodogram, it is not clear whether this period is real or caused by the data noise. Furthermore, the scattering of residuals
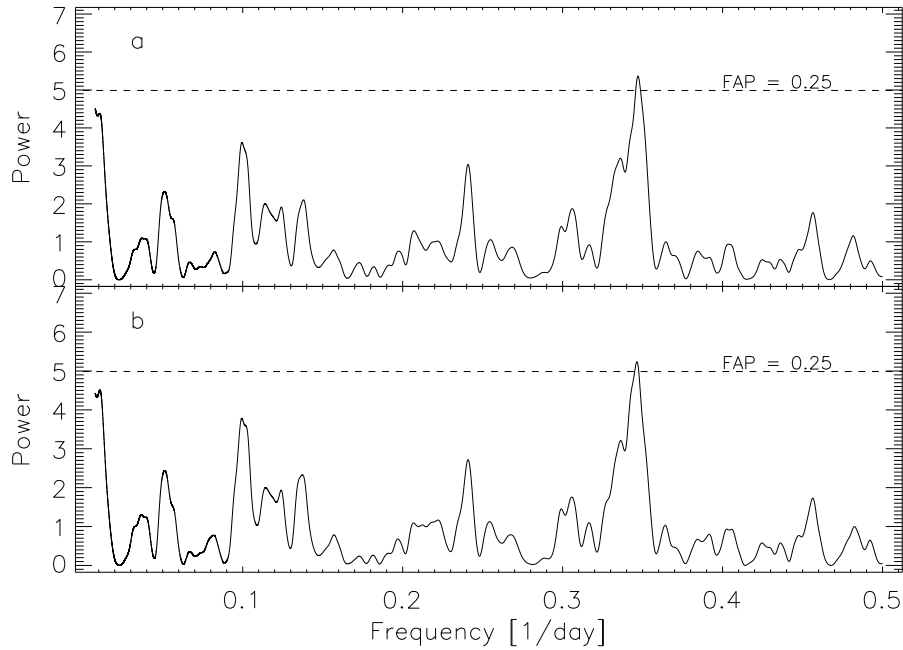
Figure 9.20: a: Periodogram of the S-index time series of HD142373; b: periodogram of the residuals

of the fit does not differ much from the data, see Fig. 9.19b. The standard deviation of the residuals is 0.009. The difference between the standard deviation of the residuals and standard deviation of the S-indices is only 0.8%. Furthermore, the residuals are checked if the periodic variation is eliminated. In Fig. 9.20b, the periodogram of the residuals is shown. One can see that the peak has not disappeared. The significance of the peak is slightly smaller. Nevertheless, this period is clearly smaller than the period calculated with Eq. 9.6. To verify if this period is caused by noise, it is necessary to further observe this object because a period is an exclusion criterion for a template star.

9.7   Summary

In this chapter, I could demonstrate the potential and some capabilities of the HRT. I presented the first time series of the S-index with the aim to find rotation periods.
The longest time series of S-index is of the Sun, from Oct. 2008 until Jul. 2009. In this time series, no rise in activity could be recognized. The S-index is constant over this observation period. For all objects, I tried to find rotation periods. In the time series for the Sun, HD79028, HD120136 and HD142373, I found possible periodic variations. The significance of the corresponding peaks in the periodograms are smaller than 99.9% so that these periods are not surely detected. The possible reasons for these low significances are the total number of data points for these individual objects and the scattering in the S-indices. For the Sun and HD120136, the rotation periods are known. In the case of the Sun, the period is different of the rotation period. This was not unexpected because most

of the days were spotless. The possible reason for this peak is a superposition of the stellar rotation and the evolution of the active regions on the Sun. In the case of HD120136, the detected period of 3.19 days is consistent with the known rotation period. For HD121370, I found no periodic variations in the S-index.

To verify these results, it is necessary to monitor these objects further. Considering the total number of data points and the problem of the dark noise, the results are very good. These results also show that the accuracy of the S-index needs to be increased. This will be achieved by changing the spectrograph's CCD camera because with the new camera the strong dark noise in the data presented here will be eliminated.

Furthermore, I determined radial velocity shifts and the periods of these radial velocity shifts for HD79028 and HD120136. For HD120136, the significance of the peak in the periodogram is only 81%. The determined periods are consistent with the literature values. The values of the amplitudes are very different and I obtained for HD79028 34.9 km/s and for HD120136 only 0.5 km/s. These values are also consistent with the literature values. Therefore, I can conclude that this test was successful. Further, at the example of HD120136, the limits of the accuracy of the wavelength calibration and the method which performed the determination of the radial velocity shift are shown. The radial velocity shifts of HD120136 are at the limit of the possibility to detect a radial velocity shift because the errors of the radial velocity shifts for the individual data points are clearly greater than the amplitude of the radial velocity shift. However, the peak at the orbital period is seen very well in the periodogram. The significance of this peak is only 81%.

The accuracy of the determination of the radial velocity shifts can be increased with the beginning of the operation of the red channel of the spectrograph. Another possibility to increase the accuracy is the implementation of the pressure, temperature and humidity dependence of the wavelength calibration.

Chapter 10

Summary and Outlook

I have presented the fully automatic data reduction pipeline of the HRT with an automatic wavelength calibration for the blue spectral range of the spectrograph. This pipeline is based on the IDL reduction package REDUCE by Piskunov and Valenti (2002). The REDUCE package was adapted to the HEROS spectrograph and additional IDL procedures had to be created for the reduction process. I have described the reduction process and the important reduction procedures with the additional aim to provide a manual for the data reduction pipeline. The pipeline was applied to extract all spectra which have been used in this thesis. This served also as a test for the stability and performance of the automatic extraction procedure. Hence, I was able to show that the pipeline is working properly and is stable. Nevertheless, I have shown that one problem in the reduction pipeline is the identification of faint outliers in the science image. An outlier correction is implemented, but the accuracy of this correction depends on the size of the swath width. In the pipeline, a relatively small swath width (Sect. 4.4.10.4) is used and therefore, the accuracy of the outlier correction is not very high. Some of these outliers are caused by the CCD of the spectrograph. The camera has a high dark noise because it is not possible to cool below $-25°$C. Furthermore, the continuum normalisation process of late type stars may have problems in finding the quasi-continuum segments of the spectrum.

I was also able to show that the wavelength shifts depend on the air pressure, air temperature and humidity. This dependence has an influence on the wavelength solution. To optimise the accuracy of the wavelength solution, this effect needs to be considered in the future. Additionally, I found relatively high scattering in the velocity shifts for the wavelengths. This scattering has a strong effect of the accuracy on the radial velocity shifts.

In this thesis, the first results of the HRT observations have been presented. One of these results is the transformation equation for the conversion of the S-index of the HRT to the Mount Wilson S-index. This transformation is necessary for the direct comparison with the S-indices obtained by other telescopes. For the transformation equation, I have used the average S-indices by Baliunas et al. (1995), Hall (private communication), Hall et al. (2009) and the average S-indices measured with the HRT. I obtained a linear relation between the S-index of the HRT and the Mount Wilson S-index. The standard deviation of the residuals is 0.0011. In an average, the results transformed to the Mount Wilson S-index (Eq. 6.20) deviate from the reference S-indices by about 4%. Furthermore, I have determined the conversion factor K for the conversion of the relative flux to the absolute flux.

The flux of the Ca II H+K lines is composed of the flux created in the photosphere and chromosphere of a star. To obtain only the chromospheric part, it is necessary to subtract the photospheric one. Hence, I have created a new photospheric flux correction, which depends on the colour index $B - V$, for main sequence stars, subgiants and giant stars, using the multi-purpose stellar atmosphere code PHOENIX. Furthermore, I have determined the excess flux of Ca II H+K lines for a sample of stars applying this correction. For main sequence stars, I have found two general trends between the excess flux of the Ca II H+K lines and the rotation periods. I have derived three linear relations for the calculation of the rotation period of main sequence stars.

Following the new photospheric correction, I have presented the spectra of the first six objects of the sample of possible template stars. The line cores of the Ca II H+K lines in those observed spectra were analysed for the detectability of a double peak structure which yielded negative results for two objects. In the four other stars, a faint double peak structure was detected.

The first time series of S-indices of five objects have been presented. The longest time series was that of the Sun from Oct. 2008 until Jul. 2009. The observed activity level of the Sun remained constant. Furthermore, I have investigated the Ca II H+K lines in the lunar spectrum taken on a day with the relative sunspot number $R = 0$. In this spectrum, a faint double peak structure is observed in the Ca II K line and not in the Ca II H line. This fact has an influence on the template search, since a star is possibly applicable as a template star with a faint double peak structure in the Ca II K line and without one in Ca II H line. For all stars, I have tried to find their rotation periods. The periods of the Sun and HD120136 are known from literature. To find a periodic variation in the time series of the S-index, I have performed a Fourier analysis with the Lomb-Scargle method. For four stars, including the Sun and HD120136, I have found such periods. The significance of the corresponding peaks in the periodograms was not strong enough for a clear detection. Hence, these peaks can only be interpreted as a hint of possible periods. The period of the Sun is clearly different from the literature value whereas here, the rotation period of the Sun was not expected to be detected because most of the days were spotless. This peak is possibly caused by a superposition of the stellar rotation and the evolution of active regions.

In the case of HD120136, the detected period of 3.19 days is consistent with the literature value. The low significance of the peak is caused by the low total number of data points. The amplitude of the variation is consistent with zero. From the individual time series, it can be concluded that the error of the S-indices are relatively high. These high errors are caused by the consideration of dark noise of the spectrograph's CCD in the error calculation and it is possible oversized. Nevertheless, the influence of the dark noise is seen in some of the spectra for the template search. However, this problem with the dark noise will hopefully be solved by replacing the camera.

Additionally, I have presented radial velocity shifts for HD79028 and HD120136. The period of the radial velocity shifts are known which allows for a good test of the accuracy of the wavelength calibration and the method with which the radial velocity shifts are calculated. I found the known period for HD79028. Furthermore, I calculated the orbital parameters for this star and these values are comparable with the literature values. The strongest peak in the periodogram of HD120136 was at the known frequency. However, the significance of the corresponding peak in the periodograms for HD120136 was lower than 99.9%. Nevertheless, this represents a very good result because for the determination

of the period only 22 data points were available. The individual errors of the data points were greater than the amplitude of the variations. The amplitude of the radial velocity shifts of HD120136 shows the limit of the possibility to detect a periodic radial velocity shift. In the following, I will give an overview over the future tasks.

Mainly, this thesis shows the current state and the potential of the HRT. After finishing this thesis, the data reduction pipeline of the blue channel will be adapted on the new CCD camera. Furthermore, the wavelength solution will be optimised to reduce the scatter in the wavelength shifts. Additionally, the correction of the wavelength shift depending on the temperature, pressure and humidity will be included in the data reduction pipeline.

The creation of the data reduction pipeline for the red spectral channel of the spectrograph will be started if the red channel is in operation. When this channel is properly working and enough ThAr data has been taken, the wavelength shifts will be investigated for a dependence on the temperature, pressure and humidity.

With the completion of the red spectral channel of the spectrograph, the field of applications will be expanded. It will be possible to find and to investigate a relation between the Ca II H+K line and the Ca II triplet (8498.02 Å, 8542.09 Å, 8662.14Å). Furthermore, the radial velocity determination could be optimised because a larger wavelength range is available. In the range of 6000 Å, single spectral lines are present which could significantly improve the determination of the radial velocity shift.

The spectrograph upgrade for the blue spectral channel will require a test and possibly the re-determination of the transformation equation for the S-index.

Furthermore, follow-up observations for the template candidates will be performed because the new CCD will eventually eliminate the dark noise influence which will yield more precise structures of the line cores of the Ca II H+K lines. In addition, the template candidates will be monitored to find a periodic variability of the S-index. The observation of other templates candidates will be performed as well.

The HRT will not only be used for searching template stars. With the HRT, it is possible to measure rotation periods of active stars. These periods can be use for the optimisation of the relation between the excess flux of the Ca II H+K lines and rotation period.

In addition to the observations with the HRT, the work on the photospheric flux correction of the Ca II H+K lines created with PHOENIX should be continued. The connection between the photospheric flux in the Ca II H+K lines and the metallicity should be investigated with the aim that the photospheric flux corrections consider the colour index $B - V$ and the metallicity. Furthermore, the evolutionary state of a star has an influence of the photospheric flux, too. This influence is roughly considered in the individual correction equations for main sequence, subgiant and giant stars. In further investigations, these three equations will be connected to a single one. This equation would depend on the colour index $B - V$, metallicity and the absolute magnitude. With the consideration of the metallicity and the absolute magnitude, the accuracy of the photospheric flux correction can be increased.

Appendix A

Table

Parameter	Value
xr	[130, 1924]
yr	[485, 1684]
orient	1
backn	0
xwd1	6.
xwd2	7.
osample	12.
sf_smooth	10.
sp_smooth	10.
swath_width	25
power	2
thresflat	50.
thresdark	30.
use_dark_thres	0.01
thresbias	10.
threscosmic	5.0
filter	200.
min_order_size	35.
order_width	1.999
obase	100.
inst_mode	heros_blue
master_thar	directory+name of the master Th-Ar spectrum
path_master_1d_solution	directory of the sav file of the 1 D wavelength solution

Table A.1: The parameters and the default values of the extraction

Relative order	a	b	c
0	-0.01925±0.00010	-0.03335±0.00032	-0.00300±0.00012
1	-0.02068±0.00001	-0.02797±0.00003	-0.00082±0.00001
2	-0.02166±0.00001	-0.02939±0.00003	-0.00186±0.00001
3	-0.02096±0.00008	-0.02690±0.00025	-0.00125±0.00010
4	-0.02082±0.00001	-0.02980±0.00003	-0.00210±0.00001
5	-0.02139±0.00006	-0.02837±0.00022	-0.00159±0.00009
6	-0.02145±0.00007	-0.02852±0.00026	-0.00156±0.00010
7	-0.02133±0.00003	-0.02954±0.00011	-0.00173±0.00004
8	-0.02106±0.00010	-0.02802±0.00035	-0.00116±0.00014
9	-0.02134±0.00003	-0.02884±0.00011	-0.00138±0.00004
10	-0.02130±0.00001	-0.02834±0.00005	-0.00119±0.00002
11	-0.02084±0.00001	-0.02830±0.00004	-0.00110±0.00001
12	-0.02036±0.00001	-0.02693±0.00004	-0.00189±0.00002
13	-0.02058±0.00002	-0.02854±0.00006	-0.00137±0.00002
14	-0.02085±0.00002	-0.02867±0.00007	-0.00106±0.00003
15	-0.02058±0.00001	-0.02798±0.00005	-0.00106±0.00002
16	-0.02144±0.00001	-0.03162±0.00003	-0.00225±0.00001
17	-0.02082±0.00001	-0.02929±0.00004	-0.00105±0.00002
18	-0.02093±0.00005	-0.02843±0.00018	-0.00152±0.00007
19	-0.02116±0.00002	-0.02963±0.00007	-0.00137±0.00003
20	-0.02046±0.00002	-0.02827±0.00008	-0.00082±0.00003
21	-0.02019±0.00002	-0.02819±0.00007	-0.00069±0.00003
22	-0.02223±0.00002	-0.03056±0.00006	-0.00179±0.00002
23	-0.02117±0.00002	-0.02948±0.00007	-0.00133±0.00003
24	-0.02064±0.00002	-0.02880±0.00007	-0.00100±0.00003
25	-0.02181±0.00002	-0.03011±0.00006	-0.00159±0.00002
26	-0.02094±0.00002	-0.02903±0.00007	-0.00101±0.00003
27	-0.02117±0.00002	-0.02932±0.00008	-0.00116±0.00003
28	-0.02125±0.00002	-0.02994±0.00007	-0.00141±0.00003
29	-0.02016±0.00002	-0.02838±0.00006	-0.00084±0.00002
30	-0.01985±0.00010	-0.02729±0.00033	-0.00104±0.00013
31	-0.02092±0.00002	-0.02951±0.00008	-0.00133±0.00003
32	-0.02034±0.00004	-0.02851±0.00014	-0.00084±0.00005
33	-0.02148±0.00001	-0.03071±0.00005	-0.00144±0.00002
34	-0.02065±0.00002	-0.02957±0.00006	-0.00109±0.00002
35	-0.02152±0.00002	-0.03124±0.00007	-0.00161±0.00003
36	-0.02043±0.00002	-0.02896±0.00009	-0.00089±0.00003
37	-0.02099±0.00002	-0.03035±0.00008	-0.00118±0.00003
38	-0.02095±0.00002	-0.02954±0.00007	-0.00098±0.00003
39	-0.02095±0.00002	-0.03085±0.00007	-0.00126±0.00003
40	-0.02104±0.00015	-0.02981±0.00056	-0.00107±0.00022
41	-0.02015±0.00004	-0.02823±0.00012	-0.00091±0.00005
42	-0.02082±0.00002	-0.02809±0.00006	-0.00078±0.00002
43	-0.02073±0.00004	-0.02783±0.00012	-0.00151±0.00005
44	-0.02071±0.00003	-0.02990±0.00010	-0.00125±0.00004
45	-0.02137±0.00002	-0.02919±0.00009	-0.00110±0.00004
46	-0.02172±0.00003	-0.03152±0.00011	-0.00117±0.00005
47	-0.01742±0.00010	-0.02612±0.00038	0.00108±0.00015
48	-0.02079±0.00003	-0.03097±0.00009	-0.00100±0.00004
49	-0.02087±0.00002	-0.02968±0.00006	-0.00112±0.00003

Table A.2: The parameter of the air pressure, temperature, humitidy pixel shift correction equation 5.2

Sp Typ	B-V	T_{eff}	log g	M/M$_\odot$	ξ	vsini
F5V	0.44	6528	4.3	1.41	6.2	20.0
F8V	0.53	6160	4.4	1.25	5.1	9.0
G0V	0.59	5943	4.4	1.16	4.4	6.4
G2V	0.63	5811	4.4	1.11	3.7	4.8
G5V	0.68	5657	4.5	1.05	2.8	3.4
G8V	0.74	5486	4.5	0.97	1.9	2.6
K0V	0.82	5282	4.6	0.90	1.5	2.2
K2V	0.92	5055	4.6	0.81	1.2	2.0
K3V	0.96	4973	4.6	0.79	0.8	2.0
K5V	1.15	4623	4.6	0.65		1.9
K7V	1.28	4410	4.7	0.54		1.7

Table A.3: The physical parameter for main sequence stars to calculate the synthetic spectra

Sp Typ	B-V	T_{eff}	log g	M/M$_\odot$	ξ	vsini
G2III	0.76	5433	3.1	4.59	6.7	25.0
G5III	0.90	5098	2.8	2.79	5.8	5.8
G8III	0.96	4973	2.7	2.63	5.2	4.0
K0III	1.03	4836	2.5	2.26	4.8	3.0
K2III	1.18	4572	2.1	1.33	4.5	2.3

Table A.4: The physical parameter for giant stars to calculate the synthetic spectra

B-V	T_{eff}	log g	M/M$_\odot$	vsini
0.44	6528	4.1	1.5	26.0
0.50	6085	4.0	1.4	26.0
0.60	5910	4.0	1.3	8.0
0.70	5598	4.0	1.2	6.0
0.80	5331	3.8	1.1	4.0
0.90	5098	3.5	1.1	3.0
1.00	4893	3.4	1.1	2.0
1.10	4709	3.2	1.1	1.0

Table A.5: The physical parameter for subgaint stars to calculate synthetic spectra

Object	Luminosity class	$B-V$	S	$\log R'_{\mathrm{HK}}(Noyes)$	R'_{HK}
Sun	V	0.642	0.171	-4.937	-4.898±0.075
HD1835	V	0.659	0.360	-4.415	-4.297±0.035
HD2454	V	0.447	0.170	-4.793	-4.839±0.095
HD3229	IV	0.444	0.215	-4.612	-4.574±0.062
HD3443	V	0.715	0.182	-4.917	-4.888±0.065
HD3651	V	0.850	0.185	-4.960	-5.023±0.062
HD3795	IV	0.718	0.158	-5.024	-4.981±0.069
HD4628	V	0.890	0.230	-4.852	-4.878±0.047
HD9562	IV	0.639	0.145	-5.102	-5.086±0.100
HD10476	V	0.836	0.210	-4.874	-4.884±0.052
HD10700	V	0.727	0.172	-4.955	-4.963±0.071
HD12235	IV	0.610	0.170	-4.924	-4.872±0.073
HD13421	IV	0.569	0.130	-5.205	-5.364±0.207
HD16160	V	0.918	0.230	-4.939	-4.918±0.047
HD16673	V	0.524	0.215	-4.663	-4.582±0.056
HD17925	V	0.862	0.700	-4.278	-4.157±0.028
HD18256	IV	0.471	0.170	-4.793	-4.865±0.097
HD20630	V	0.681	0.345	-4.454	-4.345±0.036
HD22049	V	0.881	0.510	-4.441	-4.350±0.030
HD22072	IV	0.891	0.135	-5.186	-5.218±0.068
HD23249	IV	0.915	0.137	-5.186	-5.215±0.064
HD25998	V	0.520	0.275	-4.502	-4.373±0.043
HD26913	V	0.680	0.385	-4.407	-4.276±0.034
HD26923	V	0.570	0.285	-4.496	-4.379±0.041
HD26965	V	0.820	0.205	-4.876	-4.886±0.054
HD29645	IV	0.593	0.135	-5.156	-5.239±0.151
HD30495	V	0.632	0.285	-4.522	-4.428±0.041
HD32147	V	1.049	0.300	-4.940	-4.920±0.039
HD33608	IV	0.462	0.210	-4.644	-4.603±0.063
HD35296	V	0.544	0.308	-4.429	-4.307±0.039
HD39587	V	0.594	0.300	-4.476	-4.361±0.040
HD43587	V	0.610	0.158	-4.990	-4.985±0.093
HD45067	IV	0.564	0.140	-5.101	-5.181±0.144
HD75332	V	0.549	0.270	-4.443	-4.405±0.043
HD76151	V	0.661	0.260	-4.622	-4.521±0.043
HD76572	IV	0.474	0.146	-4.941	-5.155±0.169
HD78366	V	0.585	0.240	-4.631	-4.522±0.048
HD81809	IV	0.642	0.175	-4.907	-4.847±0.066
HD82885	V	0.770	0.315	-4.579	-4.499±0.037
HD88737	IV	0.573	0.235	-4.621	-4.544±0.049
HD89744	IV	0.531	0.135	-5.130	-5.305±0.201
HD97334	V	0.600	0.320	-4.450	-4.322±0.038
					continue next page

Table A.6: Table with the object, the S-index and $\log R'_{\mathrm{HK}}(Noyes)$ from Noyes et al. (1984) and the estimed luminosity class, the $B-V$ and the $\log R'_{\mathrm{HK}}$ with the new photosphere corretion.

Table A.6 continue

Object	Luminosity class	$B-V$	S	$\log R'_{\text{HK}}(Noyes)$	R'_{HK}
HD100180	V	0.570	0.165	-4.922	-4.904±0.087
HD100563	V	0.480	0.195	-4.702	-4.665±0.067
HD101501	V	0.723	0.310	-4.548	-4.458±0.038
HD103095	V	0.754	0.180	-4.930	-4.939±0.065
HD106516	V	0.470	0.208	-4.651	-4.593±0.061
HD107213	IV	0.523	0.138	-5.077	-5.253±0.184
HD114378	V	0.455	0.240	-4.541	-4.453±0.051
HD114710	V	0.572	0.200	-4.756	-4.679±0.060
HD115383	V	0.585	0.310	-4.449	-4.332±0.039
HD115404	V	0.926	0.550	-4.467	-4.370±0.030
HD115617	V	0.709	0.160	-5.015	-5.037±0.084
HD120136	V	0.508	0.185	-4.759	-4.734±0.072
HD124570	IV	0.537	0.135	-5.137	-5.297±0.195
HD124850	IV	0.511	0.208	-4.689	-4.628±0.060
HD126053	V	0.639	0.170	-4.930	-4.903±0.076
HD131156A	V	0.720	0.450	-4.375	-4.225±0.032
HD131156B	V	1.170	1.400	-4.418	-4.281±0.026
HD136202	IV	0.540	0.140	-5.089	-5.200±0.158
HD141004	V	0.604	0.160	-4.971	-4.963±0.090
HD142373	IV	0.563	0.142	-5.089	-5.152±0.136
HD143761	V	0.612	0.150	-5.041	-5.069±0.108
HD149661	V	0.827	0.360	-4.541	-4.482±0.035
HD152391	V	0.749	0.400	-4.438	-4.326±0.033
HD154417	V	0.578	0.275	-4.519	-4.411±0.042
HD155885	V	0.855	0.375	-4.571	-4.493±0.034
HD155886	V	0.855	0.405	-4.532	-4.447±0.033
HD156026	V	1.144	0.835	-4.627	-4.490±0.028
HD157856	IV	0.457	0.196	-4.698	-4.677±0.072
HD158614	V	0.715	0.165	-4.990	-5.002±0.078
HD159332	IV	0.505	0.145	-4.999	-5.146±0.155
HD160346	V	0.959	0.305	-4.787	-4.769±0.038
HD161239	IV	0.683	0.140	-5.144	-5.134±0.098
HD165341A	V	0.860	0.385	-4.557	-4.483±0.034
HD165341B	V	1.160	0.980	-4.557	-4.437±0.027
HD166620	V	0.876	0.205	-4.910	-4.958±0.054
HD176051	V	0.594	0.180	-4.865	-4.805±0.070
HD176095	IV	0.478	0.200	-4.682	-4.660±0.067
HD182101	V	0.458	0.210	-4.637	-4.580±0.061
HD182572	IV	0.761	0.160	-5.034	-4.982±0.063
HD187013	V	0.476	0.150	-4.943	-5.057±0.137
HD187691	V	0.563	0.150	-5.017	-5.053±0.115
HD188512	IV	0.855	0.141	-5.148	-5.155±0.067
					continue next page

Table A.6 continue

Object	Luminosity class	$B-V$	S	$\log R'_{\mathrm{HK}}(Noyes)$	R'_{HK}
HD190007	V	1.128	0.780	-4.592	-4.498±0.028
HD190360	V	0.749	0.155	-5.049	-5.119±0.089
HD190406	V	0.600	0.190	-4.818	-4.749±0.064
HD194012	V	0.498	0.194	-4.739	-4.676±0.067
HD201091	V	1.069	0.605	-4.800	-4.534±0.029
HD206860	V	0.587	0.323	-4.424	-4.305±0.038
HD212754	IV	0.519	0.140	-5.075	-5.219±0.173
HD216385	IV	0.487	0.141	-5.032	-5.235±0.193
HD217014	V	0.666	0.155	-5.037	-5.048±0.093
HD219834A	IV	0.787	0.168	-4.999	-4.945±0.057
HD219834B	IV	0.910	0.220	-4.902	-4.820±0.039
HD224930	V	0.690	0.178	-4.901	-4.889±0.068

Object	Luminosity class	B-V	S	Ref	$\Delta\mathcal{F}'_{HK}$	Old/ Young	P_{obs}	Ref
sun	V	0.642	0.179	1	5.952±0.067	2.00	27.00	10
HD1835	V	0.659	0.349	1	6.466±0.035	1.00	7.70	2
HD2454	V	0.447	0.170	1	6.161±0.091	1.00	7.80	3
HD3651	V	0.850	0.176	1	5.542±0.067	2.00	48.00	2
HD4628	V	0.890	0.230	2	5.711±0.047	2.00	38.00	2
HD9562	IV	0.639	0.136	1	5.600±0.118	2.00	37.50	4
HD9826	IV	0.536	0.161	9	5.960±0.092	3.00	14.00	9
HD10476	V	0.836	0.198	1	5.692±0.056	2.00	35.20	8
HD13421	IV	0.569	0.131	1	5.519±0.187	2.00	4.35	7
HD16160	V	0.918	0.226	1	5.636±0.048	2.00	45.00	2
HD16673	V	0.524	0.215	1	6.334±0.054	1.00	5.70	2
HD20630	V	0.681	0.366	1	6.454±0.034	1.00	9.40	2
HD22049	V	0.881	0.496	1	6.232±0.031	1.00	11.30	2
HD25998	V	0.520	0.300	1	6.612±0.040	1.00	2.60	2
HD26913	V	0.680	0.396	1	6.504±0.033	1.00	7.20	2
HD30495	V	0.632	0.297	1	6.408±0.039	1.00	7.60	2
HD32147	V	1.049	0.286	1	5.525±0.041	2.00	48.00	5
HD35296	V	0.544	0.332	1	6.640±0.037	1.00	3.56	8
HD39587	V	0.594	0.325	1	6.538±0.037	1.00	5.20	2
HD75732	V	0.869	0.190	9	5.583±0.059	2.00	42.00	6
HD78366	V	0.585	0.248	1	6.358±0.045	1.00	9.67	8
HD81809	IV	0.642	0.172	1	5.931±0.066	2.00	40.50	4
HD89744	IV	0.531	0.137	1	5.637±0.174	2.00	12.30	2
HD97334	V	0.600	0.335	1	6.547±0.036	1.00	7.60	2
HD100180	V	0.570	0.165	1	5.962±0.084	2.00	14.00	2
HD101501	V	0.723	0.311	1	6.269±0.037	1.00	17.10	2
HD103095	V	0.754	0.188	1	5.803±0.060	2.00	31.10	4
HD106516	V	0.470	0.210	8	6.392±0.058	3.00	6.91	8
HD114378	V	0.455	0.244	1	6.555±0.049	1.00	3.00	2
HD114710	V	0.572	0.201	1	6.192±0.058	1.00	12.40	2
HD115383	V	0.585	0.313	1	6.529±0.038	1.00	3.30	8
HD115404	V	0.926	0.535	1	6.178±0.030	1.00	18.80	2
HD117176	IV	0.714	0.145	9	5.646±0.081	2.00	31.00	9
HD120136	V	0.508	0.191	1	6.236±0.066	1.00	3.20	9
HD124570	IV	0.537	0.133	1	5.550±0.202	2.00	5.65	7
HD124850	IV	0.511	0.210	1	6.311±0.057	1.00	7.60	2
								continue next page

Table A.7: The data used for the investigation too the flux excess and rotation period.

Ref: [1] Baliunas et al. (1995), [2] Noyes et al. (1984), [3] Rutten (1987), [4] Dobson (1992), [5] Baliunas and Vaughan (1985), [6] Baliunas et al. (1998), [7] Stimets and Giles (1980), [8] Hempelmann et al. (1996), [9] Henry et al. (2000), [10] Shkolnik et al. (2005), [11] Messina and Guinan (2003)

Table A.7 continue

Object	Luminosity class	B-V	S	Ref	$\Delta\mathcal{F}'_{HK}$	Old/ Young	P_{obs}	Ref
HD129333	V	0.626	0.530	4	6.773±0.030	3.00	2.70	11
HD131156A	V	0.720	0.461	1	6.516±0.031	1.00	6.20	2
HD131156B	V	1.170	1.381	1	6.113±0.026	1.00	11.50	2
HD136202	IV	0.540	0.140	1	5.693±0.149	2.00	2.33	7
HD141004	V	0.604	0.155	1	5.819±0.095	2.00	18.00	2
HD143761	V	0.612	0.150	1	5.754±0.104	2.00	17.00	6
HD149661	V	0.827	0.339	1	6.119±0.036	1.00	21.30	2
HD152391	V	0.749	0.393	1	6.366±0.033	1.00	11.10	2
HD154417	V	0.578	0.269	1	6.433±0.042	1.00	7.60	2
HD155885	V	0.855	0.384	1	6.138±0.034	1.00	22.90	2
HD155886	V	0.855	0.375	1	6.124±0.034	1.00	20.30	2
HD160346	V	0.959	0.300	1	5.759±0.039	2.00	33.50	2
HD165341A	V	0.860	0.392	1	6.140±0.033	1.00	19.70	2
HD166620	V	0.876	0.190	1	5.568±0.059	2.00	42.00	2
HD182101	V	0.458	0.216	1	6.438±0.057	1.00	5.02	3
HD186427	V	0.661	0.154	9	5.722±0.092	2.00	31.00	9
HD187691	V	0.563	0.148	1	5.793±0.116	2.00	15.00	3
HD190007	V	1.128	0.746	1	5.907±0.028	1.00	29.30	2
HD190406	V	0.600	0.194	1	6.110±0.060	1.00	13.50	2
HD201091	V	1.069	0.658	1	5.976±0.029	2.00	35.37	8
HD206860	V	0.587	0.330	1	6.561±0.037	1.00	4.70	2
HD212754	IV	0.519	0.140	1	5.695±0.163	2.00	13.00	3
HD217014	V	0.666	0.149	1	5.661±0.101	2.00	37.00	6
HD219834B	IV	0.910	0.204	1	5.702±0.041	2.00	42.00	2

Element	Fe I	Fe I	Fe I	Fe I	Fe I	Si I	Fe I
λ [Å]	3859.911	3878.018	3886.282	3895.656	3899.707	3902.945	3905.523
Element	Al I	Al I	Fe I	Mn I	Mn I	Fe I	
λ [Å]	3944.0058	3961.52	4005.241	4030.76	4033.76	4045.813	

Table A.8: Elements and laboratory wavelength which use to eliminate the additional continuum in the day light sun spectra

Range	1	2	3	4	5	6	7
λ [Å]	3900-4000	4112-4152	4200-4240	4509-4549	4841-4881	5147-5187	5153-5193
Range	8						
λ [Å	5163-5203						

Table A.9: Wavelenghtrange for the cross correlation to estimate the radial velocity shift
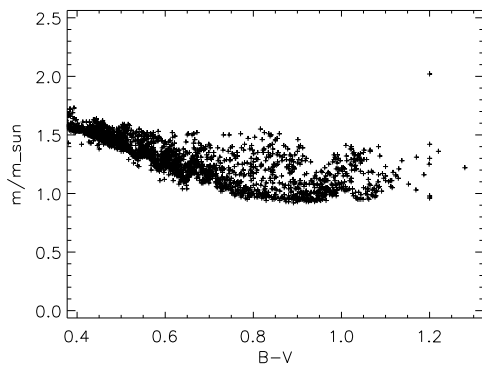
Appendix B

Plots

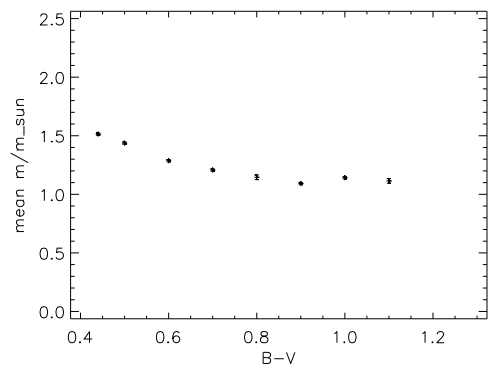Figure B.1: The $M/M_\odot$ of the subgiant (Allende Prieto and Lambert 1999)
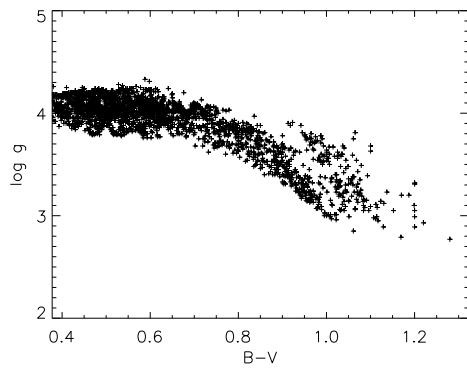

Figure B.2: The average $M/M_\odot$ of the subgiant

Figure B.3: The log g of the subgiant (Allende Prieto and Lambert 1999)
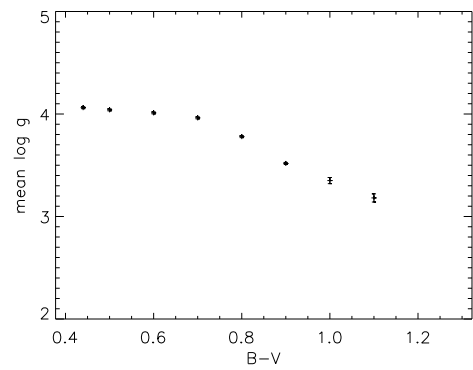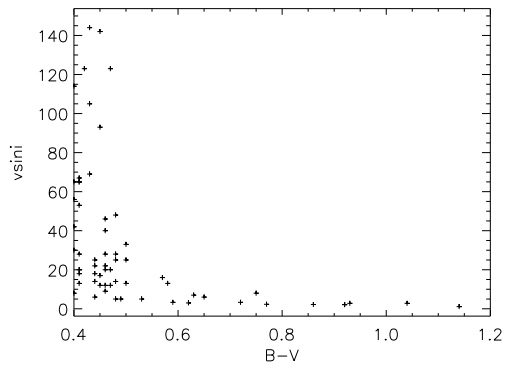

Figure B.4: The average $log\ g$ of the subgiant

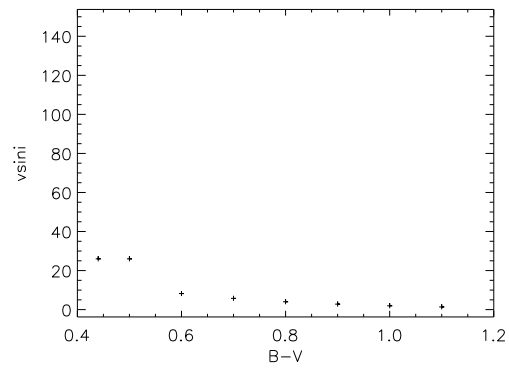Figure B.5: The vsini of the subgiant selected from Schrijver and Pols (1993)
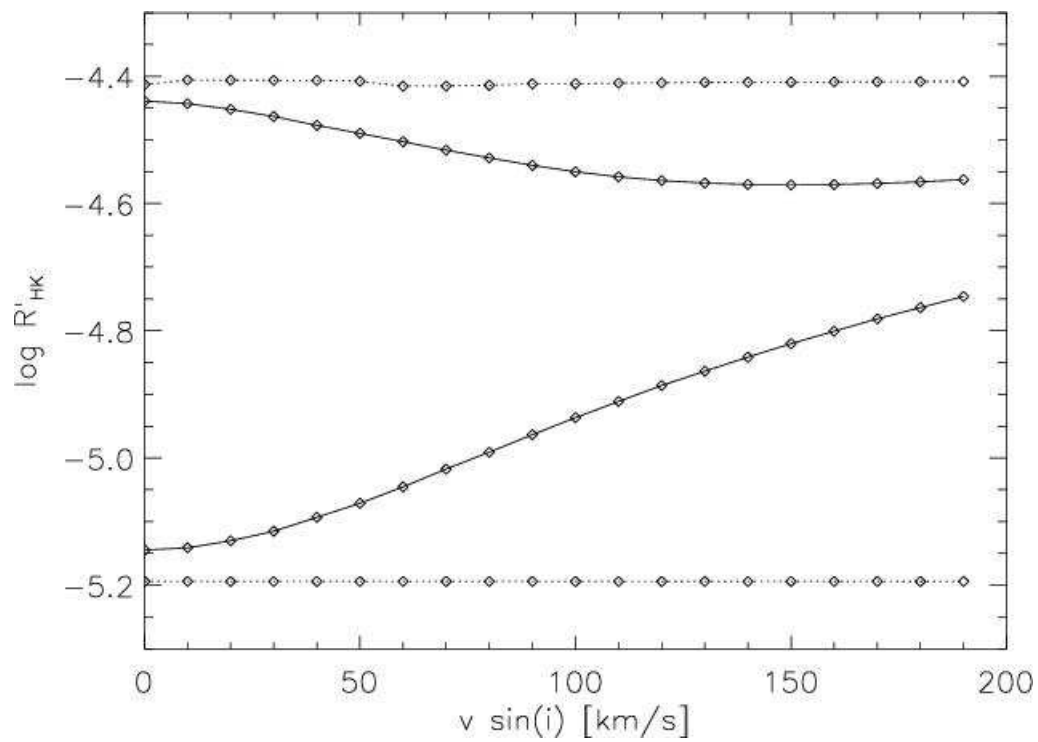

Figure B.6: The average vsini of the subgiant

Figure B.7: The influence of the vsini at $\log R'_{\mathrm{HK}}$ (Schröder et al. 2009)

Bibliography

H. A. Abt and S. G. Levy. Multiplicity among solar-type stars. *ApJS*, 30:273–306, March 1976. doi: 10.1086/190363.

C. W. Allen. *Astrophysical Quantities*. 1976.

C. Allende Prieto and D. L. Lambert. Fundamental parameters of nearby stars from the comparison with evolutionary calculations: masses, radii and effective temperatures. *A&A*, 352:555–562, December 1999.

M. Asplund, N. Grevesse, and A. J. Sauval. The Solar Chemical Composition. In T. G. Barnes, III and F. N. Bash, editors, *Cosmic Abundances as Records of Stellar Evolution and Nucleosynthesis*, volume 336 of *Astronomical Society of the Pacific Conference Series*, pages 25–+, September 2005.

A.-F. Attia, E. Mahmoud, H. I. Shahin, and A. M. Osman. A modified genetic algorithm for precise determination the geometrical orbital elements of binary stars. *New Astronomy*, 14:285–293, April 2009. doi: 10.1016/j.newast.2008.08.005.

H. W. Babcock. The Topology of the Sun's Magnetic Field and the 22-YEAR Cycle. *ApJ*, 133:572–+, March 1961. doi: 10.1086/147060.

S. L. Baliunas and A. H. Vaughan. Stellar activity cycles. *ARA&A*, 23:379–412, 1985. doi: 10.1146/annurev.aa.23.090185.002115.

S. L. Baliunas, R. A. Donahue, W. H. Soon, J. H. Horne, J. Frazer, L. Woodard-Eklund, M. Bradford, L. M. Rao, O. C. Wilson, Q. Zhang, W. Bennett, J. Briggs, S. M. Carroll, D. K. Duncan, D. Figueroa, H. H. Lanning, T. Misch, J. Mueller, R. W. Noyes, D. Poppe, A. C. Porter, C. R. Robinson, J. Russell, J. C. Shelton, T. Soyumer, A. H. Vaughan, and J. H. Whitney. Chromospheric variations in main-sequence stars. *ApJ*, 438:269–287, January 1995. doi: 10.1086/175072.

S. L. Baliunas, G. W. Henry, R. A. Donahue, F. C. Fekel, and W. H. Soon. Properties of Sun-like Stars with Planets: rho 1 Cancris, tau Bootis, and upsilon Andromedae. *ApJ*, 474:L119+, January 1997. doi: 10.1086/310442.

S. L. Baliunas, R. A. Donahue, W. Soon, and G. W. Henry. Activity Cycles in Lower Main Sequence and POST Main Sequence Stars: The HK Project. In R. A. Donahue and J. A. Bookbinder, editors, *Cool Stars, Stellar Systems, and the Sun*, volume 154 of *Astronomical Society of the Pacific Conference Series*, pages 153–+, 1998.

J. M. Beckers, C. A. Bridges, and L. B. Gilliam. *A high resolution spectral atlas of the solar irradiance from 380 to 700 nanometers. Volume 2: Graphical form.* June 1976.

F. C. Bertiau. The Orbits of the Spectroscopic Binaries Rho Orionis, Eta Bootis, and 32 Virginis. *ApJ*, 125:696–+, May 1957. doi: 10.1086/146343.

I. N. Bronstein, K. A. Semendjajew, G. Musiol, and H. Mühlig. *Taschenbuch der Mathematik.* 2001.

R. P. Butler, G. W. Marcy, E. Williams, H. Hauser, and P. Shirts. Three New "51 Pegasi–Type" Planets. *ApJ*, 474:L115+, January 1997. doi: 10.1086/310444.

G. Cayrel de Strobel. Stars resembling the Sun. *A&A Rev.*, 7:243–288, 1996. doi: 10.1007/s001590050006.

A. N. Cox. *Allen's astrophysical quantities.* 2000.

H. Dekker, S. D'Odorico, A. Kaufer, B. Delabre, and H. Kotzlowski. Design, construction, and performance of UVES, the echelle spectrograph for the UT2 Kueyen Telescope at the ESO Paranal Observatory. In M. Iye and A. F. Moorwood, editors, *Society of Photo-Optical Instrumentation Engineers (SPIE) Conference Series*, volume 4008 of *Society of Photo-Optical Instrumentation Engineers (SPIE) Conference Series*, pages 534–545, August 2000.

A. K. Dobson. Short Time-Scale Variations in CA II H+K Observations. In M. S. Giampapa & J. A. Bookbinder, editor, *Cool Stars, Stellar Systems, and the Sun*, volume 26 of *Astronomical Society of the Pacific Conference Series*, pages 297–+, 1992.

R. A. Donahue. *Surface differential rotation in a sample of cool dwarf stars.* PhD thesis, AA(New Mexico State Univ., University Park.), 1993.

D. K. Duncan, A. H. Vaughan, O. C. Wilson, G. W. Preston, J. Frazer, H. Lanning, A. Misch, J. Mueller, D. Soyumer, L. Woodard, S. L. Baliunas, R. W. Noyes, L. W. Hartmann, A. Porter, C. Zwaan, F. Middelkoop, R. G. M. Rutten, and D. Mihalas. CA II H and K measurements made at Mount Wilson Observatory, 1966-1983. *ApJS*, 76: 383–430, May 1991. doi: 10.1086/191572.

J. A. Eddy. The Maunder Minimum. *Science*, 192:1189–1202, June 1976.

H-J. Eichler, M. Freyberger, H. Fuchs, F. Haug, H. Kaase, J. Kross, H. Lang, H. Lichte, H. Niedrig, T. Pfau, H. Rauch, W. P. Schleich, G. Schmahl, E. Sedlmayr, F. Serick, K. Vogel, H. Weber, and K. Weber. *Bergmann Schaefer Lehrbuch der Experimentalphysik Band 3 Optik.* 2004.

P. V. Foukal. *Solar Astrophysics, 2nd, Revised Edition.* April 2004.

R. Glebocki and A. Stawikowski. Catalog of Projected Rotational Velocities. *Acta Astronomica*, 50:509–515, December 2000.

J. N. González-Pérez, A. Hempelmann, M. Mittag, and H.-J. Hagen. Controlling the Hamburg Robotic Telescope: a description of the software. In *Society of Photo-Optical Instrumentation Engineers (SPIE) Conference Series*, volume 7019 of *Society of*

Photo-Optical Instrumentation Engineers (SPIE) Conference Series, August 2008. doi: 10.1117/12.796646.

D. F. Gray. *The Observation and Analysis of Stellar Photospheres.* September 2005.

R. O. Gray, C. J. Corbally, R. F. Garrison, M. T. McFadden, and P. E. Robinson. Contributions to the Nearby Stars (NStars) Project: Spectroscopy of Stars Earlier than M0 within 40 Parsecs: The Northern Sample. I. *AJ*, 126:2048–2059, October 2003. doi: 10.1086/378365.

M. Güdel and Y. Nazé. X-ray spectroscopy of stars. *A&A Rev.*, 17:309–408, September 2009. doi: 10.1007/s00159-009-0022-4.

H. Haken and H. C. Wolf. *Atom- und Quantenphysik.* 2004.

J. C. Hall. On the Determination of Empirical Stellar Flux Scales. *PASP*, 108:313–+, April 1996. doi: 10.1086/133724.

J. C. Hall and G. W. Lockwood. The solar-stellar spectrograph: Project description, data calibration, and initial results. *ApJ*, 438:404–419, January 1995. doi: 10.1086/175084.

J. C. Hall and G. W. Lockwood. The Chromospheric Activity and Variability of Cycling and Flat Activity Solar-Analog Stars. *ApJ*, 614:942–946, October 2004. doi: 10.1086/423926.

J. C. Hall, G. W. Lockwood, and B. A. Skiff. The Activity and Variability of the Sun and Sun-like Stars. I. Synoptic Ca II H and K Observations. *AJ*, 133:862–881, March 2007. doi: 10.1086/510356.

J. C. Hall, G. W. Henry, G. W. Lockwood, B. A. Skiff, and S. H. Saar. The Activity and Variability of the Sun and Sun-Like Stars. II. Contemporaneous Photometry and Spectroscopy of Bright Solar Analogs. *AJ*, 138:312–322, July 2009. doi: 10.1088/0004-6256/138/1/312.

L. Hartmann, D. R. Soderblom, R. W. Noyes, N. Burnham, and A. H. Vaughan. An analysis of the Vaughan-Preston survey of chromospheric emission. *ApJ*, 276:254–265, January 1984. doi: 10.1086/161609.

P. H. Hauschildt and E. Baron. Numerical solution of the expanding stellar atmosphere problem. *Journal of Computational and Applied Mathematics*, 109:41–63, September 1999.

P. H. Hauschildt, F. Allard, E. Baron, J. Aufdenberg, and A. Schweitzer. Stellar atmospheres and synthetic spectra for GAIA. In U. Munari, editor, *GAIA Spectroscopy: Science and Technology*, volume 298 of *Astronomical Society of the Pacific Conference Series*, pages 179–+, 2003a.

P. H. Hauschildt, T. S. Barman, E. Baron, and F. Allard. Temperature Correction Methods. In I. Hubeny, D. Mihalas, & K. Werner, editor, *Stellar Atmosphere Modeling*, volume 288 of *Astronomical Society of the Pacific Conference Series*, pages 227–+, January 2003b.

A. Hempelmann. Wavelet analysis of stellar differential rotation. II. The Sun in ultraviolet. *A&A*, 388:540–545, June 2002. doi: 10.1051/0004-6361:20020572.

A. Hempelmann. Wavelet analysis of stellar differential rotation. III. The Sun in white light. *A&A*, 399:717–721, February 2003. doi: 10.1051/0004-6361:20021758.

A. Hempelmann and R. A. Donahue. Wavelet analysis of stellar differential rotation. I. The Sun. *A&A*, 322:835–840, June 1997.

A. Hempelmann, J. H. M. M. Schmitt, and K. Stępień. Coronal X-ray emission of cool stars in relation to chromospheric activity and magnetic cycles. *A&A*, 305:284–+, January 1996.

G. W. Henry, S. L. Baliunas, R. A. Donahue, F. C. Fekel, and W. Soon. Photometric and Ca II H and K Spectroscopic Variations in Nearby Sun-like Stars with Planets. III. *ApJ*, 531:415–437, March 2000. doi: 10.1086/308466.

T. J. Henry, D. R. Soderblom, R. A. Donahue, and S. L. Baliunas. A Survey of Ca II H and K Chromospheric Emission in Southern Solar-Type Stars. *AJ*, 111:439–+, January 1996. doi: 10.1086/117796.

J. Holmberg, B. Nordström, and J. Andersen. The Geneva-Copenhagen survey of the solar neighbourhood. III. Improved distances, ages, and kinematics. *A&A*, 501:941–947, July 2009. doi: 10.1051/0004-6361/200811191.

J. H. Horne and S. L. Baliunas. A prescription for period analysis of unevenly sampled time series. *ApJ*, 302:757–763, March 1986. doi: 10.1086/164037.

K. Horne. An optimal extraction algorithm for CCD spectroscopy. *PASP*, 98:609–617, June 1986. doi: 10.1086/131801.

K. R. Lang. *The Sun from Space*. 2008.

J. L. Linsky. Formation of the Calcium H, K, and Subordinate Lines in the Solar Chromosphere. *SAO Special Report*, 274, May 1968.

J. L. Linsky. Nonradiative activity across the H-R diagram - Which types of stars are solar-like? *Sol. Phys.*, 100:333–362, October 1985. doi: 10.1007/BF00158435.

J. L. Linsky, W. McClintock, R. M. Robertson, and S. P. Worden. Stellar model chromospheres. X - High-resolution, absolute flux profiles of the CA II H and K lines in stars of spectral types F0-M2. *ApJS*, 41:47–74, September 1979. doi: 10.1086/190607.

M. Mayor, F. Pepe, D. Queloz, F. Bouchy, G. Rupprecht, G. Lo Curto, G. Avila, W. Benz, J.-L. Bertaux, X. Bonfils, T. dall, H. Dekker, B. Delabre, W. Eckert, M. Fleury, A. Gilliotte, D. Gojak, J. C. Guzman, D. Kohler, J.-L. Lizon, A. Longinotti, C. Lovis, D. Megevand, L. Pasquini, J. Reyes, J.-P. Sivan, D. Sosnowska, R. Soto, S. Udry, A. van Kesteren, L. Weber, and U. Weilenmann. Setting New Standards with HARPS. *The Messenger*, 114:20–24, December 2003.

D. Meschede. *Gerthsen Physik*. 2006.

S. Messina and E. F. Guinan. Magnetic activity of six young solar analogues II. Surface Differential Rotation from long-term photometry. *A&A*, 409:1017–1030, October 2003. doi: 10.1051/0004-6361:20031161.

R. Mewe and C. Zwaan. Chromospheric and Coronal Activity in F-Type G-Type and K-Type Stars. *SAO Special Report*, 389:123–+, 1980.

R. Mewe, C. J. Schrijver, and C. Zwaan. Coronal activity in F-, G-, and K-type stars. *Space Science Reviews*, 30:191–199, March 1981. doi: 10.1007/BF01246018.

F. Middelkoop. Magnetic structure in cool stars. IV - Rotation and CA II H and K emission of main-sequence stars. *A&A*, 107:31–35, March 1982.

M. Mittag. Die technische Performance des Hamburger Robotischen Teleskops. Diploma thesis, Universität Hamburg, 2006.

D. Montes, M. J. Fernández-Figueroa, E. De Castro, M. Cornide, A. Latorre, and J. Sanz-Forcada. Multiwavelength optical observations of chromospherically active binary systems. III. High resolution echelle spectra from Ca ii H & K to Ca ii IRT. *A&AS*, 146: 103–140, October 2000. doi: 10.1051/aas:2000359.

P. Murdin. *Encyclopedia of astronomy and astrophysics.* 2001.

R. W. Noyes, L. W. Hartmann, S. L. Baliunas, D. K. Duncan, and A. H. Vaughan. Rotation, convection, and magnetic activity in lower main-sequence stars. *ApJ*, 279: 763–777, April 1984. doi: 10.1086/161945.

B. J. Oranje. The CA II K emission from the sun as a star. II - The plage emission profile. *A&A*, 124:43–49, July 1983.

E. N. Parker. Hydromagnetic Dynamo Models. *ApJ*, 122:293–+, September 1955. doi: 10.1086/146087.

E. N. Parker. The Generation of Magnetic Fields in Astrophysical Bodies. I. The Dynamo Equations. *ApJ*, 162:665–+, November 1970. doi: 10.1086/150697.

M. A. C. Perryman and ESA, editors. *The HIPPARCOS and TYCHO catalogues. Astrometric and photometric star catalogues derived from the ESA HIPPARCOS Space Astrometry Mission*, volume 1200 of *ESA Special Publication*, 1997.

N. E. Piskunov and J. A. Valenti. New algorithms for reducing cross-dispersed echelle spectra. *A&A*, 385:1095–1106, April 2002. doi: 10.1051/0004-6361:20020175.

W. H. Press, S. A. Teukolsky, W. T. Vetterling, and B. P. Flannery. *Numerical recipes in FORTRAN. The art of scientific computing.* 1992.

R. G. M. Rutten. Magnetic structure in cool stars. VII - Absolute surface flux in CA II H and K line cores. *A&A*, 130:353–360, January 1984.

R. G. M. Rutten. Magnetic structure in cool stars. XII - Chromospheric activity and rotation of giants and dwarfs. *A&A*, 177:131–142, May 1987.

R. J. Rutten. 2003, Radiative Transfer in Stellar Atmospheres, Utrecht University lecture notes, 8th edition. 2008.

J. D. Scargle. Studies in astronomical time series analysis. II - Statistical aspects of spectral analysis of unevenly spaced data. *ApJ*, 263:835–853, December 1982. doi: 10.1086/160554.

C. J. Schrijver and O. R. Pols. Rotation, magnetic braking, and dynamos in cool giants and subgiants. *A&A*, 278:51–67, October 1993.

C. J. Schrijver and C. Zwaan. *Solar and Stellar Magnetic Activity*. April 2000.

C. J. Schrijver, J. Cote, C. Zwaan, and S. H. Saar. Relations between the photospheric magnetic field and the emission from the outer atmospheres of cool stars. I - The solar CA II K line core emission. *ApJ*, 337:964–976, February 1989. doi: 10.1086/167168.

C. Schröder, A. Reiners, and J. H. M. M. Schmitt. Ca II HK emission in rapidly rotating stars. Evidence for an onset of the solar-type dynamo. *A&A*, 493:1099–1107, January 2009. doi: 10.1051/0004-6361:200810377.

R. A. Shine, R. W. Milkey, and D. Mihalas. Resonance Line Transfer with Partial Redistribution. V. The Solar CA II Lines. *ApJ*, 199:724–733, August 1975. doi: 10.1086/153744.

E. Shkolnik, G. A. H. Walker, and D. A. Bohlender. Modulation of Ca II H and K Emission by Short-Period Planets. In D. Deming and S. Seager, editors, *Scientific Frontiers in Research on Extrasolar Planets*, volume 294 of *Astronomical Society of the Pacific Conference Series*, pages 157–160, 2003.

E. Shkolnik, G. A. H. Walker, D. A. Bohlender, P.-G. Gu, and M. Kürster. Hot Jupiters and Hot Spots: The Short- and Long-Term Chromospheric Activity on Stars with Giant Planets. *ApJ*, 622:1075–1090, April 2005. doi: 10.1086/428037.

E. Shkolnik, D. A. Bohlender, G. A. H. Walker, and A. Collier Cameron. The On/Off Nature of Star-Planet Interactions. *ApJ*, 676:628–638, March 2008. doi: 10.1086/527351.

P. Skoda and M. Slechta. Reduction of spectra exposed by the fiber-fed echelle spectrograph HEROS. *Publications of the Astronomical Institute of the Czechoslovak Academy of Sciences*, 90:40–60, 2002.

K. Stepien. Excess calcium emission flux and the Rossby number. *A&A*, 210:273–278, February 1989.

K. Stepien. Applicability of the Rossby number in activity-rotation relations for dwarfs and giants. *A&A*, 292:191–207, December 1994.

R. W. Stimets and R. H. Giles. Rotational modulation of chromospheric variations of main-sequence stars. *ApJ*, 242:L37–L41, November 1980. doi: 10.1086/183397.

M. Stix. *The sun : an introduction*. 2004.

K. G. Strassmeier. *Aktive Sterne. Laboratorien der solaren Astrophysik*. 1997.

M. P. Thekaekara. Extraterrestrial solar spectrum, 3000 - 6100 Å at 1-Å intervals. *Appl. Opt.*, 13:518–522, 1974.

John. H. Thomas and Nigel. O. Weiss. *Sunspots and Starspots*. 2008.

A. H. Vaughan. Comparison of activity cycles in old and young main-sequence stars. *PASP*, 92:392–396, August 1980. doi: 10.1086/130684.

A. H. Vaughan and G. W. Preston. A survey of chromospheric CA II H and K emission in field stars of the solar neighborhood. *PASP*, 92:385–391, August 1980. doi: 10.1086/130683.

A. H. Vaughan, G. W. Preston, and O. C. Wilson. Flux measurements of CA II H and K emission. *PASP*, 90:267–274, June 1978. doi: 10.1086/130324.

A. H. Vaughan, G. W. Preston, S. L. Baliunas, L. W. Hartmann, R. W. Noyes, F. Middelkoop, and D. Mihalas. Stellar rotation in lower main-sequence stars measured from time variations in H and K emission-line fluxes. I - Initial results. *ApJ*, 250: 276–283, November 1981. doi: 10.1086/159372.

J. E. Vernazza, E. H. Avrett, and R. Loeser. Structure of the solar chromosphere. III - Models of the EUV brightness components of the quiet-sun. *ApJS*, 45:635–725, April 1981. doi: 10.1086/190731.

O. R. White and W. C. Livingston. Solar luminosity variation. III - Calcium K variation from solar minimum to maximum in cycle 21. *ApJ*, 249:798–816, October 1981. doi: 10.1086/159338.

O. C. Wilson. Chromospheric variations in main-sequence stars. *ApJ*, 226:379–396, December 1978. doi: 10.1086/156618.

O. C. Wilson and M. K. Vainu Bappu. H and K Emission in Late-Type Stars: Dependence of Line Width on Luminosity and Related Topics. *ApJ*, 125:661–+, May 1957. doi: 10.1086/146339.

U. Wolter. *Spot evolution and differential rotation of the ultrafast rotator Speedy Mic*. PhD thesis, Universität Hamburg, 2004.

J. T. Wright, G. W. Marcy, R. P. Butler, and S. S. Vogt. Chromospheric Ca II Emission in Nearby F, G, K, and M Stars. *ApJS*, 152:261–295, June 2004. doi: 10.1086/386283.

H. Zirin. *Astrophysics of the sun*. 1988.

Acknowledgements